Nanoscopía de fluorescencia por localización estocástica de moléculas individuales

Barabas, Federico M.

2017-03-27

Cita tipo APA:

Barabas, Federico M.. (2017-03-27). Nanoscopía de fluorescencia por localización estocástica de moléculas individuales. Facultad de Ciencias Exactas y Naturales. Universidad de Buenos Aires.

Cita tipo Chicago:

Barabas, Federico M.. "Nanoscopía de fluorescencia por localización estocástica de moléculas individuales". Facultad de Ciencias Exactas y Naturales. Universidad de Buenos Aires. 2017-03-27.

Universidad de Buenos Aires
Facultad de Ciencias Exactas y Naturales
Departamento de Física

Nanoscopía de fluorescencia por localización estocástica de moléculas individuales

Tesis presentada para optar por el título de
Doctor de la Universidad de Buenos Aires en el área Ciencias Físicas
por Federico M. Barabas

Director de Tesis: Dr. Fernando D. Stefani
Consejera de Estudios: Dra. Andrea Bragas
Lugar de trabajo: Centro de Investigaciones en Bionanociencias,
Consejo Nacional de Investigaciones Científicas y Técnicas

Buenos Aires, 2017

Índice general

Índice de figuras

Nanoscopía de fluorescencia por localización estocástica de moléculas individuales

Hasta hace unos 20 años se creía que la difracción de la luz imponía un límite fundamental de unos 200 nm a la resolución espacial de un microscopio óptico. Las nanoscopías de fluorescencia, también llamadas microscopías de superresolución, han quebrado esta barrera y permiten en teoría alcanzar la máxima resolución espacial con sentido físico, es decir el tamaño mismo de la fuente de luz. En la práctica, sin embargo, la resolución se ve limitada a unos 20 nm por efecto de variables experimentales como la relación señal-ruido y el fotoblanqueo de los marcadores fluorescentes. Además, las nanoscopías de fluorescencia mantienen las ventajas de la microscopía de fluorescencia tradicional, como el acceso poco invasivo y la alta sensibilidad y especificidad.

Se denomina "localización de una molécula individual" al proceso numérico por el cual se extrae la posición de un emisor único a partir de la medición de su patrón de intensidad. La nanoscopía por localización estocástica de moléculas individuales (o simplemente "nanoscopía por localización") consiste en la adquisición secuencial de imágenes en las que en cada una un subconjunto estocástico de los fluoróforos de una muestra son resueltos individualmente. Como los patrones de emisión no se superponen, la precisión de localización solo depende del número de fotones detectados de cada emisión. La imagen final se construye con las posiciones de cada fluoróforo previamente localizado. Para obtener una imagen de superresolución es necesario que los marcadores estén separados por distancias menores a su imagen limitada por difracción y que éstos emitan de manera intermitente (que se enciendan y apaguen), de manera que en algún momento puedan observarse individualmente. La nanoscopía por localización comprende a un con-

junto de técnicas diferenciadas entre sí de acuerdo al mecanismo que permite el encendido y apagado de los marcadores fluorescentes.

En la presente Tesis se estudian aspectos fundamentales e instrumentales de la nanoscopía por localización y se la aplica al estudio de preguntas biológicas. En el Capítulo 1 se desarrollan los conceptos fundamentales y limitaciones de la microscopía de fluorescencia, y se introducen las técnicas de superresolución. En el Capítulo 2 se detallan los métodos y estado del arte de la nanoscopía por localización. En el Capítulo 3 se caracteriza el nanoscopio por localización con posibilidad de obtener imágenes en 3D y a dos colores de emisión, que fuera construido como parte del trabajo de Tesis. Finalmente, en los Capítulos 4 y 5 se describen aplicaciones de dicho nanoscopio en dos proyectos de relevancia biológica: el estudio en neuronas hipocampales de la estructura periódica de espectrina y la distribución espacial de proteínas presentes en la membrana del *Trypanosoma cruzi* que median la interacción entre el parásito y el huésped.

Palabras clave: fluorescencia, microscopía, superresolución, óptica, nanoscopía

Single-molecule stochastic localization fluorescence nanoscopy

Until twenty years ago it was considered that the diffraction of light imposed a fundamental limit of around 200 nm to the resolution of an optical microscope. Fluorescence nanoscopy, also known as super-resolution fluorescence microscopy, has overcome this limit. It achieves the theoretical maximum spatial resolution, which is the size of the light source itself. In practice, however, the resolution is limited to around 20 nm by experimental factors like the signal-to-noise ratio and the photobleaching of fluorescent markers. Besides, fluorescence nanoscopy maintains the advantages of traditional fluorescence microscopy, like its low invasivity and its high sensitivity and specificity.

Single-molecule localization is the numerical process that extracts the single-molecule position from measuring its emission pattern. Sigle-molecule stochastic localization nanoscopy (or simply “localization nanoscopy”) consists of the sequential acquisition of images of well separated fluorophores from a stochastic subset of all fluorophores in the sample. As their emission patterns do not overlap, the position of each molecule can be determined with a precision only limited by the number of detected photons. A final super-resolved image is reconstructed from the localizations of all the fluorophores of the sequence of images. In order to obtain a super-resolved image, it is essential to have fluorescent markers closer to each other than the diffraction limit. Also, they must intermittently switch on and off, so that at a given point in time they can be imaged individually. Stochastic localization nanoscopy denotes a group of techniques each with a different mechanism for the on-off switching of the fluorophores.

In this thesis we study fundamental and instrumental aspects of localization

nanoscopy and we apply it to the study of biological questions. In Chapter 1 the fundamental concepts, potential and limitations of fluorescence microscopy are presented, followed by an introduction to super-resolution techniques. The fundamental principles and methods of single-molecule localization fluorescence nanoscopy are explained in detail in Chapter 2. Chapter 3 gives a complete description of the nanoscope built as part of this thesis work at the Centro de Investigaciones en Bionanociencias (CIBION), along with guidelines for its operation and an illustration of its performance. In Chapters 4 and 5 two biological applications of the nanoscope are presented, that address nanoscale organization proteins: firstly, the quantification of the periodic spectrin structure present in hippocampal neurons and secondly, the spatial distribution of proteins on the outer membrane of the *Trypanosoma cruzi* that mediate the parasite-host interaction. Finally, the conclusions of this thesis and future perspectives are unfolded in Chapter 6.

KEYWORDS: FLUORESCENCE, MICROSCOPY, SUPER-RESOLUTION, OPTICS, NANOSCOPY.

Agradecimientos

A Fernando Stefani, por la confianza y lo enseñado. Por estar siempre disponible y abierto a la discusión. Por las oportunidades de aprendizaje y desarrollo. Por exigirme siempre a mejorar.

A Andrea Bragas, por ser mi consejera de estudios y estar disponible siempre que fue necesario.

A Francisco Balzarotti y Martín Caldarola por escucharme, por enseñarme ciencia y cómo hacerla.

A Stefan Hell y Mark Bates, por hacer posible mi experiencia en Göttingen, enriquecedora en múltiples sentidos.

A los amigos del MPI-BPC, especialmente a Yvan, Fran, Bryce, Elisa, Ila, Micha, Fabian, Deb, Seb y Mark. Göttingen hubiera estado mucho más nublado sin ustedes.

A los Nanofísicos, Jesi, Iani, Cata, Chechu y Santi, con los que armamos un gran equipo y grupo de amigos. Mención especial para Lucho, mi *colaborador*/espía internacional.

A los becarios y personal del CIBION, especialmente a Alan y Antonella. Gracias a Pedro Aramendía por las discusiones enriquecedoras y por liderar un instituto donde da gusto trabajar.

Del IBioBA, gracias a Raquel, Georgina, Sebastián y Damián por enseñarme biología y por su compromiso con los proyectos juntos.

Al eterno núcleo y grupo de contención de es-importante: JJ, Mechi, NA, Sabri, PP, Marian, Ari, Freitas, Gabi y Mario. A Juli, mi último y definitivo compañero de laboratorio, crucial en tantos momentos.

A Vir, por todos estos años juntos pero, más que nada, por los que vienen.

Glosario

BFP	back focal plane 40, 42, 48
CMOS	complementary metal–oxide–semiconductor 40, 45, 49, 52, 68
CRLB	Cramér-Rao lower bound 27
EMCCD	electron-multiplying charge coupled device 22, 31, 40, 44, 51, 54, 56
FOV	field of view 51, 63, 65
FRC	Fourier ring correlation 35
FWHM	full width at half maximum 9–11, 25, 26, 34, 35, 37, 55, 56, 58, 59, 61
GFP	green fluorescent protein 7, 13
GSD	ground-state depletion 15, 20
GSDIM	ground state depletion microscopy followed by individual molecule return 17, 20, 29, 38
GUI	graphical user interface 49, 50, 52
HRR	horizontal readout rate 54
LS	least-squares 26–28, 37
MLE	maximum likelihood estimator 26–28, 37
NA	numerical aperture 8, 9, 11
PA-GFP	photoactivatable green fluorescent protein 29
PAINT	point accumulation for imaging in nanoscale topography 17, 20, 30, 31, 38, 55, 56
PALM	photoactivatable localization microscopy 17, 20, 24, 29, 38
PSF	point spread function 8–11, 15, 16, 19–26, 28, 37, 45, 54–56, 59–61

RESOLFT	reversible saturable optical linear fluorescence transitions 15, 20
sCMOS	scientific complementary metal–oxide–semiconductor 22
SIM	structured illumination microscopy 12, 13
SNR	signal-to-noise ratio 31, 54, 56
SPEM	saturated pattern excitation microscopy 15, 20
SSIM	saturated structured illumination microscopy 15, 20
STED	stimulated emision depletion 14, 15, 20
STM	scanning tunneling microscopy 2, 10
STORM	stochastic optical reconstruction microscopy 17, 20, 24, 29–31, 38, 41, 42, 53, 55–58, 60–62, 67, 68, 71–73, 75–79, 90, 92
TIRF	total internal reflection fluorescence 5, 19, 40, 42, 44, 48, 52–56, 67
UV	ultraviolet 29, 30, 38, 68
VSS	vertical shift speed 54

Chapter 1

Introduction

> *Strepsiades - Have you ever seen this stone in the chemist's shops, the beautiful and transparent one, from which they kindle fire?*
> *Socrates - Do you mean the burning-glass?*
> *Aristophanes, The Clouds, 424 BC*

Archaeology findings show that humans have used lenses for at least 2700 years. People from Assyria, The Ancient Egypt, Greece and Babylon made lenses by polishing crystal (quartz) or by filling glass spheres with water. They were probably used as magnification glasses or to ignite fires by concentrating sunlight[1]. The theory of refraction, however, was discovered around the tenth century by Islamic mathematicians of the court of Baghdad[2].

The first microscope was invented in 1590 in the Dutch Republic although until the mid-eighteenth century their lenses were made by trial and error methods, without a theoretical understanding of its working principles[3]. Around the end of the nineteenth century Ernst Abbe, Carl Zeiss and Otto Schott developed the mathematical basis of image formation theory and lens aberrations that allowed to properly design lenses for microscopes. They also established the spatial resolution limit of around half a wavelength for any optical system capable of image formation[4], given by the diffraction of light. This lower bound on the resolution attainable by light microscopes is now known as Abbe's resolution limit. Optical microscopy later achieved low invasivity imaging of biological samples through contrast mechanisms like silver chromate staining[5], dark-field microscopy[6], phase contrast imaging[7] and polarization microscopy[8]. However, it was the specificity given by the introduction of fluorescence[9] what found virtually unlimited application in biology.

The limitation in resolution found by Abbe held valid for more than a century. Although techniques like electron microscopy[10] and scanning tunneling microscopy (STM)[11] achieved sub-nanometer resolution because of the small De Broglie wavelength of the electron, they did it at the expense of major sample invasivity that made them incompatible with live-cell imaging. Near-field optics[12] and atomic force microscopes[13] reached nanometric resolutions but they can only probe the topography of the sample.

Far-field super-resolution or nanoscopy techniques were developed over the last 20 years. They fill the gap for a non-invasive purely optical method with nanometric resolution so that subcellular structures can be imaged with the specificity given by fluorescence staining. They overcome Abbe's diffraction limit by using the photophysical or photochemical properties of the fluorescent markers.

In this chapter the fundamentals of far-field optical nanoscopy are described. In Section 1.1 the principles of far-field optical microscopy are outlined. Molecular fluorescence basics are detailed in Section 1.2. Their combination, fluorescence microscopy, is described in Section 1.3. The origin of the resolution limit in conventional microscopy is explained in Section 1.4. Efforts to extend imaging resolution beyond this limit are analyzed in Section 1.5. Then, in Section 1.6, the two groups of fluorescence nanoscopy methods are described. Finally, the motivation and outline of this thesis is presented in Section 1.7.

1.1. Far-field optical microscopy

Far-field optical microscopes use propagating light and lenses to form images of objects. A diagram of a compound microscope, composed of an objective lens and a tube lens, is shown in Figure 1.1. The sample is located at the focal plane of the objective lens so that the light emitted within its angular aperture is collimated. This light is then refocused onto the detector by the tube lens. From geometrical optics one can calculate the lateral magnification M of the optical system as

$$\mathrm{M} = -\frac{\mathrm{y}'}{\mathrm{y}} = -\frac{f_{TL}}{f_O}, \tag{1.1}$$

where y and y′ are lateral distances between objects in the object and image plane, respectively. f_O and f_{TL} are the focal distances of the objective and tube

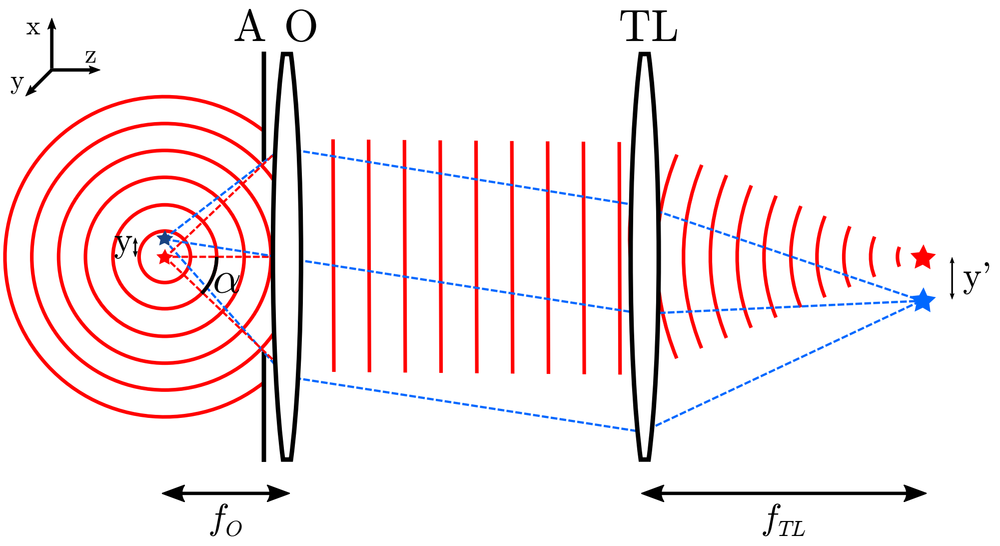

Figure 1.1: Image formation diagram for a compound microscope with an infinity-corrected objective. Two emitters are represented; the wavefront is shown for the one depicted in red and the ray tracing for the one in blue. A: objective lens aperture, O: infinity-corrected objective lens, TL: tube lens, α: angular semi-aperture of the objective lens, y and y' are the distance between emitters in the object and image plane, respectively, and f_O and f_{TL} are the focal distances of the objective and tube lenses, respectively.

lenses, respectively. The minus sign just means that the image is inverted.

An important specification of an objective lens is its numerical aperture NA:

$$\mathrm{NA} = n \, \sin\alpha, \tag{1.2}$$

where n is the immersion media refraction index and α is the angular semi-aperture of the lens. Since α is the half-angle of the maximum cone of light picked up by the lens, this parameter measures its light-gathering power. The definition of NA includes the index of refraction because Snell's law ensures that the product $n \, \sin\alpha$ remains constant across interfaces.

In this thesis compound microscopes will simply be called "microscopes" as we will not deal with single-lens microscopes.

1.2. Fluorescence

Fluorescent molecules or fluorophores are organic compounds that can emit light after absorbing light. The simplified Jablonski diagram for the energy states

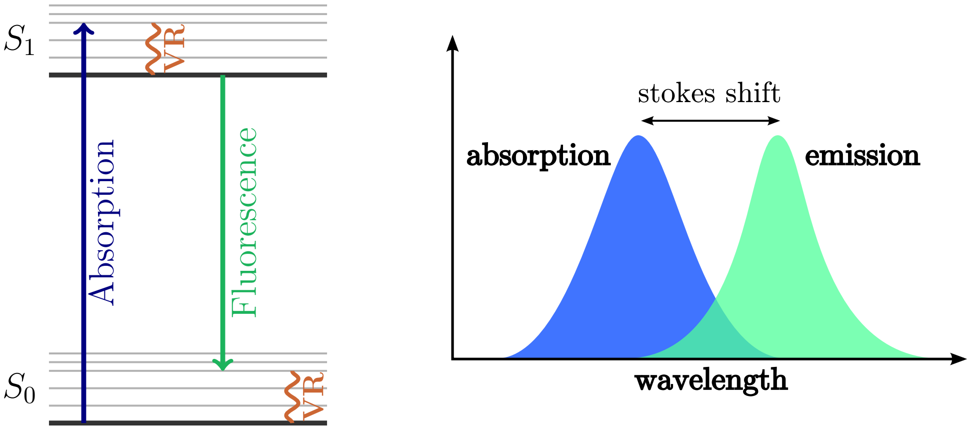

(a) Simplified Jablonski diagram of fluorescence phenomena. S_0: ground state, S_1: excited state, VR: vibrational relaxation.

(b) Absorption and emission spectra of a generic fluorescent molecule. The Stokes shift is the wavelength difference between the absorption and emission peaks.

Figure 1.2: (a) Jablonski diagram of fluorescence absorption and emission and (b) the corresponding spectra.

of a fluorescent molecule (Figure 1.2(a)) shows the ground state S_0 and the first electronic excited state S_1, each one split in vibrational states. Molecules can transition from S_0 to S_1 by absorbing a photon carrying the energy difference between the states. This energy difference ΔE is related to the photon wavelength λ through the Planck-Einstein relation:

$$\Delta E = \frac{h\,c}{\lambda}, \tag{1.3}$$

where h is the Planck's constant and c is the speed of light in the medium where the transition is taking place. The absorption process occurs in the femtosecond time scale and afterwards the molecule relaxes to the lowest energy state within S_1 in a vibrational relaxation process that spans a few ps. If we neglect the probability of intersystem crossing, at this point the molecule can only return to S_0, a transition that occurs in the nanosecond time scale.

Typical absorption and emission spectra of a fluorescent molecule are shown in Figure 1.2(b). The energy relaxation within S_1 accounts for the shift between absorption and emission spectra towards longer wavelengths, called *Stokes shift*. This spectral shift is generally of at least 20 nm and in fluorescence microscopes it allows the separation of excitation and emission light with appropriate filters.

1.3. Fluorescence microscopy

Fluorescence microscopy is the kind of optical microscopy that uses fluorescent compounds as the contrast mechanism to image samples. A typical spectral configuration is shown in Figure 1.3(a). Here, laser light (in blue) is used to excite fluorescence from a sample. A dichroic mirror reflects the laser beam towards the sample and transmits light of wavelengths around the fluorescence emission maximum, thus decoupling excitation from emission. An additional emission filter more precisely tuned to the emission peak is usually used before light reaches the detector for blocking unspecific fluorescence or autofluorescence.

Microscopes can be classified according to their excitation/detection scheme in wide-field and confocal microscopes. In the former (Figure 1.3(b)), a rather large area of the sample is illuminated and therefore the camera detects the integration of light emitted by all illuminated markers. Confocal microscopy[14] (Figure 1.3(c)) takes the opposite approach: the illumination is focused at a spot of the sample and a pinhole placed in the detection focus plane blocks out of focus emission. Background fluorescence is thus drastically reduced compared to wide-field microscopy. The trade-off to this improvement is that in order to acquire a complete image, the illumination and detection spots have to be jointly scanned through the sample so that the detector can measure the response at each position.

Total internal reflection fluorescence (TIRF) microscopy[15] is a variant of the wide-field microscopy technique that deals with the background fluorescence in a different way. If an oil immersion objective lens is used, it is possible to illuminate the sample at an angle greater than the critical angle of the glass-water (for aqueous samples) or the glass-air (for dry samples) interface. If that is the case, Snell's law ensures that there will be no transmitted beam beyond the interface. In fact, no **propagating** beam is transmitted beyond the interface but an evanescent wave still illuminates an area closer than ≈ 200 nm and therefore only fluorophores within this region are excited. This mode of illumination with evanescent waves greatly improves signal-to-noise ratio compared to straight wide-field illumination at the expense of limiting the view to a thin volume close to the interface.

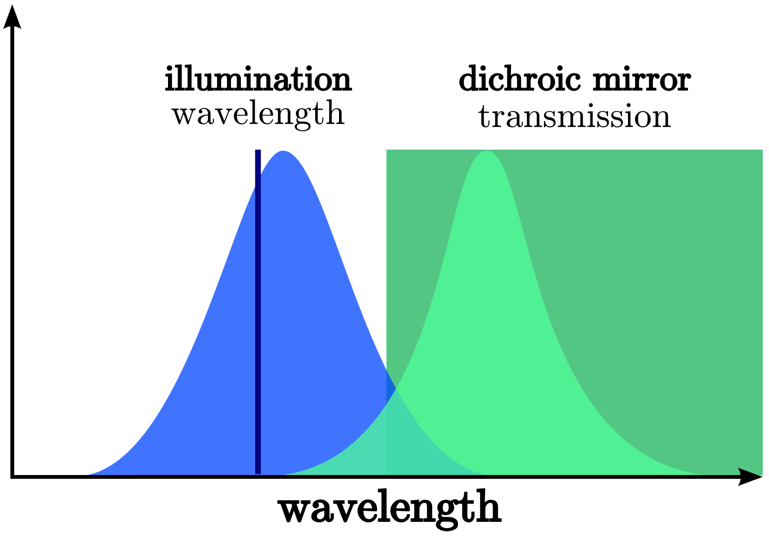

(a) Typical spectral configuration of a fluorescence microscope with laser illumination. The dichroic mirror reflects the laser light and transmits fluorescence emitted by markers in the sample.

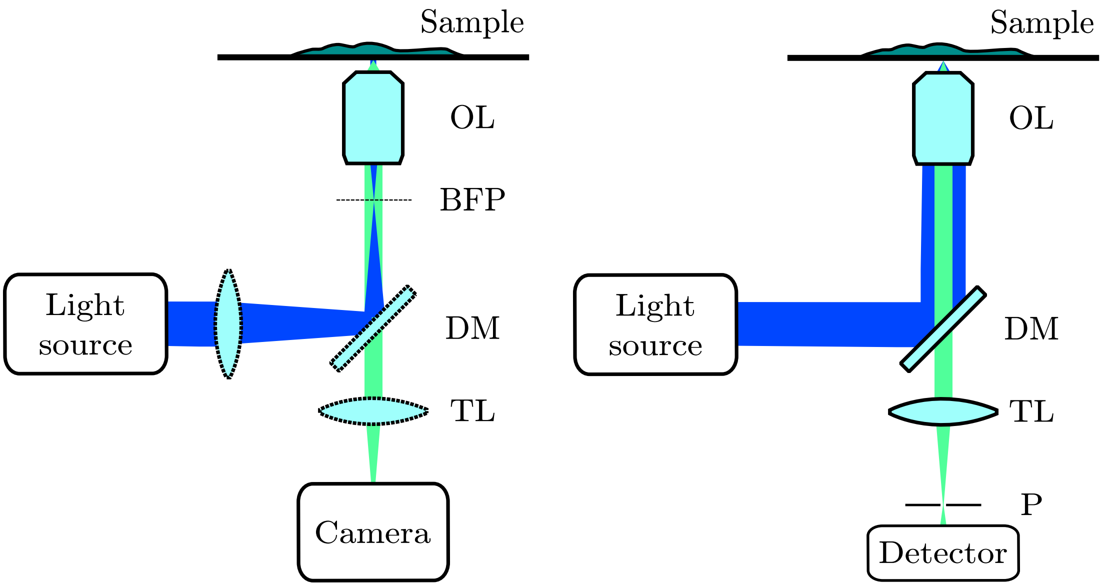

(b) A wide-field fluorescence microscope.

(c) A confocal fluorescence microscope.

Figure 1.3: Fluorescence microscopy spectral configuration and wide-field and confocal optical path diagrams. OL: objective lens, BFP: back-focal plane, DM: dichroic mirror, TL: tube lens, P: pinhole.

1.3.1. Sample staining

Since most cellular structures are optically transparent, fluorescence constitutes an effective contrast mechanism to image them. Through immunostaining, it provides highly specific labeling of subcellular structures. Fluorescence microscopy uniquely provides noninvasive imaging of the subcellular environment in three dimensions.

There are several strategies to label a sample with fluorescent markers[16]. In the case of biological samples, staining protocols need to ensure the fluorescent molecules bind to the structure of interest (proteins, lipids, nucleic acids, etc) specifically. Here we will mention intrinsic biological staining, immunostaining and fluorescent protein expression.

Some molecules intrinsically bind to a specific subcellular structure and therefore they can be used for labeling it with fluorescent markers. For instance, DAPI is a fluorescent stain that strongly binds to nucleic acid in fixed and living cells[17]. Another example is phalloidin, a toxin that binds to actin filaments[18]. It is used for staining this structure by conjugating it with a fluorescent marker[19].

Since antibodies recognize antigens very specifically, producing antibodies against the protein of interest and then staining them with a fluorophore also constitutes a very effective staining technique. This technique is known as antibody staining or immunostaining[20] and it is commonly used in cellular biology although using it in live cells remains a challenge.

In 1994 a new, revolutionary method was developed. It began with the discovery and cloning of the green fluorescent protein (GFP), expressed in the *Aequora Victoria* bioluminiscent jellyfish. It enabled the staining of virtually any protein by fusing its complementary DNA with the one of the GFP[21, 22]. After GFP, many more fluorescent proteins were developed with a wide range of spectroscopic properties and chemical sensitivity, including photoactivation[23, 24, 25, 26]. This method enables the staining of proteins in living cells, maintaining in most cases the biological function unaffected.

1.4. Resolution and the diffraction limit

1.4.1. The point spread function

Spatial resolution is a measure of the ability to distinguish two separated point-like objects from a single object[27]. The narrower these objects look as seen through the microscope, the better the resolution. In this sense the resolution of an optical system is closely related to its focusing capabilities.

According to geometrical optics, light rays originating from a point on an object can be focused to a spot by an optical system. In practice, however, the image of a point light source has a finite size. This is explained by wave optics as a consequence of the diffraction of light. The point spread function (PSF) of an optical system is the spatial intensity distribution corresponding to the image of a point light source.

We will consider an optical system along the z axis composed of an objective lens and a tube lens. A dipolar emitter with moment $\boldsymbol{\mu}$ perpendicular to the z axis and emission wavelength λ is located at the focus of the objective lens. Within the paraxial approximation (i. e. for low numerical aperture (NA) objectives), the PSF has cylindrical symmetry and takes the following form:

$$I(\rho,\theta,z=0) = I_0 \left[2\,\frac{J_1(2\pi\tilde{\rho})}{2\pi\tilde{\rho}}\right]^2, \qquad \tilde{\rho} = \frac{\mathrm{NA}\,\rho}{\mathrm{M}\lambda}, \tag{1.4}$$

where $J_1(x)$ is the Bessel function of first order and M is the magnification of the optical system. Remarkably, even for high NA objective lenses, the paraxial PSF remains a suitable approximation[27]. The function between brackets in Equation 1.4 (blue line in Figure 1.4) is called the Airy function. Its width $\Delta\rho$, defined as the radial distance for which its value becomes zero, is commonly called *Airy disk radius.* Inverting Equation 1.4, we get

$$\Delta\rho \simeq 0.61\,\frac{\mathrm{M}\,\lambda}{\mathrm{NA}}. \tag{1.5}$$

The results along z axis are similar:

$$I(\rho=0,\theta,z) = I_0 \left[\frac{\sin(\pi\tilde{z})}{\pi\tilde{z}}\right]^2, \qquad \tilde{z} = \frac{\mathrm{NA}^2 z}{2n'\mathrm{M}^2\lambda}, \tag{1.6}$$

$$\Delta z = 2\,n'\frac{\mathrm{M}^2\lambda}{\mathrm{NA}^2}. \tag{1.7}$$

1.4.2. The resolution limit

The width of the PSF in the x, y and z directions constitutes a limitation to a microscope's ability to discern two simultaneous emitting sources. If they are too close, their PSFs overlap so that they cannot be individually resolved.

In 1873 Ernst Abbe defined the minimum lateral distance between PSFs in order to be distinguishable as one Airy disk radius[4]. This means one of the PSF maximum of one of the sources coincides with the first minimum of the other. From Equation 1.5, we simply divide by M to get this distance in the object plane Δr as

$$\Delta r \backsimeq 0.61\,\frac{\lambda}{\mathrm{NA}} \tag{1.8}$$

For the axial resolution, an analogous criterion yields

$$\Delta z = 2\,\frac{n\lambda}{\mathrm{NA}^2}, \tag{1.9}$$

where n is the object plane index of refraction.

As an example, light of 670 nm imaged with an oil immersion ($n = 1.515$) objective with a NA of 1.42 has a lateral resolution limit of $\Delta r \backsimeq 287$ nm and an axial resolution limit of $\Delta z \backsimeq 1\ \mu$m.

Equation 1.8 and Equation 1.9 were traditionally considered as the optical microscopy resolution limits, also known as *Abbe's resolution limit*.

1.4.3. Gaussian approximation

The Airy disk can be well approximated by a Gaussian function, that is easier to work with. This Gaussian is often expressed as a function of its full width at half maximum (FWHM) instead of its standard deviation σ:

$$I(x) = I_0 \exp\left(-\frac{(x-x_0)^2}{2\sigma^2}\right) = I_0 \exp\left[-4\ln 2\left(\frac{x-x_0}{\mathrm{FWHM}}\right)^2\right], \tag{1.10}$$

where

$$\mathrm{FWHM} = 2\sqrt{2\ln 2}\,\sigma \tag{1.11}$$

The plot in Figure 1.4 shows an Airy disk PSF (blue line) of a molecule emitting 670 nm light. The Gaussian fit between the first minima of the Airy

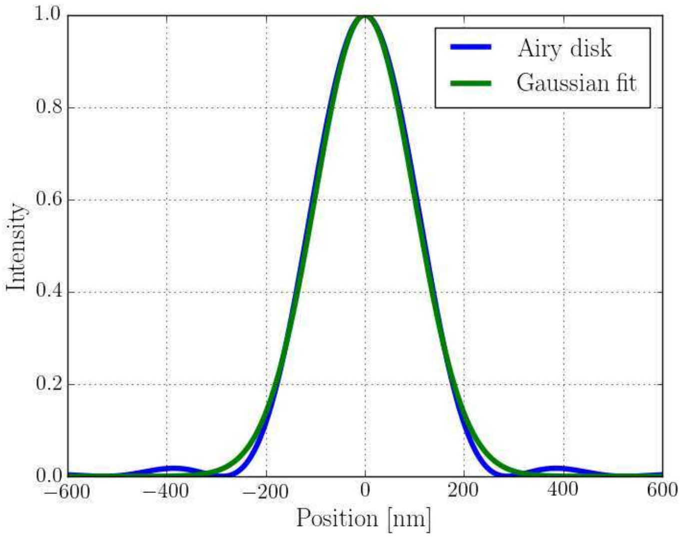

Figure 1.4: Graphical comparison of an Airy disk and a matching Gaussian function. The plotted Airy disk corresponds to the PSF along the radial coordinate ρ of a molecule emitting light of 670 nm collected by an objective lens of a NA = 1.42, as shown in Equation 1.4. The Gaussian was fitted to the Airy disk by the least squares method.

disk (within the interval $[-\Delta r, \Delta r]$ defined in Equation 1.8) is shown in red. The fit gives a FWHM of 236 nm.

1.5. Techniques to improve resolution

Both resolution limits in Equation 1.8 and Equation 1.9 have a linear dependence with the wavelength. Techniques like electron microscopy[28] and STM[29] exploit this dependence to achieve better resolutions by focusing electrons instead of visible light. Although they get the resolution down to the nanometric and subnanometric scales, they lack the advantages of optical microscopy: low invasivity, high specificity and sensitivity. The techniques presented here are still limited by diffraction but they represent the first efforts to push the resolution of optical microscopes beyond Abbe's limit.

1.5.1. Confocal microscopy

Confocal microscopy is commonly referred to as an improvement in resolution with respect to wide-field microscopy[30]. Since the total PSF can be regarded as the product of the excitation and detection PSFs,

$$I(x,y,z) = I_{ex}(x,y,z)\, I_{em}(x,y,z) \approx I_{ex}^2(x,y,z), \tag{1.12}$$

the FWHM of the resulting PSF is reduced by a $\sqrt{2}$ factor. In practice, however, $I_{ex}(x,y,z)$ and $I_{em}(x,y,z)$ are not perfectly symmetrical so the lateral resolution experiments only a slight improvement.

1.5.2. Multiphoton microscopy

Unlike confocal, two-photon scanning microscopy presents a real quadratic dependence between the total PSF and the excitation PSF[31, 32]. This technique works by exciting fluorescent molecules from their ground state to an excited one by simultaneous absorption of two (or more) photons each carrying a portion of the energy difference between the levels. In consequence, the two-photon absorption probability has a quadratic dependence with the excitation intensity. It is cubic for a three-photon process, and so on. As this process is only possible within a small volume around the focus spot, the background signal is greatly reduced (even in thick samples). Nevertheless, the quadratic dependence does not directly translate to a $\sqrt{2}$ factor reduction in the FWHM compared to wide-field microscopy. This is because the PSF widening given by the change in illumination wavelength necessary for the two-photon process overcomes the $\sqrt{2}$ factor improvement. Two-photon microscopy resolution is therefore in fact slightly worse than the resolution of confocal microscopy[33]. It is still very useful for thick samples because of the longer penetration depth of infrared wavelengths compared to visible light.

1.5.3. 4Pi microscopy

Both resolution limits in Equation 1.8 and Equation 1.9 have a decreasing dependence on the NA that can be taken advantage of to improve the resolution. A way of increasing the numerical aperture is using two objective lenses, one on each side of the sample, perfectly aligned so that they focus on the same spot of the sample. The collection angle doubles so the resulting PSF is nearly isotropic[34], improving the axial resolution to around 100 nm. The excitation can also be performed through both objectives, improving the PSF even further[35].

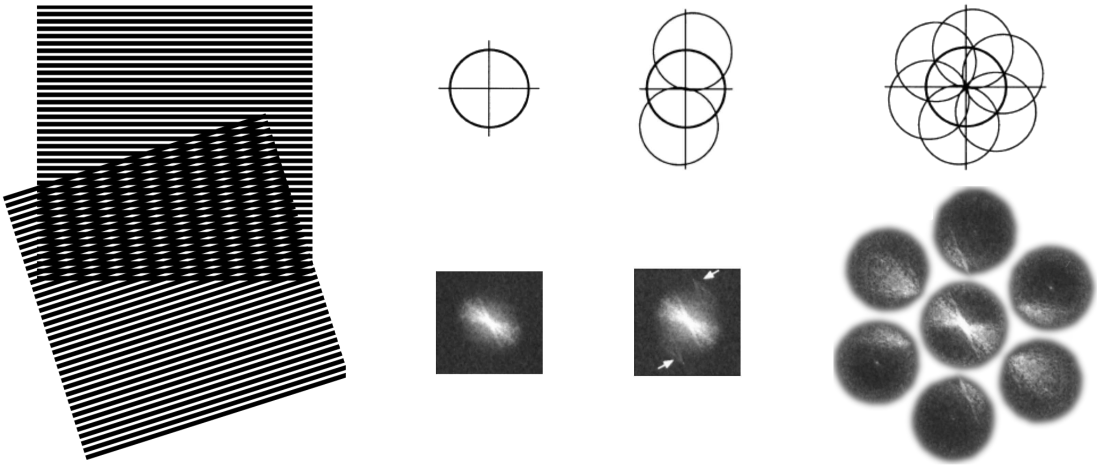

(a) (b) (c) (d)

Figure 1.5: Structured illumination microscopy concept. (a): when two fine patterns are multiplicatively superposed, the result exhibits a coarser pattern, known as moiré. (b): on top, the circle with $\frac{1}{d}$ radius (d equals to Abbe's resolution limit) in reciprocal space accessible to conventional microscopy due to diffraction; on the bottom the Fourier transform of a conventional microscopy image. (b): on top, the expanded accessible area in reciprocal space given by illuminating the sample with a sinusoidal pattern; on the bottom, the Fourier transform exhibits new components, pointed by white arrows. (c): from a sequence of images with different orientation and phase of the illumination pattern, it is possible to recover information from an area (in Fourier space) twice the size of the normally accessible region, corresponding to twice the normal resolution. Figure adapted from [37].

This technique was called “4Pi microscopy” alluding to the intention of covering the whole 4π solid angle around the emitter even though the real collected angle is smaller.

4Pi implementation in wide-field microscopy is called I^5M[36].

1.5.4. Structured illumination microscopy

The technique known as structured illumination microscopy (SIM) was fully demonstrated for the first time in 2000[37]. The concept can be understood in terms of the moiré effect. If two fine patterns are superposed multiplicatively, a beat pattern we call moiré fringes will appear in their product (Figure 1.5(a)) as a manifestation of the wave interference between patterns. In SIM, the unknown spatial distribution of fluorescent dye within the sample takes the role of one of the patterns being superposed while the other is a structured excitation light intensity. As in the example of Figure 1.5(a), the moiré fringes in the observed image show lower spatial frequencies than the original patterns. The SIM technique works because the coarser emerging pattern may then be resolvable through the microscope even if the underlying dye distribution is not. This way one can gain access to high resolution information by observing its appearance under carefully controlled illumination patterns.

A conventional microscope can only resolve structures within a circular radius of $\frac{1}{d}$ in reciprocal space, where d is Abbe's resolution limit. The same restriction applies to the illumination light pattern. Figure 1.5(b) shows the observable region on top and the Fourier transform of a conventional image on the bottom. SIM moves information from the outside into the $\frac{1}{d}$ circle, making that information observable through the coarser emerging pattern. If the illumination is structured as a sinusoidal pattern, the moiré fringes in the image contain information from an expanded area in reciprocal space (Figure 1.5(c)). In addition to the diffraction-limited circle, two new circles appear in a direction defined by the stripe direction of the pattern, and by a distance proportional to the inverse line spacing of the pattern. By recording three or more images of the sample with different illumination phases (Figure 1.5(d)), the three components can be separated through simple arithmetic, and the information restored to its proper position. By using the thinnest illumination pattern that the diffraction of light allows, enough information is transferred as to double the normal resolution. SIM can therefore reach lateral resolutions of around 100 nm.

1.6. Fluorescence nanoscopy

Until the early 1990s it was generally accepted that the only way of dramatically improving imaging resolution using light was to replace far-field optics for near-field optics, a field unlimited by the diffraction of propagating light. Efforts were made in this direction, including applications in biology[38, 39]. Even though near-field imaging is an extremely relevant technique in areas like material science, its usefulness is limited by its restriction to surfaces.

Meanwhile, important progress in the far-field fluorescence microscopy field was made thanks to developments like two-photon 3D imaging[31] and the discovery of the GFP and its variants[21, 22].

Engineering the fluorescent marker transitions was a fundamental key to un-lock unlimited resolution in far-field microscopy. The idea behind all nanoscopy or super-resolution microscopy techniques was to use molecular transitions to overcome the resolution limit. There was a radical change in conceiving fluorophores as not only reporters but also proper tools in their own right.

Several methods to overcome the diffraction limit were developed in the last few years. They all rely on switching the fluorophores between two states: the **on** and **off** states. Molecules in the on state emit detectable fluorescence while molecules in the off state are inhibited from emission or its emission cannot be detected. The nature (chemical, conformational, etc) of each state is different for each method.

Fluorescence nanoscopy methods are grouped according to their readout mode. Coordinate targeted techniques have their excitation/detection paths built in confocal configuration so that they sequentially probe every position of the sample with nanometric resolution. On the other hand, coordinate stochastic techniques are built in wide-field configuration and they simultaneously readout the sample at the single-molecule level at random positions. Here the two groups of nanoscopy techniques are described, along with some of the more relevant implementations.

1.6.1. Coordinate targeted techniques

In coordinate targeted techniques, a light pattern governing the on-off transitions precisely determines the coordinates where the sample can emit fluorescence. To that end, at least two patterns are superimposed (see Figure 1.6(a)). One of them, as in conventional confocal microscopy, transfers fluorophores within a diffraction-limited area to an excited (**on**) state, from where they can relax by emitting fluorescence. The other one, called the *depletion* pattern, transfers fluorophores to a state (**off**) from which they cannot emit detectable fluorescence. Its shape is engineered so that it presents zero intensity at the center, where the excitation pattern has its intensity maximum (see Figure 1.6(b)). In 2D, this depletion pattern takes the form a doughnut. Effectively, the region of the sample capable of emitting fluorescence photons is reduced. Scanning the excitation and depletion patterns a super-resolved image is obtained. With this method, resolutions of 20 nm have been reported in biological samples, which constitutes an order of magnitude improvement.

In 1994 Stefan Hell proposed stimulated emision depletion (STED)[41], the

(a) Excitation and depletion light patterns. Their overlap generates an effective spot reduced beyond the diffraction limit.

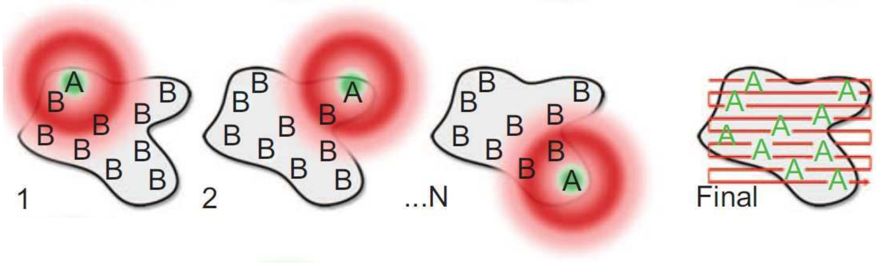

(b) Read-out procedure for coordinate targeted nanoscopy techniques. The superimposed beams are scanned through the sample. Figure adapted from [40].

Figure 1.6: Coordinate targeted fluorescence nanoscopy concept.

first viable physical concept to fundamentally overcome the diffraction limit in lens-based microscopy. STED uses stimulated emission as the mechanism to transfer fluorophores from the excited (on) state to the ground (off) state, effectively inhibiting its fluorescence emission. Stimulated emission light is filtered from the fluorescence before reaching the detector so the effective PSF of the microscope is greatly reduced, as shown in Figure 1.6(a). This concept was experimentally demonstrated for the first time in 2000[42].

A number of techniques like ground-state depletion (GSD)[43], saturated pattern excitation microscopy (SPEM) or saturated structured illumination microscopy (SSIM)[44, 45] and reversible saturable optical linear fluorescence transitions (RESOLFT)[46] were later developed following the same basic concepts for achieving super-resolution than STED but using different mechanisms for controlling the transitions between on and off states.

1.6.2. Coordinate stochastic techniques

Stochastic localization nanoscopy techniques consist of constructing a super-resolved image from the previously determined positions of each fluorophore on

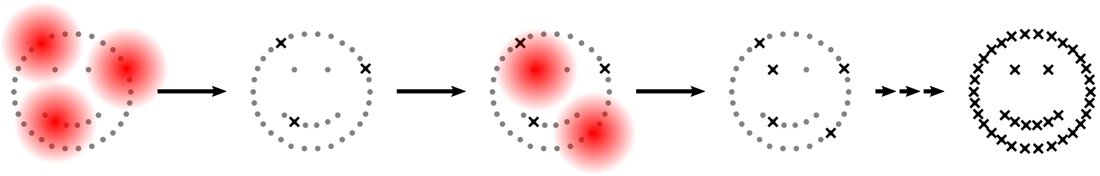

(a) Acquisition process. Single-molecule emitters are activated and localized in different frames. The final image is constructed from all the localizations.

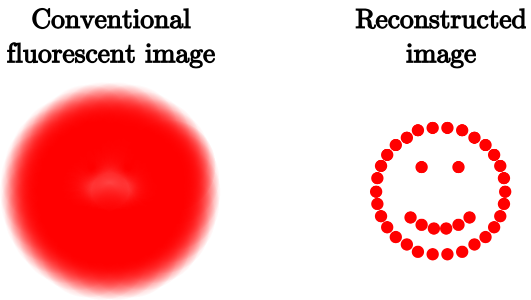

(b) Comparison between the conventional fluorescent image, in which all the fluorophores are simultaneously emitting and the super-resolved image reconstructed from localizations.

Figure 1.7: Stochastic localization fluorescence nanoscopy concept.

the sample. Although the image of a single isolated fluorophore has an intensity pattern given by the PSF of the optical system, its position can be determined (*localized*) with a precision well below the diffraction limit. This localization precision scales with the inverse squared root of the number of collected photons[47].

Conventional fluorescence microscopy images are the result of overlapping all the illuminated markers' PSFs, simultaneously emitting. Stochastic localization techniques gain resolution by separating markers along the temporal axis and for that they rely on fluorophores that can be switched between a fluorescent (**on**) emitter state and a non-fluorescent (**off** or **dark**) state. Molecules within a diffraction-limited region can be activated at different times, individually imaged and localized.

In a typical acquisition (see Figure 1.7(a)), fluorescent markers are initially in the off state and a random set are switched on in a sufficiently low concentration to make the individual imaging possible. While they are on, they emit photons that are detected with a high-sensitivity camera so that each single-molecule image can be localized with sub-diffraction precision. Then these fluorophores are switched off and the process is iterated with a new random set until a sufficiently large number of the molecules of the sample has been imaged. Finally, a super-resolved image is built from the localizations gathered from the whole acquisition. Because the localization precision is better than the diffraction limit, the reconstructed image has a better resolution than conventional fluorescence images.

The techniques within the stochastic localization group differ in the photophysical mechanism that makes the switching possible. Photoactivatable localization microscopy (PALM)[48, 49] is based on fluorescent photoactivatable proteins that can be activated with light of a certain wavelength and then excited with a different wavelength. Ground state depletion microscopy followed by individual molecule return (GSDIM)[50] works with standard fluorophores and use the triple state of the molecule as the dark state. Stochastic optical reconstruction microscopy (STORM)[51] uses synthetic fluorescent molecules that can photochemically switch to a dark reversible long-lived state. Finally, point accumulation for imaging in nanoscale topography (PAINT)[52, 53] relies on the transient binding of markers to the structure of interest.

1.7. Thesis motivation and outline

Super-resolution microscopy are recent techniques, still under constant research and development. At the same time, every new method quickly finds an application within the life sciences. Despite its enormous potential, STORM had little availability in Argentina. In this thesis the challenge of making this technology widely available to local research groups has been addressed.

The fundamental principles and methods of single-molecule localization fluorescence nanoscopy are explained in detail in Chapter 2. Chapter 3 gives a complete description of the nanoscope built as part of this thesis work at the Centro de Investigaciones en Bionanociencias (CIBION), along with guidelines for its operation and an illustration of its performance. In Chapters 4 and 5 two biological applications of the nanoscope are presented, that address nanoscale organization proteins: firstly, the quantification of the periodic spectrin structure present in hippocampal neurons and secondly, the spatial distribution of proteins on the outer membrane of the *Trypanosoma cruzi* that mediate the parasite-host interaction. Finally, the conclusions of this thesis and future perspectives are unfolded in Chapter 6.

Introducción

Los microscopios ópticos de campo lejano usan luz propagante para formar imágenes de objetos. Un diagrama de un microscopio compuesto (en esta tesis se lo llamará simplemente “microscopio”) se muestra en la Figura 1.1. Se deduce la magnificación lateral en la Ec. 1.1 y la apertura numérica en la Ec. 1.2.

Las moléculas fluorescentes o fluoróforos son compuestos orgánicos que pueden emitir luz luego de absorberla. El diagrama simplificado de Jablonski de un fluoróforo se muestra en la Figura 1.2(a). La diferencia en longitud de onda entre el espectro de absorción y emisión (Figura 1.2(b)) se denomina *desplazamiento de Stokes* y permite la separación entre luz de excitación y emisión.

La microscopía de fluorescencia es un tipo de microscopía óptica que usa compuestos fluorescentes como el mecanismo de contraste para detectar objetos. Una configuración experimental típica se muestra en la Figura 1.3(a). Los microscopios se pueden clasificar de acuerdo a su esquema de excitación/detección en microscopios de campo amplio y confocales (Figura 1.3(b) y Figura 1.3(c), respectivamente). Además, la microscopía TIRF es una variante de la de campo amplio que permite iluminar únicamente la superficie de muestras minimizando el ruido de fondo.

Existen diferentes maneras de marcar una muestra con fluoróforos de manera específica[16]: la marcación biológica intrínseca[17, 18, 19], la marcación con anticuerpos (o inmunomarcación)[20] y la expresión de proteínas fluorescentes convencionales[21, 22] y también fotoactivables[23, 24, 25, 26].

La resolución espacial es una medida de la habilidad de distinguir dos objetos cercanos individualmente[27]. La función de dispersión de punto (PSF) es la distribución de intensidad espacial de la imagen de una fuente puntual dispuesto en el punto focal geométrico. El ancho de la PSF limita la resolución del microscopio. En 1873 Abbe definió la distancia lateral mínima entre PSFs para ser distinguibles como un radio del disco de Airy[4]. Esto implica que un máximo de una de las PSFs coincida con el mínimo de la otra. En el plano objeto esta distancia está dada por la Ec. 1.8 en el plano x y y por la Ec. 1.9 en el eje z. Dichas ecuaciones constituyen el llamado límite de resolución de Abbe.

Los métodos de nanoscopía de fluorescencia se clasifican de acuerdo a su modo de detección: los dirigidos son confocales, detectan cada posición de la muestra secuencialmente. Los estocásticos son de campo amplio y detectan fluoróforos de la muestra a nivel de molécula única en posiciones aleatorias simultáneamente.

En las técnicas dirigidas, un patrón de luz controla las transiciones de prendido-apagado para determinar precisamente dónde la muestra puede emitir fluorescencia. A este efecto, dos patrones se superponen (ver Figura 1.6(a)), de manera que uno excita fluoróforos dentro de un área limitada por difracción, como en microscopía convencional. El otro, llamado *haz de depleción*, transfiere fluoróforos al estado apagado. Su forma se diseña para tener intensidad nula en el centro, donde el primer haz tiene su máximo (ver Figura 1.6(b)). La primera técnica dirigida en ser formulada[41] y realizada experimentalmente fue STED en 1994 y 2000[42], respectivamente. STED usa emisión estimulada como mecanismo de transferencia de estados. Técnicas como GSD[43], SPEM o SSIM[44, 45] y RESOLFT[46] siguen los mismos conceptos con mecanismos para las transiciones de estados.

Los métodos de nanoscopía por localización estocástica consisten en construir una imagen de superresolución a partir de las posiciones de cada fluoróforo de una muestra. La posición de un fluoróforo puede determinarse (*localizarse*) con una precisión más allá del límite de difracción[47]. La nanoscopía por localización estocástica separa los fluoróforos temporalmente usando transiciones entre un estado fluorescente (encendido) y uno no fluorescente (apagado). Los fluoróforos generalmente se encuentran inicialmente apagados y un conjunto aleatorio se encienden en una concentración suficientemente baja que permita visualizarlos individualmente (ver Figura 1.7(a)). Cada posición se determina a partir de la imagen de la molécula en un cámara de alta sensibilidad. Luego estos fluoróforos se apagan y el proceso se repite con otro conjunto de moléculas hasta localizar un número que permita formar una imagen final con las posiciones determinadas. Puesto que la precisión de localización es mayor que el límite de difracción, la imagen reconstruida tiene mayor resolución que una imagen de fluorescencia convencional. Las técnicas de nanoscopía por localización estocástica (PALM[48, 49], GSDIM[50], STORM[51] y PAINT[52, 53]) difieren en el mecanismo fotofísico que hace posible las transiciones de encendido-apagado.

Chapter 2

Single-molecule stochastic localization nanoscopy

The idea of individually localizing emitters with high precision was formally addressed during the 1980s[54] and later perfected in greater detail by several studies[47, 55, 56, 57]. Before 2006, emitters were localized within single-particle fluorescent tracking experiments. A famous example is the study of the motility model of the myosin V molecular motor, where a standard deviation for the localization precision of around 1.5 nm was achieved[58].

In a remarkable period of only four months in 2006, four techniques applied single-molecule localization to fluorescence microscopy imaging[48, 49, 51, 52] to overcome diffraction in fixed samples. Employing different mechanisms, every technique temporally separated the emission of markers so that they could be imaged individually at some time of the acquisition. All four techniques reached lateral resolutions well below Abbe's limit, for the first time in the wide-field imaging configuration. They were referred to as single-molecule stochastic localization nanoscopy.

Since then, single-molecule localization nanoscopy has greatly extended its capabilities. Three-dimensional localization[59, 60] was achieved through PSF engineering. Different approaches for acquiring multicolor images were demonstrated [61, 62, 63, 64, 65, 66, 67, 68]. Custom setups with opposing objective lenses were built[69, 70, 71], allowing to improve the localization precision by doubling the amount of collected photons and simultaneously performing axial localization through interferometry. The technique was also successfully adapted to live imaging following different strategies[72, 73, 74, 75, 76]. With the aim of reaching faster image acquisitions, software analysis methods were improved to fit the emission pattern of overlapping molecules in two[77, 78, 79] and three dimensions[80, 81], and even looking for highly overlapped switching events over the whole dataset[82]. Stochastic localization nanoscopy has also been combined with single-particle tracking to interpret millisecond dynamics of organelle transport along the cytoskeleton[83]. Concerning the achievable imaging frame rate of the technique, a recent breakthrough unlocked video-rate localization nanoscopy[84] by using scientific complementary metal–oxide–semiconductor (sCMOS) cameras instead of the classical electron-multiplying charge coupled devices (EMCCDs).

In this chapter the basics and state-of-the-art development of stochastic localization nanoscopy techniques are detailed. The fundamentals of single-molecule emission pattern localization are described in Section 2.1. In Section 2.2 the different stochastic localization nanoscopy methods are specified. Several ways of achieving multicolor localization nanoscopy imaging are outlined in Section 2.3. Three-dimensional sample drift correcting mechanisms during the minutes-long acquisitions are explained in Section 2.4. Finally, software alternatives for analyzing acquisition data, visualizing the final super-resolved images and assessing its resolution are discussed in Section 2.5.

2.1. Single-molecule localization

The methods for extracting the position of a molecule from its emission pattern are described in this section. The different fitting algorithms are discussed, as well as different experimental strategies aimed at extending localization to the axial direction. A complete review on lateral localization methods can be found in [85].

2.1.1. Lateral localization

As discussed in Section 1.4, the image of a point source produced by an optical system is a PSF with a finite size due to the diffraction of light. In fluorescence microscopy experiments, the emitter (either a fluorescent protein or an organic fluorophore) can be safely approximated by a point source because it is much smaller than the emission wavelength (roughly a hundred times smaller).

From the image of a single fluorophore, its position can be calculated either by centroid calculation or by fitting the intensity pattern to the theoretical function expected for the PSF. As each detected photon represents an independent measurement of the position of the emitter, the localization precision scales with the squared root of the number of collected photons, and if this number is high enough, the precision can reach the nanometric scale[55]. For fluorescence localization nanoscopy the centroid method is usually considered not precise enough. It is still useful as initial values for iterative fitting algorithms.

The PSF shape depends on the electric dipole moment direction and position of the emitter with respect to the optical axis. Depending on these variables, the image can be asymmetric so that the lateral photon distribution in the image plane appears shifted from the true molecular position in the object plane[86, 87, 88]. This effect is usually disregarded and the PSF is considered symmetric, which means that one must work under the assumption that emitters have a rotational mobility characterized by a cone half angle of $\alpha > 60^o$. This ensures a mislocalization error below 10 nm[88].

The adequate fitting function depends on the PSF model that suits each experiment. As discussed in Section 1.4, the PSF of an optical system in the image plane is mathematically described as an Airy disk. Most fitting methods first approximate the Airy function with a two-dimensional Gaussian function and add an intensity constant b to account for local background fluorescence and readout noise[89]:

$$I(x, y) = I_0 \exp\left[\frac{-4\ln 2}{\mathrm{FWHM}^2}\ \left((x-x_0)^2 + (y-y_0)^2\right)\right] + b, \tag{2.1}$$

where I_0 is the peak intensity and is proportional to the photon emission rate, and (x_0, y_0) are the coordinates of the fluorophore. Note that this expression assumes that the background noise is constant across the region of the spot being localized.

Next, this continuous bidimensional function $I(x, y)$ must be translated to a signal detected by discrete pixels $I(i, j)$. If the size of the pixel is substantially smaller than the PSF width, the signal can be approximated with the PSF value at the center of the pixel. However, if the pixel is larger, or if high precision is required, the integral of the PSF over the pixel area must be used (for example, an error function for the Gaussian PSF)[85].

2.1.2. Axial localization

Several approaches for the localization of single emitters in the z axis have been demonstrated. Some setups rely on simultaneously recording multiple images of the same emitter via different detection beam paths, other make use of engineering of the 3D shape of the PSF and a third group extracts axial information from near-field emission. Here we will review proposed methods with a special emphasis on astigmatism based axial localization.

Biplane microscopy[90, 91, 92], works by imaging two different planes of the sample simultaneously. The axial position of each single-molecule is calculated by comparing the two images. It is possible to expand the axial localization range by increasing the number of image planes at the cost of lateral localization precision.

In a similar scheme, a mirror with a 45° angle relative to the optical axis is placed inside the sample to generate a side view of the object in addition to the normal view[93, 94]. The axial position is then determined from this side view.

Standing wave microscopy[95] is a technique that achieves axial super-resolution within the conventional *lateral* fluorescence microscopy. Standing waves formed by interference in laser illumination create an excitation field with closely spaced nodes and antinodes, allowing optical sectioning of the specimen with a resolution of 50 nm.

4Pi microscopy[36] setups place an objective lens on each side of the sample and collect fluorescence light through both. It has been combined with localization nanoscopy in the techniques called iPALM and 4Pi-STORM, if they use PALM or STORM as the corresponding lateral nanoscopy concept[69, 70, 71]. Both extract axial localization information from the self-interference of light coming from single emitters. It is an experimentally challenging technique but it has the additional advantage of improved lateral localization as it doubles the amount of collected photons.

A recently demonstrated approach extracts the axial position of a single emitter from its near-field emission[96, 97]. The near-field component of fluorescence emission is strongly dependent on the distance between emitter and coverslip. Total emission is split in two channels and a circular aperture is placed in one of them, in a conjugate plane of the back focal plane of the objective. The near-field component of each emission is measured by comparing the signal between channels and the z position is identified from a previous calibration.

The most commonly used method, usually called PSF engineering, consists in

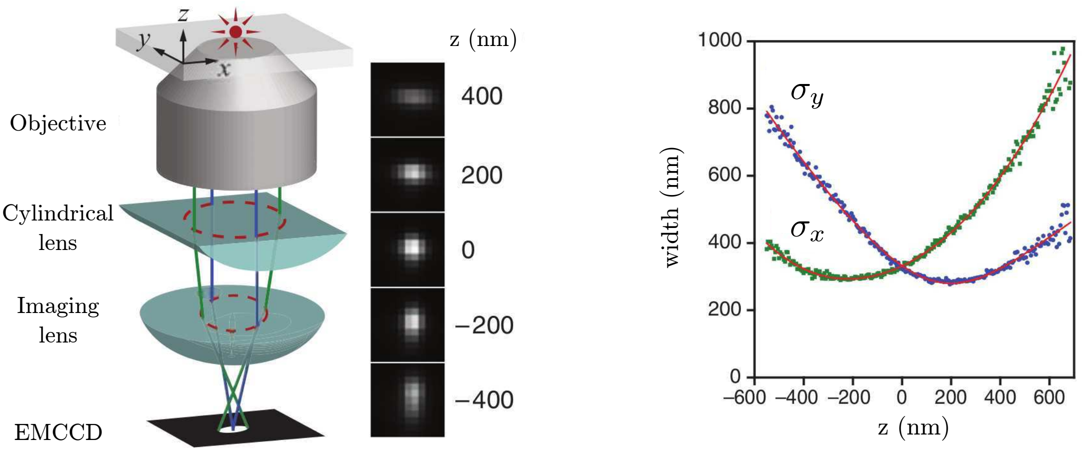

(a) Detection path diagram and effect on the PSF.

(b) σ_x and σ_y of the Gaussian PSFs vs axial position.

Figure 2.1: Axial localization concept based on generating an astigmatic PSF by inserting a cylindrical lens in the detection path. Figure adapted from [59].

shaping the PSF into a three dimensional pattern that can be used, through calibration, to identify the z position from the detected image pattern. As discussed in Section 1.4.1, the PSF naturally depends on the axial position of the emitter but this cannot be used for z localization because of its symmetry with respect to displacements from the focal plane. To solve this ambiguity, wavefront modifiers like deformable mirrors, cylindrical lenses or spatial light modulators are used to reshape the PSF.

Originally used in single-particle tracking experiments[98], cylindrical lenses[59] were the first optical element to be used for axial localization in fluorescence localization nanoscopy. A cylindrical lens focuses light into a line instead of a point, as a spherical lens would, because it affects the wavefront only in one direction (the x-axis for instance). As shown in Figure 2.1, a long focal distance ($f \simeq 1000$ mm) cylindrical lens placed in the detection path of a microscope can be used to generate a slightly astigmatic PSF, thus splitting the focal plane for the x and y axis. Before acquisition, a sample of isolated emitters is used to calibrate the σ_x and σ_y of the Gaussian PSFs as a function of axial position. This calibration is subsequently used to localize the emitter in the z axis. This method is one of the simplest approaches and allows FWHM resolutions in z of around 50 nm with a dynamic range close to 1 μm.

Alternatively, with the use of glass wedges or closely spaced nearly parallel mirrors, a PSF can be engineered so that the image of each particle is split in two lobes. The axial position is encoded in the distance and/or relative orientation of these lobes[99, 100, 101].

The use of spatial light modulators or phase plates allows for more complex PSF engineering. Single[102] and double-helix [103, 104, 105, 106, 107] PSFs encode axial information in the relative orientation of the two generated image lobes.

Finally, astigmatic PSF shaping has also been combined with multiplane imaging[108].

2.1.3. Fitting methods

Once the fitting function is chosen, one has to decide which parameters will remain fixed and which will be fitted. Typically when fitting to a function like Equation 2.1, the set of free parameters θ are the emission peak intensity I_0, the FWHM, the emitter coordinates (x_0, y_0) and the background intensity b.

There are several possible fitting algorithms. The two most common options are weighted least-squares (LS) and maximum likelihood estimator (MLE) methods. The former simply consists of finding values for the parameters θ that minimize the sum

$$S(\theta) = \sum_{ij}^{N} \left(\frac{I_{ij} - I(i,j|\theta)}{\sigma_{ij}} \right)^2 , \tag{2.2}$$

where I_{ij} is the measured intensity at the pixel (i, j), $I(i, j|\theta)$ is the expected intensity given the parameter values θ (according to a model function like Equation 2.1) and σ_{ij} is the estimate for the standard deviation of the intensity. Here the weights of the sum are $\frac{1}{\sigma_{ij}}$, which naturally means that the method will give a greater importance to data with less uncertainty. Since the intensity has a linear dependence with the number of photons and they are Poisson-distributed, one can assume $\sigma_{ij} = \sqrt{I_{ij}}$[109]. The quantity $S(\theta)$ represents the sum of relative differences between data and model, as a function of the parameters of the model. Minimizing Ec. 2.2 means in fact finding the root of equations

$$\frac{\partial S}{\partial \theta_k} = 0 \qquad k = 1, 2, \ldots, n \tag{2.3}$$

where θ_k stands for every fitting parameter of the chosen PSF function.

For the case of Equation 2.2, the solutions of Equation 2.3 do not have a closed mathematical form (it is the non-linear LS case) so numerical algorithms are used instead. Starting from a set of provided initial values, these algorithms approach the solutions iteratively. The iteration process' success critically depends on the chosen initial values.

The MLE method is based on maximizing the statistical likelihood quantity[109]. The number of photons (k) detected on each pixel ij is modeled as a Poisson process with λ_{ij} mean:

$$P_{ij}(k, \lambda_{ij}) = \frac{e^{-\lambda_{ij}}\ \lambda_{ij}^{k}}{k!}. \tag{2.4}$$

The model for the expected intensity over each pixel (Equation 2.1) depends on the parameters θ and it is used as the mean number of photons on pixel ij, $\lambda_{ij}(\theta)$. The joint probability describing the spatial distribution of the light intensity can be expressed by the likelihood L:

$$L(\theta) = \prod_{ij}^{N} P_{ij}(k, \lambda_{ij}(\theta)) \tag{2.5}$$

The parameters that maximize the likelihood of the data will be the fitting estimates $\hat{\theta}$. Taking advantage of the monotonous relation between the linear and logarithmic functions, usually the maximized quantity is the so-called log-likelihood because it is easier to work with.

$$\ln L(\theta) = \ln\left(\prod_{ij} \frac{e^{-\lambda_{ij}(\theta)}\ \lambda_{ij}^{k}(\theta)}{k!}\right) = \sum_{ij} -\lambda_{ij}(\theta) + k \ln \lambda_{ij}(\theta) - \ln k! \tag{2.6}$$

In order to maximize the log-likelihood with respect to the parameters, the last term in Equation 2.6 can be ruled out because it does not depend on them.

Besides estimating the position with the highest possible precision, a key advantage of MLE is that the precision is known. One can calculate the inverse of the Fisher information[55, 110] and average it over all localizations for calculating a variance of the estimates representative of the whole acquisition. This expected variance is called the Cramér-Rao lower bound (CRLB) and when it is possible to estimate a parameter with such precision, the estimator that achieves it is the one given by MLE. The advantages of LS are that it requires less detailed

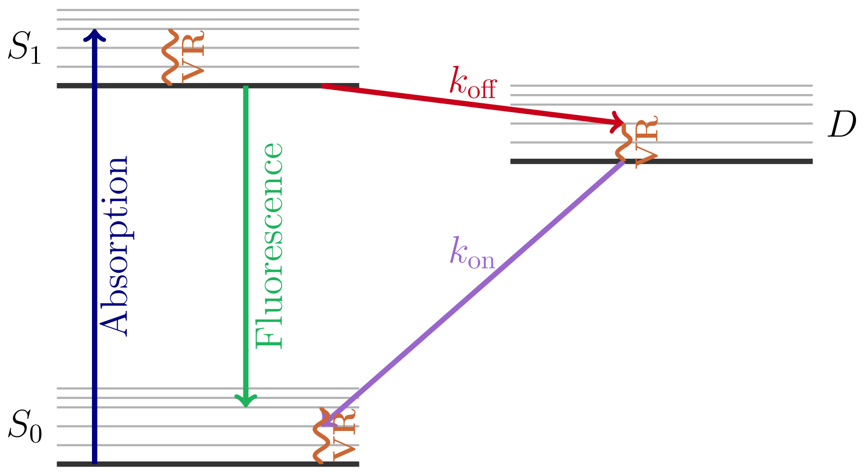

Figure 2.2: Generalized Jablonski diagram for the stochastic localization nanoscopy techniques. S_0: ground state, S_1: excited state, VR: vibrational relaxation, D: dark (non-fluorescent) state. k_{off} and k_{on} are the transition rates to and from the dark state.

information of the camera noise statistics and that it usually converges faster. On the downside, LS precision is typically 25% worse than MLE at low photon counts[111]. For any fitting method, a careful estimation of the local intensity background is critical[112]. For a more comprehensive comparison between LS and MLE, see [85, 113].

Studies recommend a detection pixel size roughly equal to the σ of the PSF[47, 55]. Most commonly used fluorophores emit in the 450-700 nm range, so following the procedure described in Section 1.4.3, a range of 95-148 nm is found for the σ of the PSF of emitters imaged with an objective of NA = 1.42. Therefore, a camera pixel size in that range is considered optimum in terms of localization accuracy.

2.2. Localization based nanoscopy techniques

All stochastic localization nanoscopy methods rely on the single-molecule imaging of fluorescent molecules. Methods in the literature differ in the mechanism they use to drive a large number of markers in the sample to a dark, non-fluorescent state, so that the remaining ones appear as single, non-overlapping molecules. A generalized Jablonski diagram is shown in Figure 2.2. Here we review the basics of some of these mechanisms.

PALM is based on using photoactivatable fluorescent proteins[48, 49] like photoactivatable green fluorescent protein (PA-GFP), EosFP, Dronpa, among others. These proteins are initially in a non-fluorescent state (D state in Figure 2.2), until they are activated usually with ultraviolet (UV) light. The transition rate k_{on} to the ground state S_0 is controlled with the activation light intensity. After activation, the fluorophores are excited with light of a different wavelength until they are photobleached. The process is repeated with a new pulse of UV light in order to activate a new set of non-overlapping proteins. The acquisition finishes when a sufficiently detailed image is reconstructed or when all proteins in the sample are bleached. Fluorescent proteins are usually dimmer and easier to bleach than synthetic fluorophores. However, this method has the advantage of being easily applicable to live cells through transfection of cells with DNA encoding a photoactivatable protein.

GSDIM works with standard fluorophores like rhodamines[50], that are usually considered not switchable. In this case the dark state is an electronic triplet state of the molecule. A molecule under strong excitation experiences a large number of transitions between S_0 and S_1, emitting fluorescent photons in the process. In every transition the chance that it gets caught in the dark triplet state is small but since the number of transitions is so large, after a few seconds of continuous excitation, most molecules end up in the triplet state. The transition back to the singlet state is as forbidden as the one forward, thus the triplet state has a long lifetime (milliseconds to seconds). Whenever a molecule spontaneously undergoes the transition back to the singlet subspace, it emits fluorescence photons and can be localized.

STORM was first demonstrated with fluorescent cyanine dyes like Cy5 in an aqueous solution containing a primary thiol[114]. Red light illumination produces fluorescent emission from Cy5 and also switches the dye to a stable dark state formed by thiol attachment to the excited cyanine dye. Its absorption spectrum suffers a substantial reduction in the original absorption peak and exhibits a new peak in the UV region[115]. The cyanine-thiol bond is broken with UV light thus bringing the molecule back to the fluorescent state. This process is referred to as *reactivation*. Initially, samples were stained with dye pairs like Cy3-Cy5 because the reactivation of Cy5 was shown to be facilitated a nearby secondary chromophore that could efficiently absorb the activation light[114]. In subsequent studies the use of facilitating chromophores like Cy3 was discontinued because Cy5 alone exhibited the same efficient reactivation upon UV light absorption. This simpler approach was later extended to a large number of fluorophores[116, 117, 118] by tailoring the buffer composition and imaging conditions to each one. Alexa Fluor 647, for instance, is a dye similar to Cy5 with respect to absorption and emission maxima, Stokes shift, extinction coefficient, photoswitching performance and reactivation under UV light. However, since Alexa Fluor 647 has a greater resistance to photobleaching[119] than Cy5, it has become the dye of choice for STORM[117].

The aqueous imaging buffer used as mounting media has two main components: the thiol that enables photoswitching and an oxygen scavenging system to reduce photobleaching. Popular choices for the thiol are beta-mercaptoethanol and mercaptoethilamine. The oxygen scavenging is usually composed of enzymes like glucose oxidase and catalase[114, 117]. Research on perfecting the buffer composition to improve photoswitching and reduce bleaching is still ongoing[120, 121, 122, 123, 124, 125].

PAINT follows a very different approach than previously described techniques. Here the object to be imaged is continuously targeted by fluorescent probes present in solution[52]. A fluorescent signal appears as a diffraction-limited spot on the object when a fluorophore transiently binds to it and disappears when that marker dissociates from the object or is photobleached. The effective on-off switching depends on the affinity between the label and the object, the diffusion coefficient and the concentration gradient of the probes. The first demonstration of the concept did not control the nature of the binding affinity between the sample and the dye in solution[52]. Since, the DNA-PAINT technique introduced the idea of using short DNA sequences to label subcellular structures and also for dye molecules to bind to[53]. The expansion of the concept of PAINT through DNA-PAINT led to highly specific staining and the possibility of controlling the binding affinity (and therefore the binding time) with the sequence length.

2.3. Multicolor imaging

Many biological questions require the simultaneous visualization of more than a single subcellular structure. Immunolabeling techniques are able to attach different fluorescent markers to distinct components of the cell so that they can be routinely imaged in conventional fluorescence microscopes to assemble multicolor images. Within the fluorescence localization nanoscopy field, new challenges emerge that require specific solutions. The use of (single-color) EMCCD cameras in single-molecule imaging for their superior signal-to-noise ratio (SNR) generate the need of a mechanism to tell the different markers apart.

Several sequential and simultaneous approaches for multicolor imaging have been proposed and experimentally demonstrated. In the sequential approaches, the fluorescent species are temporally separated so that a single-color acquisition is performed for each one. After all the acquisitions have taken place, a careful overlapping is needed for assembling the multicolor final image. For instance, the technique described in [66] works by labeling a subcellular structure, imaging it through fluorescence localization nanoscopy, then quenching the remaining unbleached fluorophores and repeating the process for the following structure. [65] describes a similar technique, within the PAINT concept. These methods have the advantage of dealing with single excitation and emission wavelengths but stitching the final images into the final color composition can be challenging.

Simultaneous multicolor approaches image two or more fluorescent species at the same time. Some methods discriminate them according to the fluorescence activation wavelength and others to the emission wavelength. In the activation scheme, every subcellular structure to be imaged is labelled with a dye pair (as in the first STORM implementation[114]) composed of a distinct activator[61]. As all pairs have the same reporter, they are excited with the same laser and imaged through a single emission channel. Each pair is preferentially activated with the laser tuned to the absorption peak of the activator. During acquisition, the activation lasers are temporally structured in pulses of alternating wavelengths as depicted in Figure 2.3(a), so that every single-molecule emission can be identified through the temporal sequence of activation. This approach has the advantage of using a single emission channel and therefore there is no chromatic aberration between channels.

The inverse method, known as “spectral demixing”, works by exciting different fluorescent markers with a single wavelength[62, 64]. This is only possible if they have similar or slightly overlapping absorption spectra, as in the case of Alexa Fluor 647 and Alexa Fluor 700. The emission path of the microscope is split in two spectral channels, each one roughly centered in the emission peak of each species and focused on different parts of the camera. Each fluorescence emission spectrum typically spans over both channels so that the intensity ra-

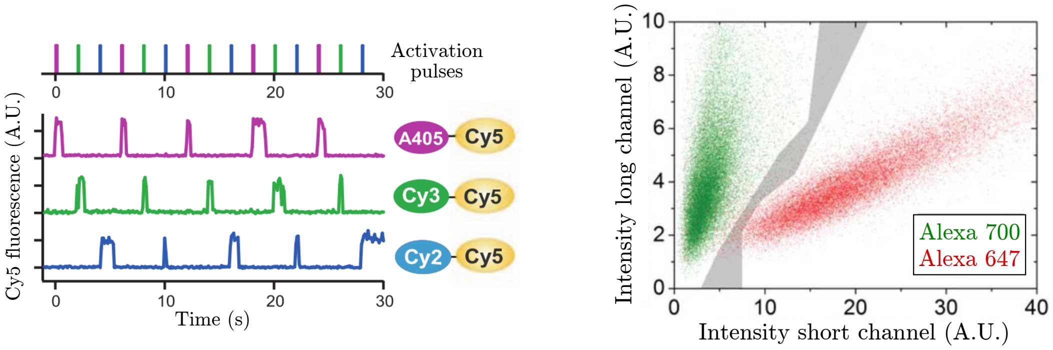

(a) Illumination pulses cycle for sequentially activating the different activator-reporter dye pairs. Figure adapted from [61].

(b) Intensity on the long wavelength channel vs on the short wavelength one for a large number of single-molecule emissions. Figure adapted from [64].

Figure 2.3: Two different concepts that achieve multicolor localization nanoscopy. The method described in (a) discerns different fluorescent dye pairs by sequentially activating each dye pair. The method in (b) excites all dyes with light of the same wavelength and identifies different species with the intensity ratio between channels.

tio between them is specific of each species. Before multicolor acquisition, the distinct ratios are measured by imaging samples stained with each dye. These measurements produce a plot like the one shown in Figure 2.3(b), where the two species are clearly separated in clusters. During the dual-color acquisition, each single-molecule emission is identified through its distinct intensity ratio between channels.

Also, both multicolor methods can be combined to discriminate a greater number of channels[63].

Single-molecule localization has also been combined with spectroscopy by adding a diffraction grating at the detection path[67, 68] and also through rotational mobility measurements[126].

2.4. Drift compensation

Due to sequential readout of markers inside a diffraction limited volume, localization nanoscopy measurements suffer from longer acquisition times than conventional microscopy, as typical times range from 1 min to 1 h[48, 127, 128]. The higher spatial resolution provided by fluorescence nanoscopy imposes stricter requirements on the mechanical stability of the imaging setups than for conventional microscopy. The displacement of the sample within the field of view due to vibration and deformation of the setup is commonly called drift. Any effective method for compensating the effect needs to ensure that during the acquisition time the displacement should be smaller than the resolution. For localization based nanoscopy this means the residual, after compensation drift, must be kept at least below 20 nm in the lateral direction and 50 nm in the axial.

The issue of lateral drift has been approached in several ways. Fiducial markers can be incorporated to the sample and used for compensating lateral displacements during acquisition[129] or for post-processing correction[48, 114]. This method provides the necessary nanometric lateral stabilization but it entails additional experimental requirements, mainly the need of having at least one fiducial marker in the field of view, perfectly bound to the sample.

Another way of compensating lateral drift is through cross-correlation analysis [130]. Basically, before reconstructing a super-resolved image from the whole set of localizations, these are divided in groups and an image is built from each one. Then, every image is cross-correlated with the first one. The result of each cross-correlation has its maxima located at the lateral displacement value between the images. Finally, the displacement that corresponds to each camera frame is calculated through interpolation of the displacements of the images. This method is as effective as the one employing fiducial markers and does not add any additional experimental complexity.

The same instabilities that drive lateral drift can also move the sample out of focus during acquisition. Contrary to the lateral case, axial drift must be actively corrected in order to have a reliable measurement. The axial position of the sample can be stabilized with a piezoelectrically driven stage or by moving the focus knob of the microscope with a motor.

A proposed way of stabilizing axial drift is based on extending the cross-correlation lateral drift method[131]. They cross-correlate each acquired image with an image taken above the focal plane and another image taken below the focal plane. They extract the defocusing distance from changes in the peak height of the correlation result.

Another way of actively correcting axial drift is described in [132]. It relies on the reflection upon the interface between coverglass and mounting medium of an IR laser in objective-based total internal reflection configuration. The position of the reflected beam is measured with a quadrant photo-diode or a camera as it depends on the objective-sample distance. Stabilizing the position of the reflected beam effectively stabilizes the axial position of the sample with nanometer accuracy but it critically relies on having a mounting media with different refraction index than that of the glass. Also, it cannot account for other defocusing factors other than a change in the distance between objective and sample.

2.5. Analysis and visualization

The automated analysis that extracts the particles coordinates of a localization nanoscopy acquisition is an intensive task. Typically, a few hundred thousand single-molecule emission patterns have to be individually discriminated from the background, fitted to a bidimensional function of no less than three parameters, their drift estimated and corrected, and finally from the results an image has to be built. Furthermore, the analysis process should be efficient enough to provide quick results.

Fortunately, several software solutions are freely available. A comprehensive benchmarking and feature comparison can be found in [113]. One notable example is ThunderSTORM[133], a software that works integrated with the widely used image analysis suite ImageJ[134]. A few of these programs are conceived to be used online to produce super-resolved images during acquisition[135].

Once single-molecule coordinates have been extracted from all the image frames, a final super-resolved image has to be built from those coordinates. An inadequate choice of the visualization method can lead to an artificial loss in the resolution of the final image[136].

The simplest method is a common scatter plot where the pixel intensity values are set to one at locations that correspond to molecular positions while all other pixel values are set to zero. This method is fast but does not reflect the density of molecules. An histogram binning the particle coordinates can also be used as the final super-resolved image. Another typical option is the Gaussian rendering with either a fixed FWHM or a FWHM equal to the fitted value of each localization. A comprehensive comparison of commonly used visualization methods and suitable new ones can be found in Refs. [136, 133].

The two parameters that most commonly limit the resolution in localization nanoscopy are localization precision and label density[137]. If a desired resolution is to be obtained, then the localization precision should be smaller and, following

Nyquist criterion, the nearest-neighbor distance between localized fluorophores should not be larger than half the desired resolution. Nevertheless, these guidelines do not account for sparsely labeled structures or for the stochastic nature of the switching dynamics needed for localization nanoscopy measurements. This means that there is a need for a way of directly measuring the resolution of an image built from localizations. This matter is still under debate and several approaches have been demonstrated. In many cases, this is done by measuring the the FWHM of the profile of thin features in the image. A more sophisticated approach uses Fourier ring correlation (FRC), a technique previously used in electron microscopy[138, 139].

Nanoscopía por localización estocástica

La posición de un fluoróforo se obtiene de su imagen ajustando el patrón de intensidad a la función esperada para su PSF[55]. Se suele aproximar la parte lateral de dicha función por una Gaussiana (Ecuación 2.1) sumada a una constante que representa el ruido de fondo[89] e integrada sobre los píxeles del detector[85].

Se han desarollado diferentes técnicas para la localización de moléculas individuales en el eje z [90, 91, 92, 93, 94, 95, 69, 70, 71, 96, 97]. El método más usado consiste en transformar la PSF en un patrón tridimensional que pueda usarse para identificar la posición axial. Por ejemplo, puede usarse una lente cilíndrica para generar una imagen ligeramente astigmática[98, 59]. Calibrando la forma de la imagen, es posible localizar las moléculas individuales en z. Este método es uno de los más simples y permite resoluciones en z de unos 50 nm con un rango dinámico de 1 μm. El uso de cuñas y espejos en la muestra[99, 100, 101] o moduladores espaciales de luz[102, 103, 104, 105, 106, 107] permiten hacer uso de otros patrones tridimensionales más complejos para la PSF.

El ajuste de curva para la posición lateral permite obtener la intensidad máxima de emisión, el ancho a mitad de altura (FWHM), las coordenadas de emisión and la intensidad del fondo de fluorescencia. Los dos algoritmos más usados para el ajuste son cuadrados mínimos (LS) y el estimador de máxima verosimilitud (MLE). LS consiste en encontrar los parámetros que minimicen la suma de la Ec. 2.2, mientras que en MLE los parámetros estimados son los que maximizan la verosimilitud[109] (Ecuación 2.5). MLE estima los parámetros con mayor precisión[55, 110] pero LS requiere menos información sobre la estadística del detector y converge más rápido. Para cualquiera de los dos métodos de ajuste es crítico contar con una precisa estimación del fondo local de fluorescencia[112].

Los métodos de nanoscopía por localización estocástica se basan en la imagen individual de fluoróforos. Difieren en el mecanismo que usan para transferir moléculas a un estado no fluorescente u *oscuro* (ver diagrama de niveles generalizado en Figura 2.2), de manera que las restantes se visualicen individualmente.

PALM usa como marcadores a proteínas fluorescentes fotoactivables[48, 49] que se encuentran inicialmente en un estado no fluorescente. Una vez que algunas se activan con luz UV, pueden ser excitadas con luz de otra longitud de onda hasta fotoblanquearlas. El proceso se repite con otros grupos de proteínas hasta formar una imagen suficientemente detallada. GSDIM usa fluoróforos convencionales como rodaminas y el estado no fluorescente es el triplete electrónico de la molécula[50]. STORM usa fluoróforos que al ser excitados pueden formar compuestos con tioles[114] presentes en el medio de montaje o *buffer*. Estos compuestos también son no-fluorescentes, tienen una larga vida media y su unión puede revertise con luz UV[115] *reactivando* el fluoróforo original. PAINT funciona gracias a la unión transitoria entre fluoróforos presentes en la solución y sitios de anclaje en el objeto[52, 53]. La señal fluorescente aparece cuando un marcador se inmobiliza en el sitio y desaparece cuando se libera.

Diversos métodos de imagen multicolor fueron desarrollados dentro del campo de la nanoscopía por localización estocástica. Algunos son secuenciales, en los que se adquiere la señal de cada especie una después de la otra[66, 65], y otros simultaneos, en los que se adquieren todas las señales al mismo tiempo. En este caso, la discriminación puede efectuarse a partir de la longitud de onda de activación de cada especie[61] o la de emisión[62, 64]. También pueden combinarse para conseguir un mayor número de canales[63].

Dado que los tiempos de adquisición propios de la nanoscopía por localización van desde los minutos a la hora[48, 127, 128] y que su resolución es superior a la convencional, el desplazamiento de la muestra debe mantenerse debajo de los 20 nm en la dirección lateral y 50 nm en la axial. El desplazamiento lateral puede corregirse mediante el seguimiento de marcadores fiduciales [48, 114, 129] o con análisis de correlación de las imágenes finales[130]. El drift axial también puede corregirse con análisis de correlación[131] o mediante el monitoreo de la posición de la reflexión de un haz IR reflejado en la muestra[132].

Se encuentran disponibles softwares especialmente diseñados para la tarea de construir una imagen final a partir de la localización de las imágenes de moléculas individuales[113, 133, 135]. La manera de medir la resolución de la imagen final está en discusión y varias soluciones han sido propuestas[137, 138, 139].

Chapter 3

Fluorescence localization nanoscope

Far-field fluorescence nanoscopy techniques are still under active development and therefore there is no standard experimental design for a nanoscope yet. On the contrary, every nanoscope is customized to suit the specific needs of each laboratory. Even though fluorescence stochastic localization techniques have an enormous application potential, at the time this thesis began there was little availability of the technology in Argentina. In consequence, the first part of the thesis consisted in the design, construction and testing of a localization nanoscope.

In this chapter the nanoscope built at Centro de Investigaciones en Bionanociencias (CIBION) is described in detail. The hardware, composed of the illumination and emission paths as well as the focus stabilization unit, is detailed in Section 3.1. The alignment procedure is explained in Section 3.2. The specially developed control software is described in Section 3.3. Finally, basic operation guidelines are provided in Section 3.4.

3.1. Experimental setup

The nanoscope is built around a commercial inverted microscope stand Olympus IX73. The layout and main components of the nanoscope are schematically shown in Figure 3.1.

All mirrors of the setup are dielectric mirrors (Thorlabs BB1) because they offer superior reflectance and durability than silver mirrors. The coating was chosen to match the specific spectrum of the light reflecting at each one. All

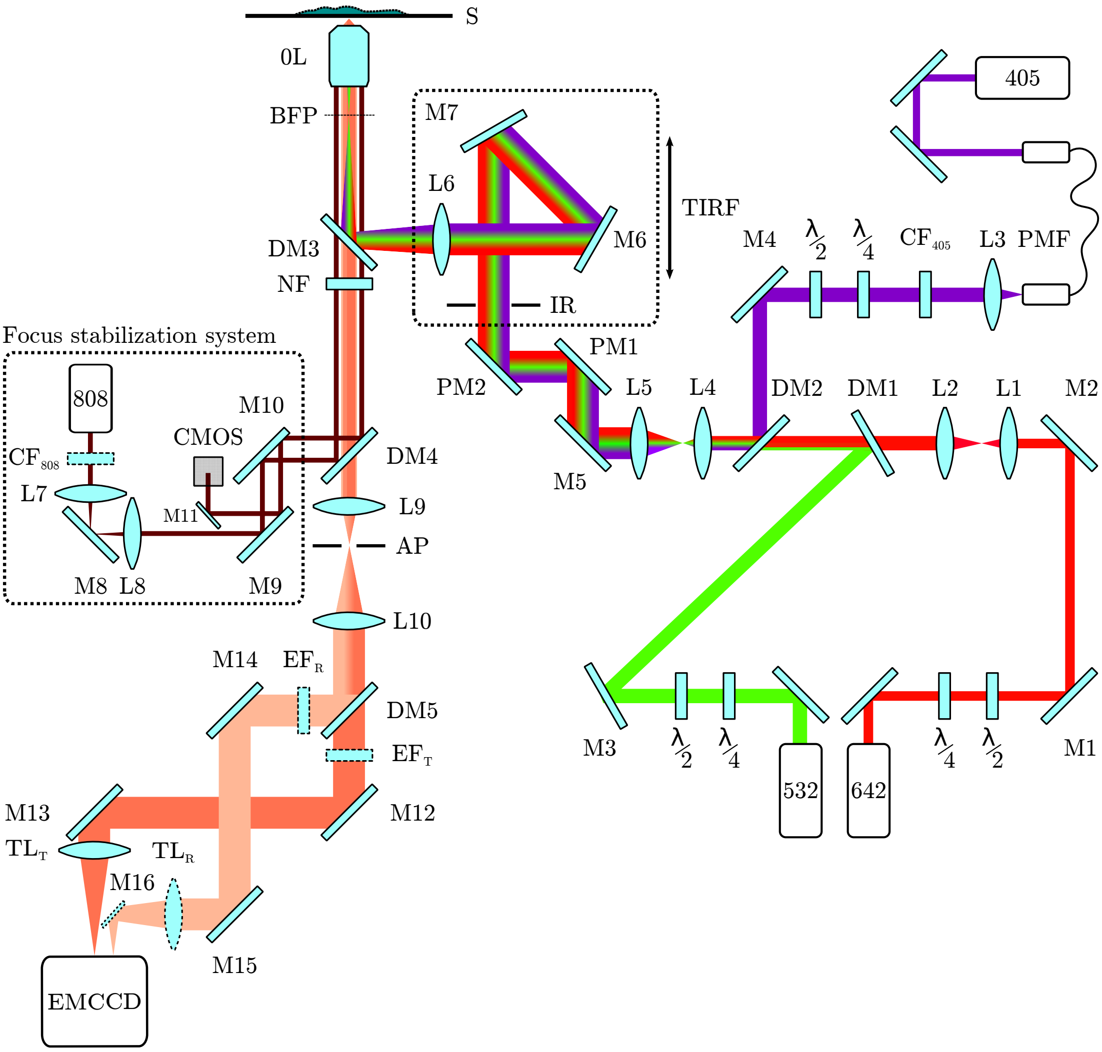

Figure 3.1: Diagram of the fluorescence localization nanoscope built at CIBION. M: mirrors, L: lenses, BS: beamsplitters, $\frac{\lambda}{2}$ half-wave plate, $\frac{\lambda}{4}$ quarter-wave plate, CF: clean-up filters, PMF: polarization-maintaining monomode optical fiber, DM: dichroic mirrors, PM: periscope mirrors, TIRF: total internal reflection fluorescence motorized linear stage, IR: iris aperture, BFP: back focal plane of the objective lens, OL: objective lens, NF: notch filter, CMOS: unexpensive camera, AP: aperture, EF: emission filters, TL: tube lenses, EMCCD: electron-multiplying charge coupled device camera.

lenses are 1” diameter achromatic doublets from Thorlabs with anti-reflection coating for visible wavelengths, unless noted otherwise.

In Sections 3.1.1 and 3.1.2 the illumination and emission parts are described, respectively.

3.1.1. Illumination path

Two continuous-wave lasers are used for fluorescence excitation, both with an output power of 1.5 W, and wavelengths of 642 nm (MPB Communications 2RU-VFL-P-1500-642) and 532 nm (Laser Quantum Ventus 532). The 642 nm laser was chosen for the excitation of Alexa Fluor 647, the most commonly used dye for the fluorescence nanoscopy technique STORM[117]. The 532 nm laser is suitable for multicolor acquisitions using for example Alexa Fluor 568 as the second label. Since the nominal beam waists are 1.5 mm for the 532 nm laser and 1 mm for the 642 nm laser, their diameters are matched by expanding the 642 nm laser with the telescope of lenses L1 and L2 (focal lengths 45 mm and 75 mm, respectively). The lowpass dichroic mirror DM1 (Semrock LM01-552-25) is used for combining the two beams.

A 405 nm 50 mW diode laser (RGB Photonics Lambda Mini) is used for reactivating cyanine fluorescent molecules by bringing them back from the long-lived dark state, as explained in Section 2.2. The laser is first coupled into a polarization-maintaining single-mode optical fiber (Thorlabs P3-405BPM-FC-2) with a fiber coupler (Schäffer+Kirchhoff 60FC-4-A7.5-02). The lens L3 ($f = 30$ mm) collimates the output of the fiber and then its spectrum is filtered with the clean-up filter CF_{405} (Semrock FF01-405/10-25). The lowpass dichroic mirror DM2 (Semrock LM01-427-25) is used for combining the 405 nm laser with the 532 nm and 642 nm lasers.

All laser beams pass through $\frac{\lambda}{2}$ and $\frac{\lambda}{4}$ multi-order phase retardant plates specific for each wavelength (Thorlabs) to tune its individual polarization state before they are combined. The beams should have circular polarization at the sample to avoid image artifacts related to the mobility of fluorophores, as explained in Section 2.1.1.

Once the three lasers are coaligned, they are expanded with the 5x telescope composed by L4 and L5 (focal lengths of 30 mm and 150 mm, respectively). The iris aperture IR permits to limit the illuminated region of the sample, typically to the area where single-molecule images are acquired for localization nanoscopy measurements. The lens L6 (f = 300 mm and 2” diameter) focuses the beams onto the back focal plane (BFP) of the objective lens OL. The TIRF platform in Figure 3.1 is mounted over a motorized linear stage (Thorlabs KMTS50E/M). By moving this stage, the focus of the lasers translates laterally within the BFP. This is useful for changing the illumination from straight wide-field to TIRF configuration, or any oblique illumination in between.

Between L5 and M5, not shown in Figure 3.1, there is a custom-made motorized filter mount with a neutral density filter with an optical density of 3. This change in illumination intensity by 1000-fold is roughly the difference needed to change from conventional fluorescence imaging to STORM imaging.

Intensity measurement

Ideally, a sample with spatially uniform fluorescence is needed to determine the intensity distribution of a laser on the sample plane. In this case, such test sample consisted of a monolayer of neutravidin protein labeled with Alexa Fluor 647 bound to the surface of a coverslip (see a protocol for preparing such a sample in Appendix A.1.2). The broad excitation spectrum of Alexa Fluor 647 makes it possible for all three lasers to excite it enough so that its intensity pattern can be measured. Still, the monolayer of Alexa Fluor 647-conjugated neutravidin is not a perfectly homogeneous sample, so a number of images from different regions were averaged to obtain the illumination field of each laser. Figure 3.2(a) shows an image of the illumination produced by the 642 nm laser, as well as two intensity profiles in orthogonal directions. In practice, the illumination field can be considered as nearly Gaussian for the three lasers used. σ is measured for each one by fitting the image with a bidimensional Gaussian function.

The illumination intensity on the sample is computed as follows[140]:

$$I_{\text{peak}} = \frac{P_{\text{BFP}} \cdot T}{2\pi\sigma^2}, \tag{3.1}$$

where P_{BFP} is the laser power at the back aperture of the objective, T is the nominal transmission of the objective at the laser wavelength and σ is the standard deviation of the Gaussian intensity pattern on the sample.

A motorized mirror placed between L5 and M5 (not shown in Figure 3.1) is used to transiently direct the laser light to a photodiode (Thorlabs DET36A) and monitor its intensity before, after or during a measurement. The photodiode volt-

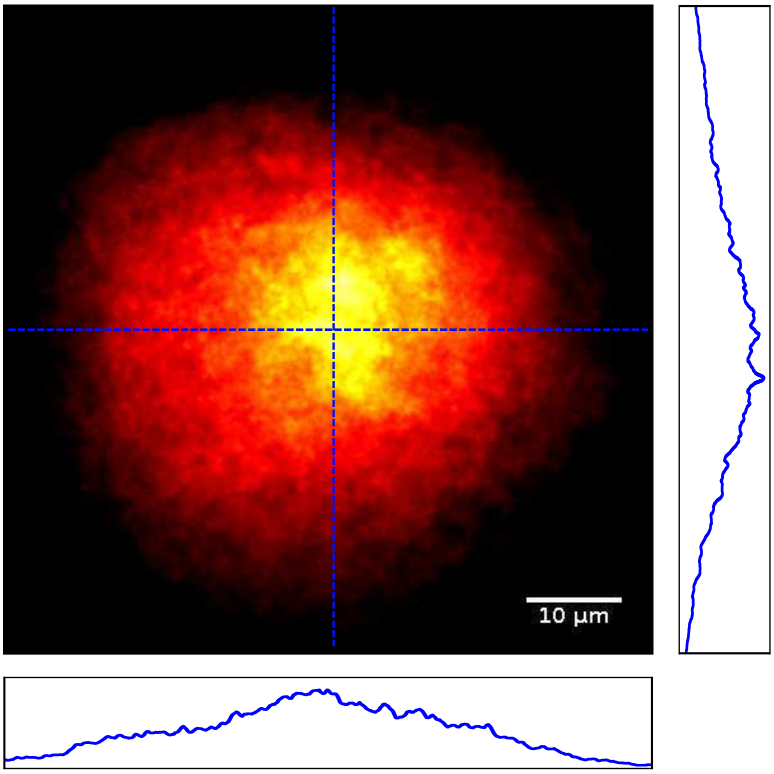

(a) Illumination intensity pattern and orthogonal centered intensity profiles.

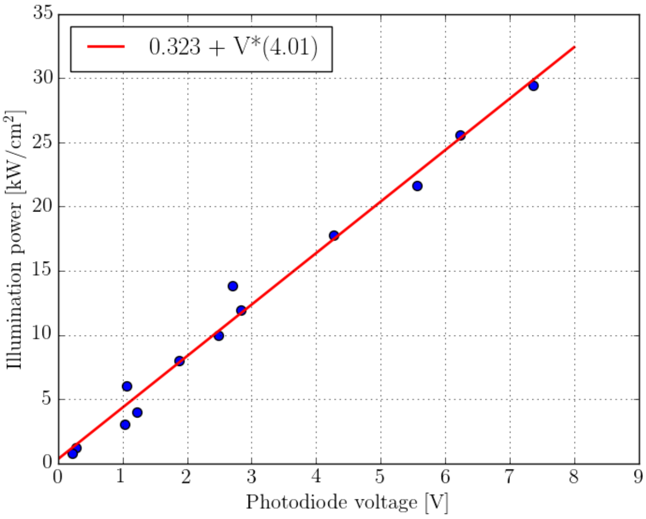

(b) Intensity calibration curve.

Figure 3.2: Illumination profile and power calibration for the 642 nm laser.

age reading is calibrated to deliver P_{BFP}, and therefore I through Equation 3.1. Figure 3.2(b) shows the intensity calibration for the 642 nm laser.

The illumination homogeneity was evaluated within a squared region of 128x128 pixels (the area usually used for localization nanoscopy measurements) so that its standard deviation would represent no more than 10% of the intensity mean. Under this condition, the intensity value was considered as representative of the whole acquisition region.

TIRF illumination intrinsically cause an up to 4-fold intensity increase on the sample[141]. This effect was taken into account by comparing the mean intensity of the sample in both TIRF and straight widefield modes. Usually, an increase of around 3 is obtained, consistent with a circular polarization beam at the sample.

3.1.2. Emission path

The objective lens Olympus PLAPON 60x was chosen for its high fluorescence transmittance and high numerical aperture (1.42). These features ensure the highest possible number of collected photons which, as discussed in Section 2.1, maximizes the single-molecule localization precision.

Collected fluorescence light is separated from the illumination by the quad-edge multiband mirror DM3 (Semrock Di03-R405/488/532/635-t1-25x36). The use of a multiband mirror allows to perform simultaneous multicolor fluorescence measurements. Any remaining laser light is further filtered by the quad-notch filter NF (Semrock NF03-405/488/532/635E-25).

The lens L9 is the original tube lens of the Olympus microscope stand. Since a custom detection system was built, the lens L10 (Edmund Optics, $f = 75$ mm vis/nir antireflex coating) is needed to recollimate the emission light. A manual rectangular aperture AP (Ealing) is placed at the focal plane between L9 and L10.

For single-color acquisitions, the dichroic mirror DM5 is removed from the beam path and a suitable emission filter E_T (e.g. Chroma ET700/75m, for the fluorophore Alexa Fluor 647) is used to match the emission spectrum of the dye and block light from other sources.

The lenses L10 and TL_T ($f = 150$ mm) are commonly known as “relay lenses” and are useful to change the magnification of the microscope. They compose a 2x telescope so that the total magnification of the optical system doubles the original 60x. Given that the physical pixel size of the EMCCD camera Andor iXon3 897 (DU-897D-CS0-#BV) is 16 μm, the total magnification M_T brings the image pixel size to $\frac{16\,\mu\text{m}}{120} = 133$ nm. This is close to the optimal value for localization nanoscopy of roughly the σ of the PSF[47, 55].

3.1.3. Focus stabilization

A custom focus stabilization system was built as shown in Figure 3.1. It relies on the reflection on the sample of an infrared laser in total internal reflection configuration, as outlined in Section 2.4.

A diode laser emitting light with its peak intensity in 808 nm is first coupled into a polarization-maintaining single-mode optical fiber (Thorlabs P3-405BPM-FC-2) with a fiber collimator (Schäffer+Kirchhoff 60FC-4-A7.5-01) to spatially filter the beam. Due to the original multimode state of the beam, its power is reduced from the initial 30 mW of power to around 2 mW within the fiber.

Light coming out of the fiber is collimated with an identical fiber collimator in order to obtain a beam with diameter of roughly 1 mm. Next, the light is spectrally filtered with the clean-up filter CF_{808} (Chroma ZET808/15x). Lenses L7 and L8 (Thorlabs with near infrared antirreflection coating, both $f = 50$ mm) and M8 compose a beam scanner that allows the displacement of the beam parallel to the objective axis. The beam is coupled to the illumination path through reflection in dichroic mirror DM4 (Semrock FF750-SDi02-25x36). As depicted in Figure 3.3, the beam is aligned in objective-based total internal reflection configuration so that any change in the objective-sample distance causes a displacement of the reflected beam, which is monitored with an inexpensive complementary metal–oxide–semiconductor (CMOS) camera.

The center-of-mass position of the beam on the CMOS camera is used as the feedback for a PID control system for the stabilization of the microscope focus. The displacement is corrected by moving the fine microscope focus knob with a stepper motor (Prior ProScanIII controller plus the motorized focus drive accessory). This motor is also used to calibrate the relation between the axial displacement of the sample and the beam displacement on the CMOS detector.

Figure 3.4 shows the performance of the stabilization unit. The need for an active control of the focus is evident from Figure 3.4(a): without stabilization, the sample experiments periodical excursions of about 4 μm in the axial direction. This is more than enough to bring the sample out of focus during the course of a localization nanoscopy experiment. Figure 3.4(b) shows the sample position over

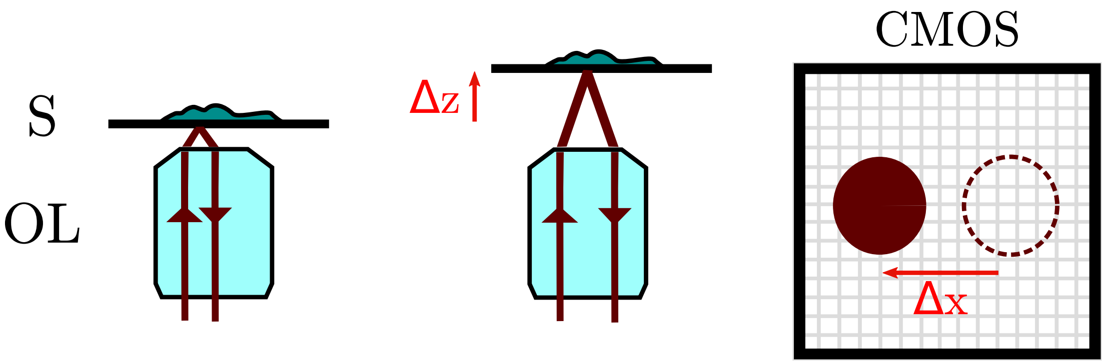

Figure 3.3: Sample axial displacement measurement principle. Changes in the objective-sample distance cause the reflected beam to laterally shift on the detector. S: sample, OL: objective lens, CMOS: camera detector.

time with the stabilization unit turned on. Here, $z = 0$ nm was defined equal to the desired stabilized position. The system effectively locks the focus position to $z = 0$ nm with a standard deviation always below 40 nm for an unlimited amount of time. Finally, Figure 3.4(c) shows the response of the stabilizer to a sudden drift from the desired position. The system returns to focus within 1-2 s.

3.2. Alignment

What follows is a step-by-step guide to align the nanoscope light paths. The illumination, detection and focus stabilization parts are treated separately.

3.2.1. Illumination

As a first coarse alignment, without L4 and L5 in the beam path, the illumination lasers should be aligned to pinholes in the L4-L5 direction in the order of increasing wavelength. This is important to avoid undoing the alignment of a laser when working on the next one. The 405 nm laser should be beam-walked with mirrors M4 and DM2, the 532 nm with M3 and DM1 and the 647 nm with M1 and M2. Next, L4 and L5 should be installed and the alignment of each laser fine tuned for them to remain coaligned. The distance between L4 and L5 should be such that the 532 nm laser is collimated after the telescope as checked with a shear plate. The last step of coalignment is installing L1 and L2 so that the 647 nm laser is collimated after L4 and L5 telescope.

Next, the lasers should be aligned parallel to the direction of movement of

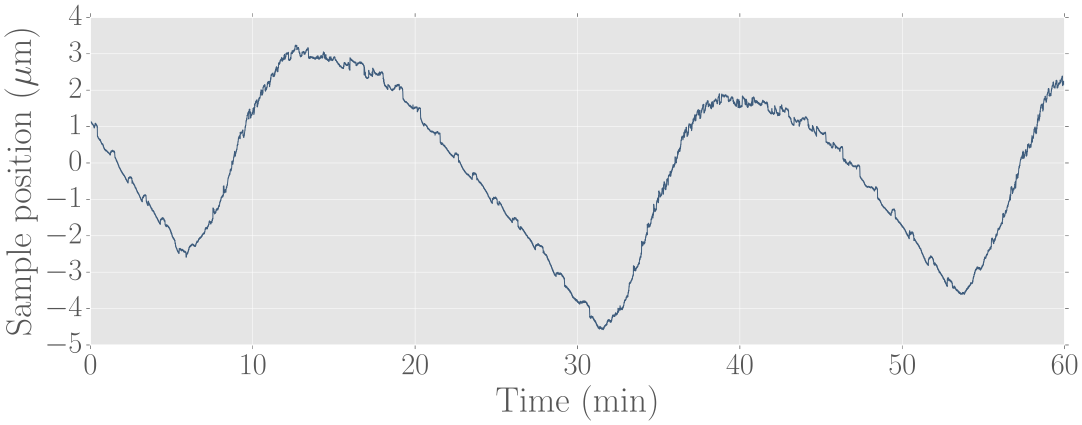

(a) Sample axial drift over the course of an hour.

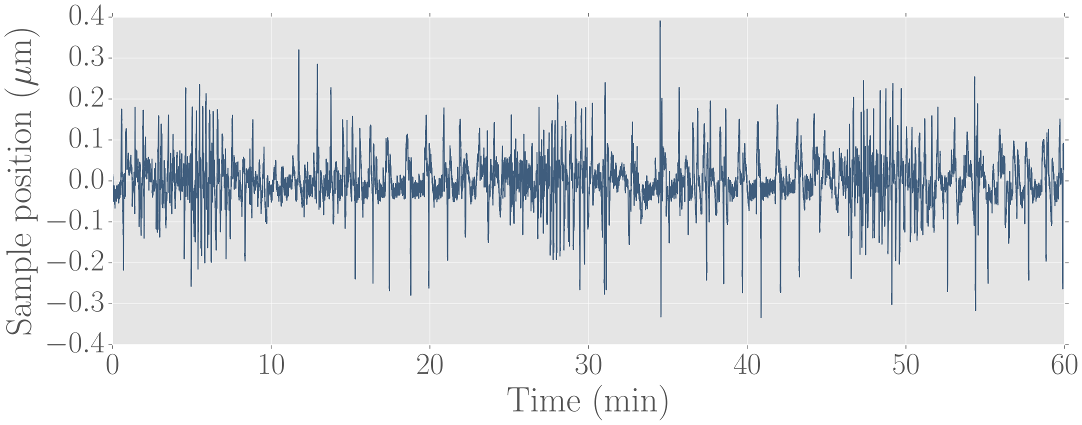

(b) Stabilized axial position over time.

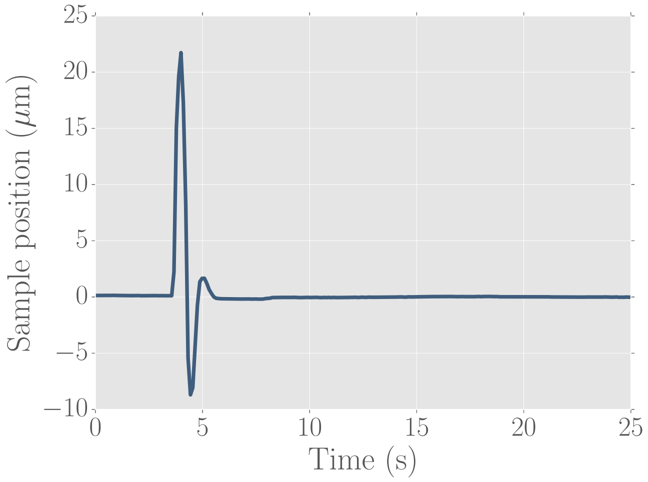

(c) Stabilizer response to a sudden excursion from the set point.

Figure 3.4: Axial position of the sample over one hour without (a) and with (b) focus stabilization. (c) shows the stabilizer response to a sudden drift from the desired position.

the TIRF platform. To this end, one can beam walk with mirrors M5 and PM2 and using as pinholes the iris aperture IR with the stage placed at its extreme positions. PM1 has only one degree of freedom and therefore it is not useful for alignment but only for redirecting the beam upwards.

Without L6 and replacing the objective lens OL for two pinholes placed as further away as possible, M6 and M7 are used for directing the beam vertically and through the center of the objective aperture. L6 should be installed in the lateral position that modifies the direction of the beam as little as possible. With the OL in the beam path, L6 position along the optical path should be such that the illumination focuses at the center of the BFP. There are two ways of ensuring the position is correct. One can look for the axial position that minimizes the size of the transmitted beam through the OL. Also, using a mirrored sample the reflected beam should be collimated after returning to L6. This is because OL and L6 constitute a telescope if the beam focuses at the BFP of the objective.

The final step consists of ensuring each laser reaches the sample with circular polarization. To this end, one can replace the objective lens with a polarizer and a photodiode. By turning the polarizer, the signal on the photodiode should remain constant. The lasers have independent quarter-wave and half-wave plates to control the polarization state of each one.

3.2.2. Detection

First, the detection area should match the illuminated area. To that end, one can take the OL off and attach the output of an optical fiber to its mounting aperture. If the fiber output runs perfectly vertical and centered, this beam can be used to mock the emission light path.

L10 is placed so that the emission beam coming out of the microscope is collimated with its original direction unaltered. Then, M12 and M13 redirect the beam perpendicular to the direction between the camera and TL_{T} centers. The TL_{T} position in z is such that the emission beam is focused at the camera. To correctly place M14, M15 and M16 one can use a beamsplitter instead of DM5 and work with the reflected beam. This beam should reach the camera chip displaced from its center so that the transmitted and reflected channels can be imaged simultaneously. As a first approximation, TL_{R} should be placed so that it focuses the reflected beam on the camera. After this first alignment, a multicolor bidimensional sample must be imaged with the same DM5 dichroic and emission filters that would be used for subsequent multicolor acquisitions (see Section 3.4.3). Under those conditions, TL_R should be placed in the position that focuses the same object plane seen on the transmitted channel. This step ensures the compensation of chromatic aberration between channels. At this point, M14 and M15 probably need a final tuning to properly center the reflected channel on the side of the camera chip.

3.2.3. Focus stabilization system

First, the beam from the infrared laser diode has to be correctly coupled to the monomode fiber so that there is at least 1-2 mW at its output.

M8 should be placed at the focus plane of L7. The position of L8 should be such that the transmitted beam is collimated. Next, the objective should be removed from the objective lens turret and replaced by an IR fluorescing alignment disk. M9 and M10 can then be used for ensuring the beam is directed vertically through the objective lens turret and ≈ 3 mm from the center. This way, the beam transmitted through the objective lens will approach the sample at an angle greater than (or at least close to) the critical angle of the interface. The upward direction of the beam defined by M9 and M10 should be such that the reflected beam travels roughly at the same height from the optical table than the incoming beam, so that they can be separated with the d-shaped pickoff mirror M11.

Placing a mirror at the sample plane and using an infrared viewing card, the CMOS camera can be roughly centered on the beam.

Since M8 is placed at the shared focus of L7 and L8, changing its angle causes a parallel translation of the output beam that can be used to shift its position at the back aperture of the objective lens towards the total internal reflection area. For this, a normal sample should be mounted on the microscope stage, focused and M6 should be moved to maximize the intensity of the signal at the CMOS camera.

3.3. Control software

The custom software *Tormenta* was developed for integrating the control of instruments of the setup through a common graphical user interface (GUI) and for performing analysis routines[142].

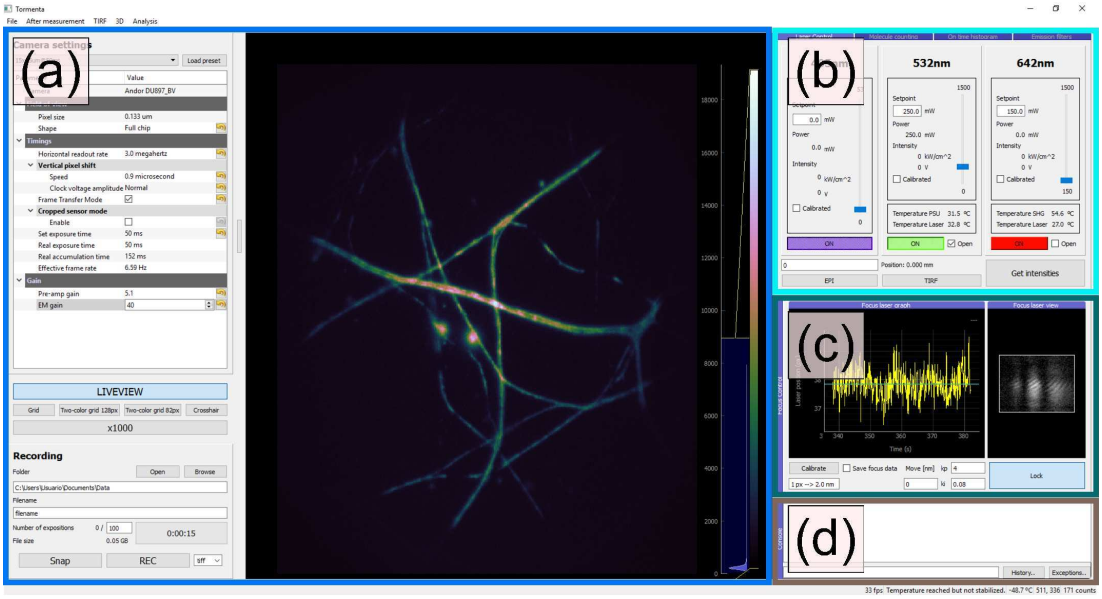

Camera Andor DU897_BV

Pixel size 0.133 um

Shape Full chip

Horizontal readout rate 3.0 megahertz

Vertical pixel shift

Speed 0.9 microsecond

Clock voltage amplitude Normal

Frame Transfer Mode ☑

Cropped sensor mode

Enable ☐

Set exposure time 50 ms

Real exposure time 50 ms

Real accumulation time 152 ms

Effective frame rate 6.59 Hz

Pre-amp gain 5.1

EM gain 40

Folder C:\Users\Usuario\Documents\Data

Filename filename

Number of expositions 0 / 100

File size 0.05 GB

0:00:15

tiff

Setpoint 0.0 mW

Power 0.0 mW

Intensity 0 kW/cm^2 0 V

☐ Calibrated

532nm: Setpoint 250.0 mW; Power 250.0 mW; Intensity 0 kW/cm^2 0 V; ☐ Calibrated; 1500 / 0; Temperature PSU 31.5 ºC; Temperature Laser 32.8 ºC; ☑ Open

642nm: Setpoint 150.0 mW; Power 0.0 mW; Intensity 0 kW/cm^2 0 V; ☐ Calibrated; 1500 / 150; Temperature SHG 54.6 ºC; Temperature Laser 27.0 ºC; ☐ Open

0

Position: 0.000 mm

☐ Save focus data

Move [nm] 0

kp 4

ki 0.08

1 px --> 2.0 nm

33 fps Temperature reached but not stabilized. -48.7 ºC 511, 336 171 counts

Figure 3.5: Main screen of Tormenta and its modules: (a) camera control and view; (b) illumination control; (c) focus stabilization system; and (d) Python console.

Tormenta consists of a number of routines written in Python 3. The GUI was created with extensive use of PyQt[143], a Python binding of the GUI toolkit Qt, and PyQtGraph[144], a GUI library optimized for live scientific applications. The code is maintained at a GitHub repository[145], including a readme file with detailed instructions for running it under Windows and Linux.

Instrument drivers and library wrappers were taken from free online repositories, when available[146, 147]. Otherwise, wrappers of the serial commands or DLL instructions were written using Python packages pyserial and ctypes, respectively, depending on the driver supplied by the manufacturer. These new drivers were written within the lantz framework, an automation and instrumentation toolkit[148].

Figure 3.5 shows the main window consisting of the following modules: (a) camera control and live view, (b) illumination control, (c) active focus stabilization system, and (d) a Python console. The last three are arranged in tabs and can be interactively moved, resized, or detached from the main window during runtime. A standard menu bar at the top gives access to custom file and analysis tools and a bottom status bar provides online information about the camera temperature and frame rate.

The camera control module is divided in four sections (Figure 3.5(a)). The one on the right is the camera image view which displays either the live-view streaming or the last frame acquired. In this example the image is displayed with the cubehelix colormap[149], chosen for its colorblind compatibility and conservation of intensity gradients when printed in grayscale. On the right hand side, an image histogram allows for live tuning of the minimum and maximum brightness levels for optimal image contrast.

The section on the upper-left side groups all camera settings in a pyqtgraph parameter tree. All operating parameters relevant to optical microscopy of an EMCCD camera can be controlled: electron-multiplying gain, field of view (FOV), exposure time, etc. The current version of Tormenta includes a complete driver for the EMCCD Andor iXon 897.

The heading box gives loading/saving functionality of imaging camera parameters.

The FOV menu includes options suited for dual-color imaging. Tormenta includes a routine for calibration and overlay process described in Section 3.4.3. It finds the optimum affine matrix and uses it to directly save the corrected dual-color imaging data. During two-color acquisitions, the image view can be set to dual-view mode that enables independent histograms for each channel, which is especially useful when the intensity and background of each channel are different.

A third section gathers buttons to run control routines such as switching on and off the live-view streaming, superimposing grids or cross-hairs to the image (e.g., useful for optical alignment), and changing in 1000-fold the illumination intensity by moving a motorized filter wheel (e.g., useful for switching from wide-field visualization to acquisition of super-resolution data).

Finally, a section labeled Recording is dedicated to the configuration and triggering of single frame (snap) and multiple frame acquisitions. Localization-based super-resolution microscopy methods often need thousands of frames for the reconstruction of a super-resolved image, hence the need of a saving format capable of handling gigabyte-sized files, such as TIFF and HDF5 formats, both implemented in Tormenta. An additional file containing the entire system configuration is saved alongside the single frame or multiple frame recording.

The illumination control module (Figure 3.5(b)) is meant to control the wavelength, intensity, and mode of illumination. It is able to drive three continuous wave lasers from different manufacturers. Each laser control is instantiated from the same Python class, so it is straightforward to change laser units or add a new one. Besides setting the output power of each one, there is a checkbox for setting the laser's shutter state, i.e., switching on and off any of the illumination sources. The button "Get Intensities" triggers the power measurement of each laser with a photodiode and reports the intensity at the sample using a previous calibration. This module also controls a motorized linear stage (Thorlabs APT Motor) that permits to switch between epi and TIRF. A routine was implemented to automatically find the optimum stage position that maximizes the intensity detected by the camera for TIRF.

In a tab behind "Laser control" there is a module called "Emission filters". It consists of an editable table containing information about the installed fluorescence emission filters, which eventually could be integrated with a control routine for a motorized filter wheel.

The focus-lock module in Figure 3.5(c) is designed to control the custom made focus stabilization unit described in Section 3.1.3. It monitors on the CMOS camera the reflection of the near-infrared laser beam sent to the sample through the objective in total internal reflection configuration. On the left side, a scrolling plot shows online the position of the reflected beam on the sensor. On the right there is a live output of the CMOS camera, which is especially useful during alignment of the near-infrared beam. From this module, one can start the proportional and integrative feedback control system that locks the focus position, as well as modify the proportional and integrative constants.

Finally the GUI of Tormenta includes a Python console module (Figure 3.5(d)) in order to give the user access to the full machinery of Python during runtime.

The software is built in a modular fashion. Its modules can be run independently as stand-alone programs; they can be excluded or replaced according to the experimental requirements. Also, in order to enable its development and test outside the lab, Tormenta includes mocking drivers for each instrument, which are loaded if the instrument is not present and provide a rudimentary simulation of it.

3.4. Image acquisition

In this Section, detailed instructions are described for performing each type of imaging session: single-color 2D and 3D, and dual-color acquisitions.

3.4.1. 2D single-color

The sample preparation is specific of each nanoscopy technique. For fixed biological samples, the localization nanoscopy of choice is STORM. In that case, cells are preferentially cultured in 18 mm coverslips because they can be mounted on microscope slides with a central hollow area, where the imaging buffer can be deposited. Cells are fixed and labeled using standard immunofluorescence protocols (see for example the one in Section 4.4). Alexa Fluor 647-conjugated secondary antibodies are usually used for staining since that is currently best performing fluorophore for STORM[117]. Samples are imaged in a buffer containing 50 mM Tris pH = 8 and 10 mM NaCl supplemented with 10% w/v glucose, 100 mM beta-mercaptoethanol, 1 μg/mL glucose oxidase and 0.5 μg/mL catalase as oxygen scavenging system. This STORM imaging buffer should be prepared immediately before mounting the coverslip onto the microscope slide. See Appendix A.2 for detailed protocols.

Prior to STORM imaging, conventional fluorescence images of the region of interest are acquired with an excitation laser intensity of 10-20 W cm^{-2}. Before STORM data acquisition, the focus of the microscope must be locked to the plane of interest. STORM data acquisition is started by changing the excitation laser intensity to $\approx$ 20 kW cm^{-2}, thus inducing on-off switching of the fluorescent marker in the tens of ms time range, as required by the STORM technique. This 1000-fold intensity increase is performed by removing a motorized neutral density filter from the illumination path through a dedicated button in the software (see Section 3.3). Throughout the whole acquisition, the 405 nm activation laser power is increased from 0 in 10 μW cm^{-2} steps whenever the density of single-molecule events decreases below $\approx$ 1 molecule per μm^2. The activation rate is highly sensitive to the activation laser power, so its intensity is kept always below 1 W cm^{-2}. This is a manual procedure and thus its performance highly depends on the monitoring user. A routine that feeds on the camera image to automatically drive the activation laser intensity was designed and it is currently being implemented. Typically, it takes around 25000 frames at 15 ms of exposition time for each STORM acquisition if the sample is excited at 20 kW cm^{-2}.

The nanoscope can be also operated in TIRF mode. Switching to TIRF illumination is straightforward: the laser widget in Tormenta has a dedicated button for it. This mode greatly reduces background fluorescence but can only be applied to thin samples, given that only fluorophores closer than $\approx$200 nm from the coverslip are illuminated. The illumination intensity on the sample is increased around 3-fold in TIRF mode, as explained in Section 3.1.1.

The mode of operation for the EMCCD camera that maximizes SNR is as follows[150]: first of all, the exposure time is to be set roughly equal to the mean **on** time of the imaged fluorescent dye. A shorter time would effectively divide each single-molecule event in several camera frames. Even though a molecule that appears in successive frames can be identified through software and its photons can be added as if they appeared during a single frame, the camera noise is also multiplied in the process hence losing SNR. An exposure time excessively over the mean on time also makes the overlapping of single-molecule PSFs more likely, thus losing localizations from the subsequent analysis. The horizontal readout rate (HRR) and vertical shift speed (VSS) govern the time it takes for the camera to read the deposited charge after a frame. Higher values means less dead time for the detector but they also bring more readout noise. Therefore, once the exposure time is set, the HRR and VSS must be set to the minimum values that make the accumulation time (the time between camera frames) match the exposure time. To reach very short exposure times it might be necessary to increase VSS to the point image degradation starts to be noticeable. If that is the case, the vertical clock amplitude (the voltage between dynodes) should be increased until the images quality goes back to normal. Finally, the preamp gain should be set to the maximum value that does not produce intensity saturation and the same for the electron multiplying gain until a value of 100x. Increasing the gain beyond that value does not increase SNR and reduces the lifetime of the camera.

Once the acquisition is over, data with an inhomogeneous background should have its background suppressed before localization fitting[112]. Tormenta has a routine for this task that uses a running median filter.

The data analysis and rendering of the final super-resolved image is performed with the ThunderSTORM software[133]. Once the 25000-frame data is loaded in ImageJ, ThunderSTORM is executed with the “Run analysis” dialog. Here, the camera specifications (pixel size, photoelectrons per analog/digital count, base level and electron-multiplying gain) have to be entered in the “Camera setup” menu. The software has several options for the image filtering, approximate localization of molecules, localization method and visualization of results. The analysis configuration chosen for measurements presented in this thesis is detailed

Analysis step	Setting	Parameters
Image filtering	Wavelet	order: 3, scale: 2
Approx. localization	Centroid	threshold: 3*std(Wave.F1)
Sub-pixel localization	Integrated Gaussian PSF	r: 3 px, MLE, sigma: 1.6
Visualization	Normalized Gaussian	magnification: 10

Table 3.1: ThunderSTORM configuration for the data of this thesis.

in Table 3.1. The integrated Gaussian PSF function fitting through maximum likelihood is used because it has been proven to be the most precise localization method[85, 113]. The magnification is chosen to match the approximate improvement in resolution given by localization nanoscopy with respect to conventional fluorescence microscopy. After all single-molecule emissions have been localized, three post-processing routines are used: first, the lateral drift is corrected through correlation analysis. This step is crucial to achieve nanometric resolution. Also, detections of the same molecule in subsequent frames are identified, their signals added and relocalized. Finally, it is possible to plot histograms of any localization result (intensity, position, sigma, etc) to identify wrong localizations and filter them out.

The localization nanoscope has been extensively used in 2D single-color mode at CIBION. Here, two example images are presented: STORM imaging of microtubules of an hippocampal neuron and DNA-PAINT imaging of a calibration sample.

Microtubules are a component of the cytoskeleton of cells. These tubular polymers are found throughout the cell and have typical lengths of 30-40 μm. The outer diameter of a microtubule is about 24 nm while the inner diameter is about 12 nm[151]. Due to their size, they are frequently used for demonstration of nanoscopy resolution capabilities. A sample of hippocampal neuron microtubules was stained with Alexa Fluor 647 through immunofluorescence and imaged with STORM. The illumination for STORM imaging was performed in TIRF mode at 60 kW cm^{-2} of intensity. 30000 frames were acquired at 10 ms each. The resulting image is compared with the conventional fluorescence microscopy image in Figure 3.6. Line profiles across microtubules in the STORM image reveal a FWHM of 30-40 nm. Taking into account that secondary antibodies are $\approx$ 13 nm in size[152], 40 nm is close to the real size of the outer diameter of the microtubules plus the length of the antibodies used to stain the structure. In Figure 3.7, widefield and STORM resolutions are compared through the intensity profile along the green lines in the images of Figure 3.6. It is shown that due to their proximity, a bundle of four microtubules appear as a single one in the widefield image.

The Gattaquant-PAINT Nanoruler is a spatial calibration tool for localization nanoscopes[153, 154]. It is made with the DNA-Origami technology[155] that uses the affinity between complementary DNA bases to fold a circular single-stranded DNA (ssDNA) molecule into complex arbitrary shapes. In particular, the Nanoruler is a 160 nm long linear structure with short ssDNA sequences at the tips and at the middle, as shown in Figure 3.8. These short ssDNA sequences act as capturing strands for complimentary, fluorescently labeled oligonucleotides in solution. Atto655 fluorophores were used as fluorescent labels. The on-off blinking required for super-resolution imaging is achieved by dynamic binding and unbinding of the fluorescently labeled oligonucleotides to the capturing strands on the Nanoruler. The sample was imaged in TIRF illumination mode at 30 kW cm^{-2}. 10000 frames were acquired at 20 ms of exposition time. The final image built from the localizations is displayed in Figure 3.9. A line profile through the image of one of the DNA origami is shown in Figure 3.9(b). The Gaussian fit of one of the docking sites yields a FWHM resolution of 37 nm.

3.4.2. 3D single-color

3D localization was implemented through PSF engineering by adding a cylindrical lens (Thorlabs LJ1516RM-A, $f = 1000$ mm) to the emission path. It was placed between the EMCCD camera and the tube lens $\mathrm{TL_T}$ so that it produced only a slight astigmatism, thus enabling z axis localization of single-molecules without losing significant SNR for the lateral localization. The orientation of the cylindrical lens was tuned so that astigmatism would occur along the camera pixels grid. This maximizes SNR because emitted photons are spread onto the minimum amount of pixels. For a detailed description of the technique see Section 2.1.2.

The astigmatic PSF model chosen for three-dimensional localization is a rotated elliptical Gaussian[133]:

$$I_{EG}\left(x, y|\Theta, \phi\right) = \frac{N}{2\pi\sigma_1(z_0)\sigma_2(z_0)} \exp\left(-\frac{x'^2}{2\left(\sigma_1(z_0)\right)^2} - \frac{y'^2}{2\left(\sigma_2(z_0)\right)^2}\right), \tag{3.2}$$

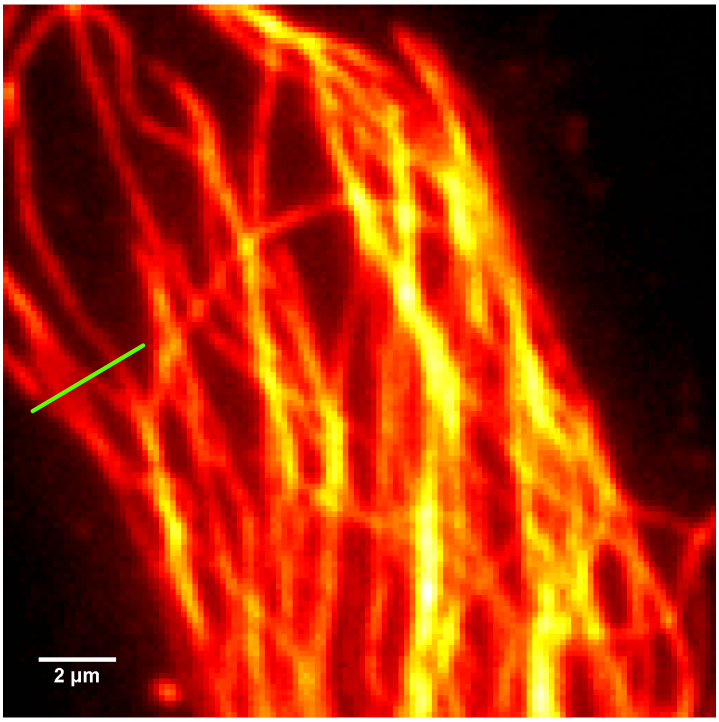

(a)

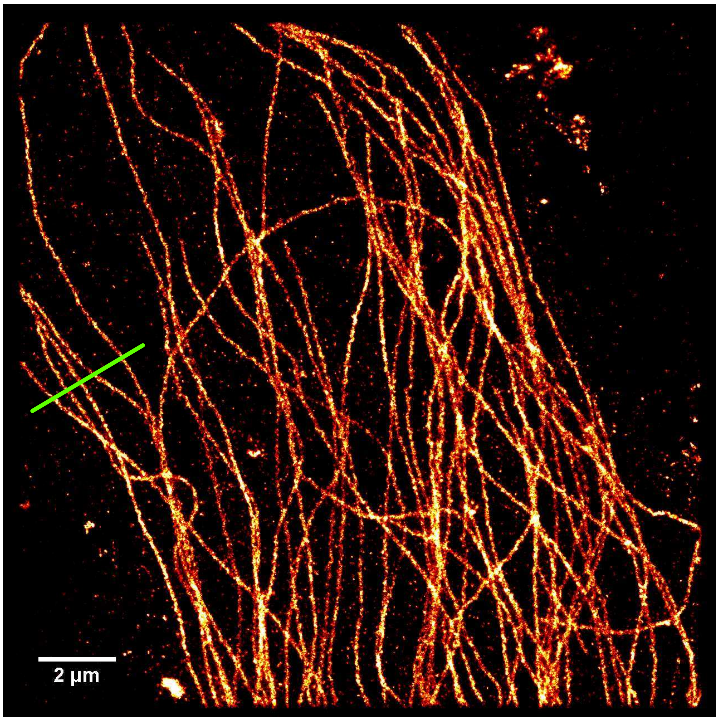

(b)

Figure 3.6: Nanoscopy of the microtubules of a hippocampal neuron. (a) Conventional fluorescence microscopy image taken before starting STORM acquisition. (b) Final STORM image.

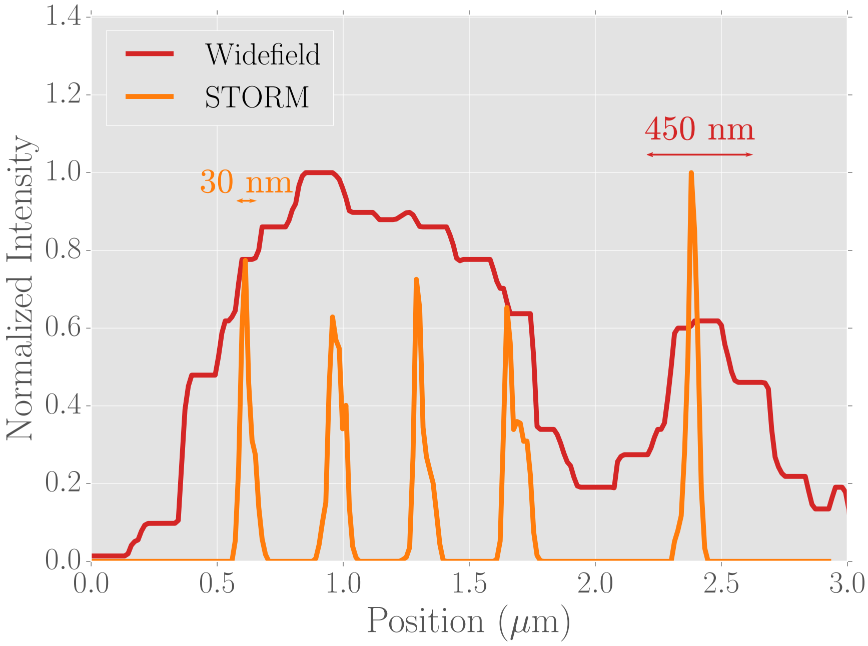

Figure 3.7: Comparison between widefield and STORM resolution. The intensity profiles along the green lines in the images of Figure 3.6 are plotted. FWHM values are also indicated.

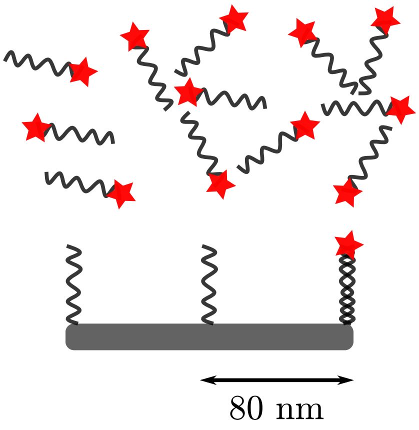

Figure 3.8: Diagram of a Nanoruler DNA origami sample.

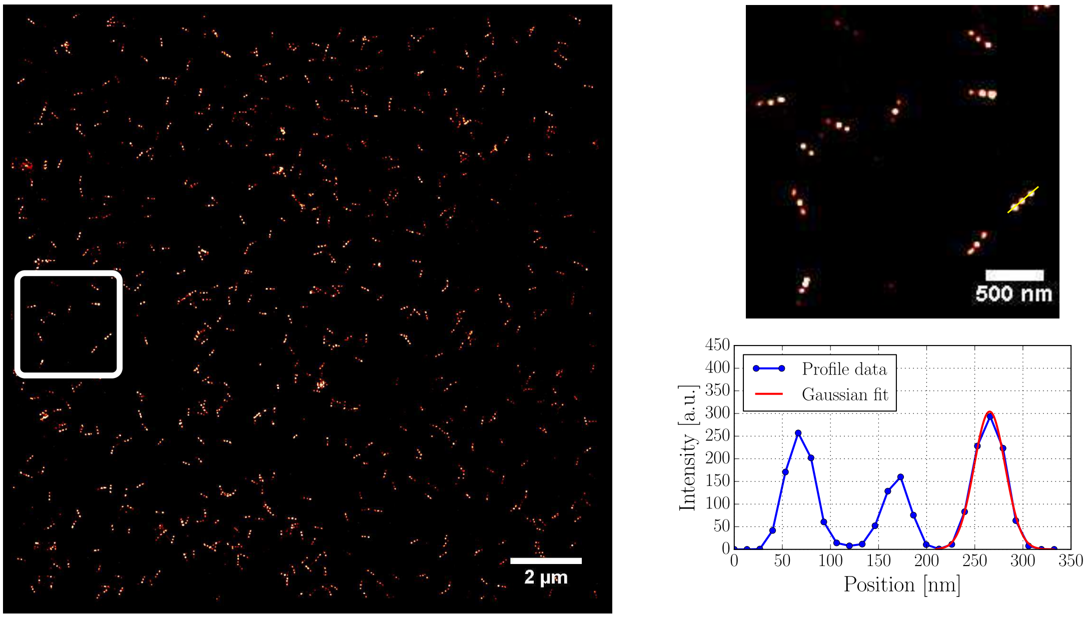

(a) (b)

Figure 3.9: Imaging of a Nanoruler DNA origami sample. (a) is the final nanoscopy image. The squared region is shown in (b), where a line profile along one of the Nanorulers is plotted and one of its docking sites fitted with a Gaussian function. The FWHM was 37 nm.

where

$$x' = (x - x_0)\cos\phi - (y - y_0)\sin\phi$$
$$y' = (x - x_0)\sin\phi - (y - y_0)\cos\phi.$$

$I_{EG}\,(x, y|\Theta, \phi)$ is the expected amount of photons at the detecting position (x, y) for the parameters $\Theta = [N, x_0, y_0, z_0, b]$ (number of emitted photons, the x, y and z coordinates of the molecule and the background signal, respectively). $\sigma_1(z_0)$ and $\sigma_2(z_0)$ are the widths of the molecule in perpendicular axis rotated a ϕ angle with respect to the x and y Cartesian axis.

The widths $\sigma_1(z_0)$ and $\sigma_2(z_0)$ require a model for the defocusing of the PSF in the axial direction[156]. The simplest choice is using quadratic functions, which works well when working around the quadratic functions minima. The model functions are

$$\begin{aligned} \sigma_1(z_0) &= a_1(z_0 - c_1)^2 + b_1 \\ \sigma_2(z_0) &= a_2(z_0 - c_2)^2 + b_2 \end{aligned} \tag{3.3}$$

In order to determine constants $a_{1,2}$, $b_{1,2}$ and $c_{1,2}$, one has to calibrate the PSF widths versus the axial position z_0. To that end a sample of isolated emitters (see a protocol for preparing such a sample in Appendix A.1.3) is translated in the z axis in a range of ≈ 2 μm around the new optical system focus, where the widths are equal. The emitters PSFs are fitted with Equation 3.2 and its widths are fitted according to the model of Equation 3.3. Figure 3.10 shows an example of such a calibration with data taken from several isolated spots to improve the reliability of the calibration. On top of the figure, typical PSFs at the focus, below and above it are displayed. Once $\sigma_1(z)$ and $\sigma_2(z)$ are known, they are used to localize emitters in the z axis during fluorescence nanoscopy imaging.

The custom built acquisition process has a specific routine that takes images at different z planes and outputs an image stack. This data is loaded into ImageJ and the calibration process that yields $a_{1,2}$, $b_{1,2}$ and $c_{1,2}$ is carried out with ThunderSTORM.

Once the cylindrical lens is added to the emission path and the PSF shape is calibrated, the data acquisition process is identical to the bidimensional case. Before the data analysis, the calibration file has to be loaded into ThunderSTORM. This way, it can identify the z position of each molecule imaged during the fluorescence localization acquisition. The three-dimensional fit is performed in the same way as the bidimensional only that the PSF function has an additional fitting parameter: the z coordinate through Equation 3.2.

As an example, a 3D STORM acquisition of microtubules in hippocampal neurons is shown in Figure 3.11. The microtubules were stained with Alexa Fluor 647 through immunofluorescence. Single-molecule emissions were localized in three dimensions using the previous PSF calibration. Figure 3.11(a) shows the conventional fluorescence microscopy image taken before the STORM acquisition. Figure 3.11(b) is the 2D STORM image built by disregarding the z coordinate of the localizations. Figure 3.11(c) shows the 3D STORM final image, where the z position has been encoded in the visualization colormap. The big white square is shown enlarged in Figure 3.11(d), where it is evident from its color that two bundles of microtubules are grouped in different planes. Furthermore, the intensity

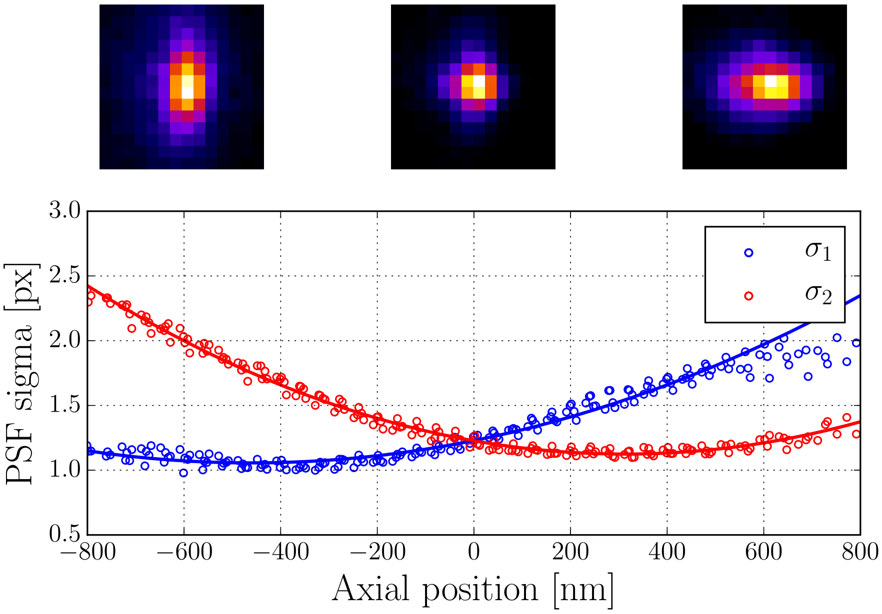

Figure 3.10: Axial position calibration for single-molecule emissions. The plot shows the $\sigma_1(z)$ and $\sigma_2(z)$ of the PSFs of isolated markers. The lines are quadratic fits of the data according to the model of Equation 3.3. Example PSFs are shown on top, roughly aligned with the corresponding axial position they were taken on.

profile along the z axis at the position of the white square of Figure 3.11(c), plotted in Figure 3.11(e). There, signal from two overlapping microtubules ≈ 500 nm apart is shown. The FWHM of one of them is 300 nm, well below the optical resolution limit for the z axis.

3.4.3. Dual-color

Two-color simultaneous nanoscopy imaging was implemented through emission wavelength discrimination. The dyes chosen for staining distinct subcellular structures are Alexa Fluor 568 and Alexa Fluor 647. They were chosen because of the low crosstalk between their emission spectra and their performance for STORM imaging[117].

Both dyes are simultaneously excited with the 532 nm and 647 nm lasers during acquisition. The dichroic lowpass filter DM5 (Chroma ZT647rdc) separates photons emitted from different species. The reflected (R) and transmitted (T) channels have their spectra further filtered by emission filters $\mathrm{EF_R}$ (Semrock 582/75 BrightLine HC) and $\mathrm{EF_T}$ (Chroma ET700/75m) to match the emission spectra of Alexa Fluor 568 and Alexa Fluor 647, respectively. The dyes absorp-

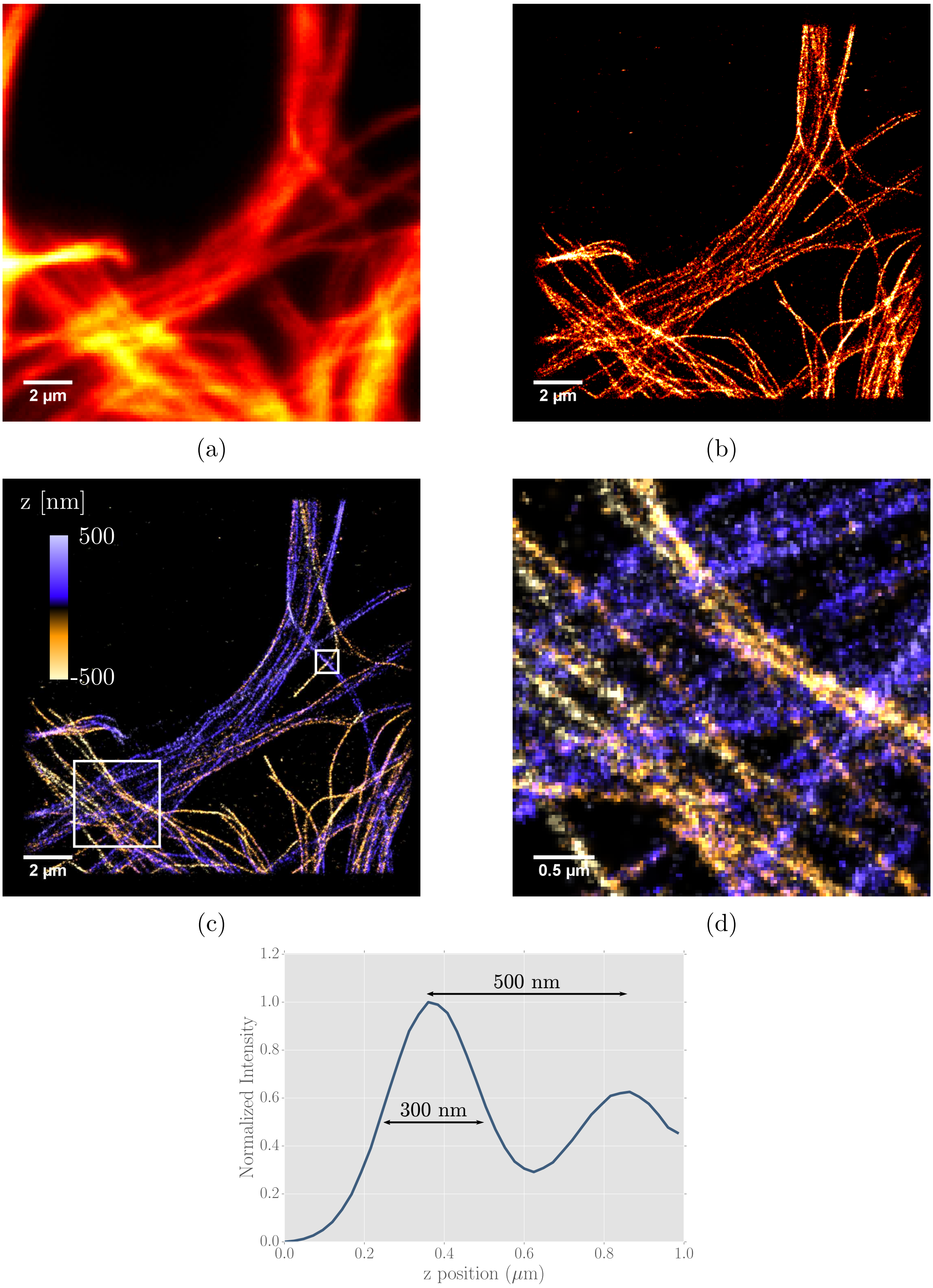

(a) (b) (c) (d) (e)

Figure 3.11: 3D nanoscopy of microtubules in hippocampal neurons. (a) Conventional fluorescence microscopy image. (b) 2D STORM image. (c) 3D STORM image. (d) Big white square region from (c). (e) Intensity profile along the z axis at the small white square region of (c).

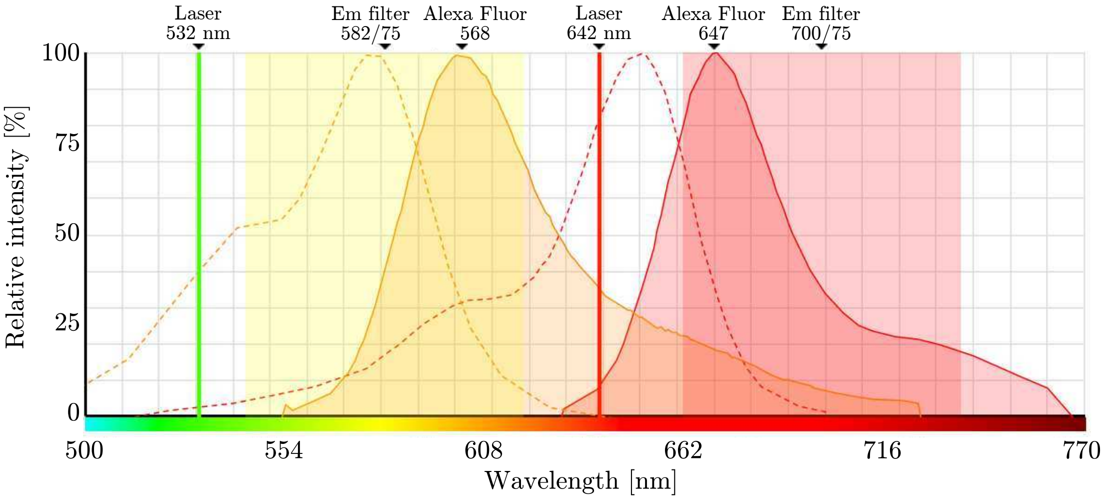

Figure 3.12: Two-color excitation and emission spectral configuration chosen for the built nanoscope. Laser lines at 532 nm and 640 nm are used for exciting Alexa Fluor 568 and Alexa Fluor 647, respectively. The fluorescence is filtered with emission filters with their transmission bands centered in 582 nm and 700 nm.

tion and emission spectra, as well as the transmission spectra of the filters are shown in Figure 3.12. Each channel independently focuses light onto a different region of the camera with its own tube lens $\mathrm{TL_R}$ and $\mathrm{TL_T}$. The use of individual tube lenses makes it possible to compensate optical path differences between the channels due to chromatic aberration. The manual aperture AP limits the FOV to avoid the overlapping of the image of the channels on the camera.

To avoid astigmatism in the reflected channel, DM5 should be specially flat ($\lambda/4$ or better) and it should be mounted without applying any pressure to its front and back surfaces. Failing any of these conditions can result in severe astigmatism and therefore the impossibility of performing reliable single-molecule localization.

Differences in magnification, shear and image rotation between the two channels must be taken into account to obtain an accurate overlay of the final reconstructed images. This is done prior to acquisition by imaging isolated fluorescent markers visible on both channels (Life Technologies Tetraspeck 0.1 μm) (see a protocol for preparing such a sample in Appendix A.1.3) and then finding the affine transformation that minimizes the distance between the same markers as detected in each detection channel. An example of the procedure is shown in Figure 3.13. Figure 3.13(a) is an image of multicolor beads as seen through both channels. Their direct overlay is shown in Figure 3.13(b), where the need to

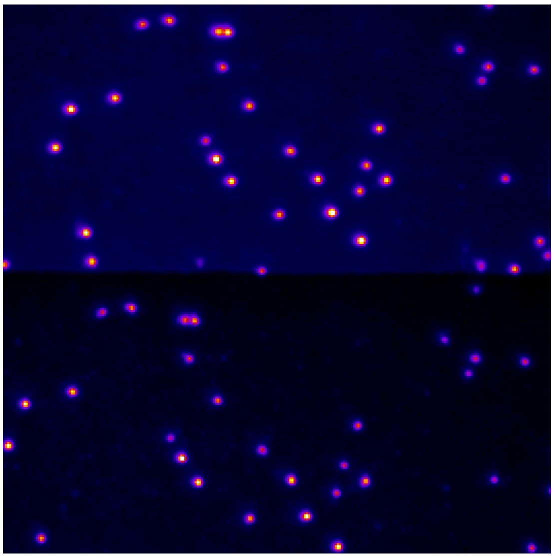

(a) Image of isolated fluorescent beads as seen through both channels.

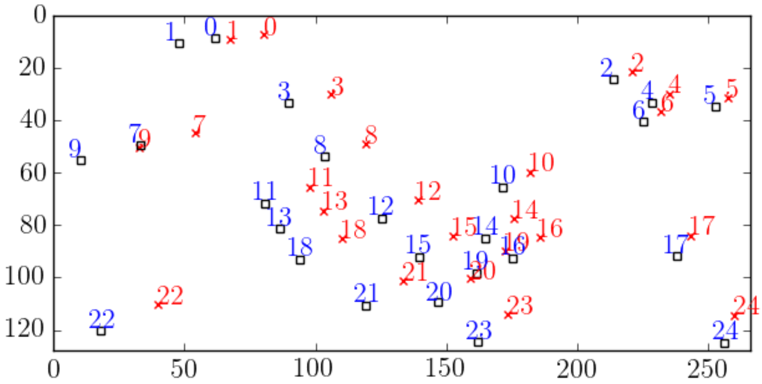

(b) Overlay of the positions of the beads.

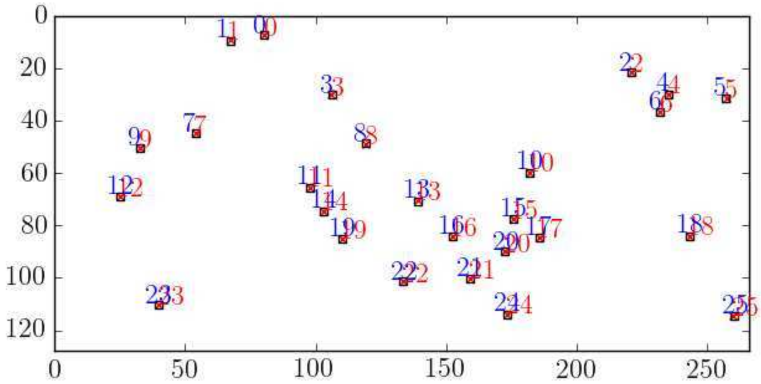

(c) Overlay after affine transformation correction of the T channel.

Figure 3.13: Affine transformation correction procedure for the overlay of channels.

correct for magnification and shear differences is evident. The localized coordinates in either channel are used to calculate the optimal affine transformation as described in [157]. Then, the raw images of the R channel are transformed with the affine matrix. The after-correction localization of the beads in the R channel are correctly overlayed with that of the T channel, as seen in Figure 3.13(c). For this example, the mean distance between localizations in the R and T channels, after affine correction, was 12 nm.

For the calibration to be effective, the exact same FOV has to used for both the calibration and the subsequent acquisition. Tormenta has specific FOV presets for dual-color imaging. When one of the dual-color FOV options is chosen, the software asks for the affine calibration data. This information is used to store already corrected data alongside the raw images from the camera during acquisition.

The rest of the acquisition process is identical to 2D imaging. Since different florophores have distinct switching dynamics, each excitation intensity must be tuned such that the on time of the two dyes is roughly similar. Then, as in single-color acquisitions, the exposition time of the camera should be roughly matched to their on time.

If needed, the system can be adapted for 3D dual-color imaging. A different position for the cylindrical lens must be found because the one described in the previous Section blocks the R channel. Nevertheless, this is a straightforward task.

In the analysis of dual-color acquisitions a background correction algorithm must be performed on the data. This is important because the R channel contributes to the background fluorescence of the T channel. The subsequent data analysis is very similar to the one for single-color acquisitions. The simultaneous approach to dual-color nanoscopy makes it possible to apply the drift correction routine to both channels at once, avoiding any additional drift between each channel acquisitions.

The performance of this multicolor imaging configuration was tested by imaging single color samples and no crosstalk was observed. For a detailed demonstration of two-color nanoscopy imaging, see Chapter 5.

3.5. Conclusions

A fluorescence localization nanoscope was built and its capabilities and operation guidelines were detailed. Its illumination, emission and focus stabilization sections were described along with its specific alignment procedures. It was reported on the custom developed instrument control software features. Particular instructions for imaging with each different mode (2D single-color, 3D single-color and simultaneous dual-color) were described and typical results were presented. In these results, a lateral resolution of 40 nm was reported.

Nanoscopio de fluorescencia por localización

El nanoscopio fue construido alrededor de un estativo de microscopio Olympus IX73. Se muestra un diagrama completo de sus componentes en la Figura 3.1.

Las fuentes de excitación son: dos láseres de onda continua de 1.5 W, uno de 642 nm (pensado para excitar Alexa Fluor 647) y otro de 532 nm. Además, se usa un láser de diodo de 50 mW y 405 nm de longitud de onda para reactivar fluoróforos de acuerdo con la técnica STORM. Se coalinean los láseres por medio de espejos dicroicos y se los expande en conjunto. Luego, se los enfoca en el plano focal anterior de un objetivo Olympus PLAPON 60x de alta apertura numérica para iluminar la muestra en modo campo amplio. Una plataforma permite mover el haz para pasar a modo de iluminación TIRF.

La emisión de fluorescencia se desacopla de la luz de excitación por medio de un espejo dicroico multibanda y luego se filtra con un filtro *notch*. Un par de lentes dispuestas antes de la cámara Andor iXon3 897 forman un telescopio 2x para adaptar el tamaño del píxel a 133 nm, cercano al óptimo para localización de moléculas individuales[47, 55].

Se implementó localización axial mediante la adición de una lente cilíndrica al camino de emisión. Se calibró el astigmatismo con una muestra de moléculas fluorescentes dispersas sobre un sustrato (ver Figura 3.10). Luego se usó esta calibración para obtener imágenes de superresolución en 3D de microtúbulos en neuronas hipocampales (ver Figura 3.11).

Se implementó la nanoscopía a dos colores con adquisición simultánea y discriminación por longitud de onda de emisión. Los fluoróforos elegidos fueron Alexa Fluor 568 y Alexa Fluor 647. Cada canal es enfocado en una región distinta de la cámara, por lo que para su correcta superposición es necesaria una calibración con marcadores visibles en ambos canales (ver Figura 3.13). Para una demostración detallada de la performance del sistema a dos colores, ver Capítulo 5.

Se construyó un sistema de estabilización del foco del nanoscopio basado en la reflexión en la muestra de un haz IR alineado en modo reflexión total interna. El sistema de control está realimentado por la posición del haz en una cámara CMOS y actúa con un motor sobre la perilla fina del foco del estativo Olympus. El sistema permite la estabilización del foco con una desviación estándar siempre menor a 40 nm por un tiempo ilimitado (ver Figura 3.4).

Se diseñó un *software* de control integrado de los instrumentos del nanoscopio llamado Tormenta[142]. Se lo muestra en la Figura 3.5. El *software* automatiza funciones necesarias para la toma de imágenes, como el sistema de control de foco, la calibración en el eje axial y en el sistema multicolor, entre otras. Incluye *drivers* de simulación de instrumentos para la prueba fuera del laboratorio.

Para la toma de imágenes de STORM, las muestras deben prepararse en cubres redondos de 18 mm de diámetro de manera que puedan montarse en portamuestras de vidrio con una hondonada central donde se deposita el buffer de STORM. Para imágenes a un único color, se marca la estructura de interés con Alexa Fluor 647. La adquisición de imágenes por localización estocástica se realiza excitando la muestra a ≈ 20 kW cm^{-2}, de manera de inducir la transición entre los estados de encendido-apagado propios de la técnica. Durante la toma de imágenes se incrementa progresivamente la potencia del láser UV cada vez que la concentración de emisiones de molécula única disminuye por debajo de ≈ 1 molécula por $\mu\mathrm{m}^2$. Cada adquisición suele tomar unos 25000 cuadros a 20 ms de tiempo de exposición. El análisis para obtener la imagen final se lleva a cabo con el *software* ThunderSTORM[133].

Chapter 4

Visualization of periodic structures in the cytoskeleton of neurons

4.1. Introduction

The technological advancement that fluorescence nanoscopy has meant for the biological sciences is providing unprecedented insight into already well-studied systems. This is the case of the neuronal cytoskeleton. The improvement in imaging resolution has allowed to unveil a periodic cytoskeleton that was first observed in the axons of hippocampal neurons by Zhuang and colleagues[158]. As schematically depicted in Figure 4.1, it is composed of actin, spectrin and associated proteins, organized in ring-like structures around the circumference of axons and are repeated along the axonal shafts with a periodicity of around 190 nm. Subsequent studies have shown that the periodic structure is also present in dendrites[159, 160] and in a broad range of neuronal cell types and animal species[161, 162].

Detailed studies based on nanoscopy imaging proved that the periodic lattice is progressively established during the maturation of neurons. The periodicity of βII spectrin in axons starts as early as DIV2 (second day *in vitro*) and it is assembled in a proximal-to-distal fashion[159]. However, the periodic actin structure was only visualized at DIV5 becoming clearly evident after DIV7 [163]. The regularity of the structure is poorer in dendrites than in axons, probably due to a lower local concentration of βII spectrin[159]. The role of βII spec-

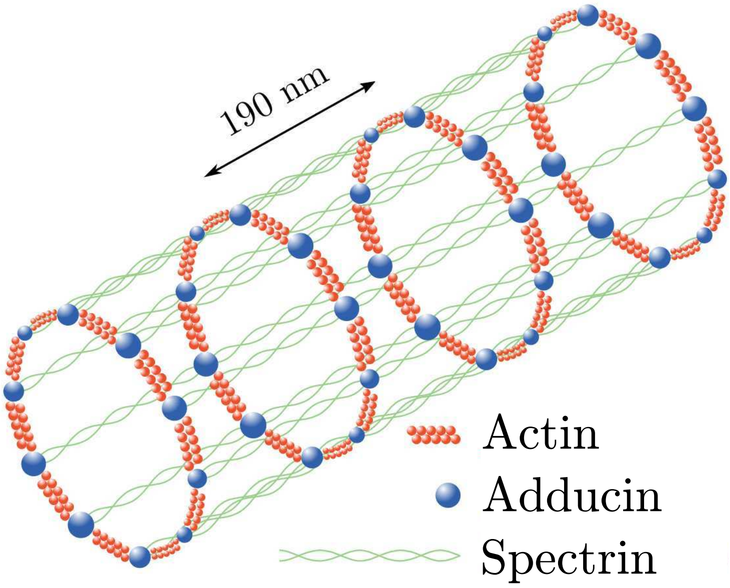

Figure 4.1: Schematic representation of the periodic structure in the cytoskeleton in neurons, as proposed in [163]. Image adapted from [164].

trin was confirmed by observing the periodic structure in dendrites upon overexpression of βII spectrin and also because knocking it down led to a loss of the periodic distribution[159]. It was also shown that depolymerization drugs like cytochalasin D and latrunculin A quickly disrupted the periodic distribution of βII spectrin and actin filaments. Also, it was recently revealed that the lattice is discontinued at synaptic sites[165].

The function of the actin/spectrin periodic structure is still a matter of speculation. It has been reported through single-particle tracking that membrane protein motion is confined to a repetitive pattern of 190 nm-spaced segments that match the underlying actin lattice in hippocampal neurons[166]. Nevertheless, a significant amount of work is still necessary before the function is completely understood. It is yet unknown, for example, how the actin/spectrin periodic structure in axons responds to physiological (i.e. electrical activity) or pathological (i.e. injury, excitotoxicity) stimuli.

Such studies require methods for quantitatively assessing changes in the periodic structure. So far, autocorrelation analysis with manual selection of regions–of-interest has been employed. It was used to quantify the “degree of periodicity” of spectrin in different segments of axons[159] and also for comparing between axons and dendrites[162]. This approach has severe limitations. Firstly, it requires the observer to handpick the region of interest with the risk of introducing a subjective bias. Secondly, such a task is highly time-consuming, which in practice limits the number of neurons that can be analyzed. Hence, quantitative studies of the periodic structure call for a specific image analysis tool to overcome this two major drawbacks.

For this purpose, an open-source image analysis tool for the quantification of changes in periodic structures was developed. The software, called Gollum, automatically finds and analyzes periodic arrangements in an image. Its output includes the abundance and distribution of the periodic structures as well as a measure of the degree of regularity in comparison to an "ideal" periodic arrangement.

The software is described in Section 4.2. Proof-of-principle tests are run on STORM images taken with the localization nanoscope described in Chapter 3. The strategy for detecting the degree of periodicity of an image and the analysis performed on multiple images of the same sample are detailed in Sections 4.2.1 and 4.2.2, respectively. Then, in Section 4.3, Gollum is applied to assessing the effect of the herbicide Paraquat on the spectrin structure. The statistical methods employed by the software are provided in Section 4.5.

4.2. Gollum

Gollum, the ring finder, is entirely written in Python 3 with Qt as the graphical user interface framework, making it cross-platform. The code is maintained at a public GitHub repository[167].

The aim of the software is to automatically quantify the fraction of the sample exhibiting a given regular structure defined by the user. The general idea is to rate the image in terms of its similarity to a synthetic reference pattern. In the particular case of the subcortical neuronal cytoskeleton, the goal is to quantify the fraction of neuronal mass exhibiting the 190 nm periodic spectrin structure (PSS). This quantity will be called "PSS fraction". It is important to note here that the reference pattern can be easily changed to any bidimensional function to suit different purposes than the one that drove this research, and quantify the presence of arbitrary structural patterns.

The code includes two executable programs. They make use of the same underlying algorithms but serve different purposes. GollumDeveloper is used for testing the analysis on individual subregions of an image in order to fine tune the parameters of the program. Once these parameters are chosen so that the software correctly characterizes the image structure, Gollum is then used for automatic bulk processing of as many images as necessary to gather significant statistics.

In Section 4.2.1, the algorithm that characterizes the quality of the periodic structure in every single subregion of an image is described. In Section 4.2.2, it is shown how it extracts information from a whole data set composed from multiple images.

4.2.1. Quantification of periodic structures

The analysis workflow for each individual image can be outlined as follows: first the neuron is discriminated from the background fluorescence. Then the image is divided into subregions of equal area, typically 1 μm^2. Those subdivisions which contain less than a certain neuronal content are not analyzed. The remaining subregions are compared to the reference pattern and a measure of the degree of similarity is calculated.

In order to identify neurons in an image, a Gaussian filter is first applied to get a continuous signal even when the image exhibits sharp features and for smoothing out small bright spots that should be considered background. GollumDeveloper is used to choose the appropriate Gaussian filter sigma and intensity threshold to adequately discriminate the neuron from background. A sigma of 100 nm and a discrimination intensity of half a standard deviation above the mean intensity of the image works well for STORM images. All pixels with an intensity above this threshold are considered as part of a neuron. A binary image indicating neuron presence at each pixel is built to be used later in the algorithm. It is called the neuron discrimination image.

Next, to be able to locally analyze the degree of periodicity, the image is divided into subregions. The suitable size for them depends on the periodicity of the structure of interest. For this study, a size of 1 μm x 1 μm was chosen because the spectrin/actin periodic structure in neurons has a periodicity of around 190 nm. A smaller subregion size is not convenient because the image must contain a few periods of the periodic structure to enable a reliable identification. Taking larger subregions is also detrimental for the analysis because the method relies on making a good estimate of the local direction of the axon or dendrite. As the size of the subregions increases, so does the chance that an axon (or dendrite) takes a curved morphology, or crosses another axon (or dendrite).

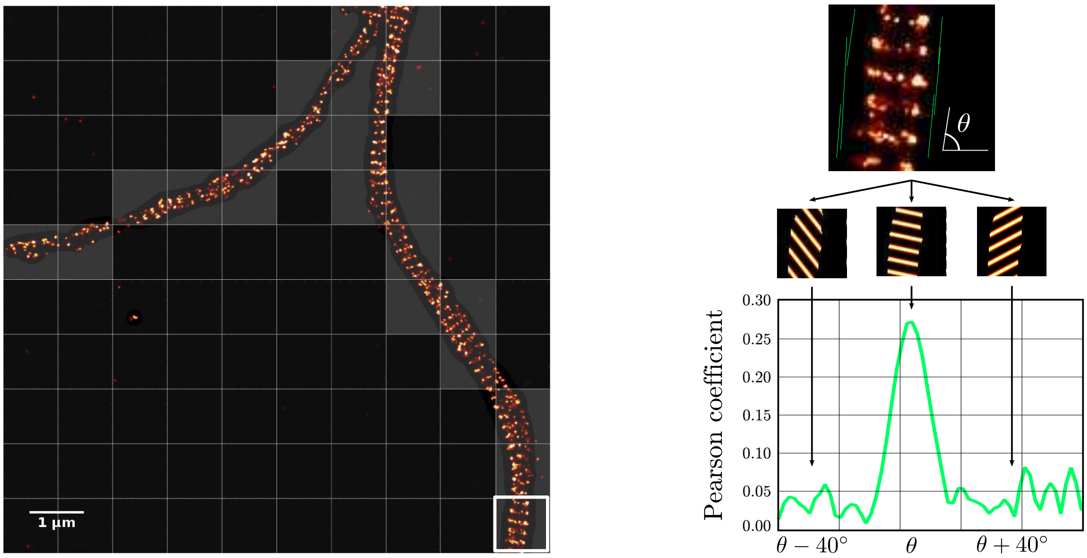

(a) (b)

Figure 4.2: Gollum workflow. (a) Neuron discrimination example. Subregions in gray have enough neuron mass to be analyzed. (b) Analysis for the subregion in the white square in (a). The Pearson correlation coefficient between subregion and reference pattern is calculated at different angles. The maximum matches the inclination of the pattern.

Once the image is divided, subregions with less than a certain percentage of its area occupied by the neuron are discarded from further analysis. This area threshold is tuned from GollumDeveloper and a value of 20% was proven effective for the performed analysis. An example of the neuron discrimination image is shown in Figure 4.2(a) for a STORM image of spectrin in hippocampal neurons. Here, the subregions in gray have sufficient neuron content to be considered in the analysis.

Figure 4.2(b) shows the analysis of an example subregion taken from the bottom right corner of the image in Figure 4.2(a). For the method to correctly asses the quality of the periodic structure, the direction angle θ and phase ϕ of the reference pattern must match those of the data. To estimate the direction of the neuron, the software detects lines along the edges between neuronal and not neuronal material (green lines in the upper image of Figure 4.2(b)). If all or nearly all the detected lines have similar angles (as it is the case of the example), the direction of the neuron is simply estimated as the average of their angles. If the detected lines have angles that group into more than one similarly-sized clusters, the algorithm interprets that more than one neuron is present and the

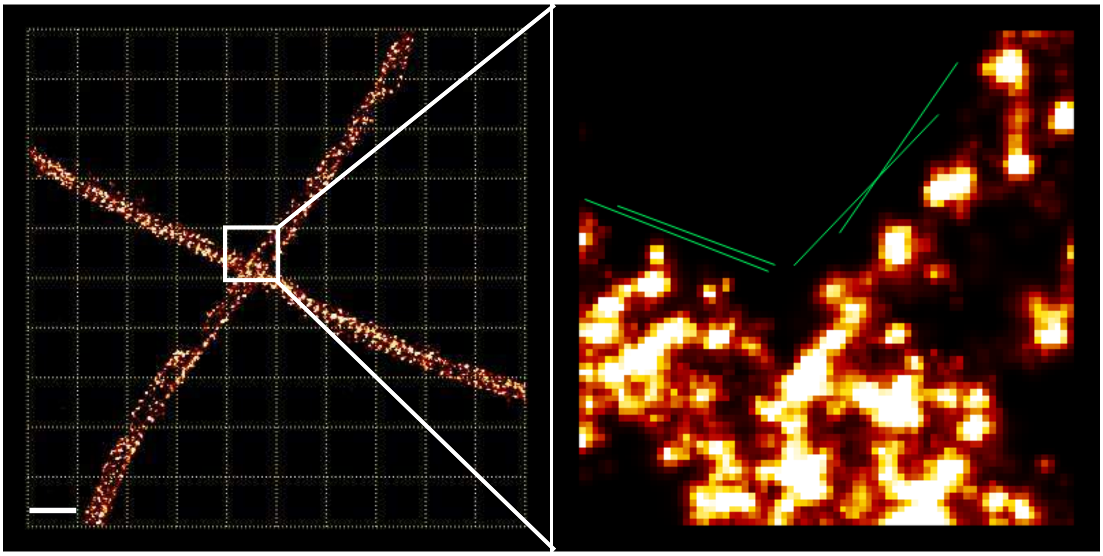

Figure 4.3: Strategy for discarding subregions with crossing axons.

subregion is discarded. An example of such case is shown in Figure 4.3, where the strategy successfully identifies the crossing of two axons.

The reference pattern is a bidimensional function $f(x, y)$ such that

$$f(x, y) = \sin^n x, \tag{4.1}$$

with x as the direction parallel to the direction of the neuron. The power n is tuned from GollumDeveloper. $n = 6$ was chosen to approximately match the duty cycle of the observed PSS. Nevertheless, the software is currently being improved to directly build $f(x, y)$ from the expected distribution of the protein under study.

The similarity between data and reference pattern is assessed by calculating the Pearson correlation coefficient R between them, within the area with neuronal mass. In order to make sure they are correctly overlayed, R is calculated for a range of θ and ϕ of the reference pattern. The maximum R obtained is taken as the value corresponding to that subregion.

The angle θ is varied within a user-defined range $\Delta\theta$ around the estimated angle of the pattern θ_0. The phase is varied over the full range $(0, \pi)$. For each θ, the highest value in the ϕ space is kept as the representative quantity of that θ. Figure 4.2(b) shows the maximum R obtained for any ϕ vs θ for the example subregion. It is necessary to discard Pearson data outside the user-defined θ range in order to get the local maximum that corresponds to the actual direction of the neuron. Given a ij subregion, the maximum R_{ij} is the quantity that characterizes its similarity to the reference pattern. In sum,

$$R_{ij} = \max_{\theta \in (\theta_0 - \Delta\theta, \theta_0 + \Delta\theta)} \left[\max_{\phi \in (0,\pi)} R\left(\text{data}, \text{pattern}(\theta, \phi)\right) \right]. \tag{4.2}$$

Both $\Delta\theta$ and the ϕ step $\Delta\phi$ are tuned from GollumDeveloper. For this thesis, $\Delta\theta = 20^{\text{o}}$ and $\Delta\phi = 3^{\text{o}}$ was used.

The executable Gollum is used to analyze all subregions in an image and visualize R of each one overlayed to the original image. The user can then choose a threshold value that discriminates subregions exhibiting a periodic structure from those that do not. This chosen value can be used in the subsequent bulk analysis of a large number of images taken from the sample under identical conditions.

For a first test of the algorithm, an artificial image was assembled using 100 preselected subregions of STORM images of spectrin in hippocampal neurons. 50 subregions were chosen because they clearly exhibited spectrin periodic structures and the other 50 were taken from neurons without periodic structures. The assembled data is shown in Figure 4.4(a) and the result of its analysis, in Figure 4.4(b). Gollum perfectly discriminates subregions with the periodic structure from the rest for a Pearson threshold of 0.2. This test means the automated analysis correctly mimics the human perception that would correspond to a manual analysis.

4.2.2. Bulk analysis

In order to assess how the periodic structure responds to experimental stimuli, it is often necessary to analyze multiple images taken from the same sample in order to gather sufficient statistics. Gollum only requires the user to define a Pearson threshold value to discriminate periodic structures from non periodic ones. Once that threshold is chosen, Gollum works over all selected images and returns an histogram of Pearson values. The previously chosen threshold determines the fraction of subregions that exhibit the periodic structure (PSS fraction). See Section 4.5 for an explanation of the statistical methods used to calculate the Pearson coefficient and the uncertainty of the output values of the bulk analysis.

A typical output of the analysis is the histogram of Figure 4.5. The red dashed line is the chosen threshold for discriminating neuronal material with or without periodic structures. The legend contains the fraction of subregions with

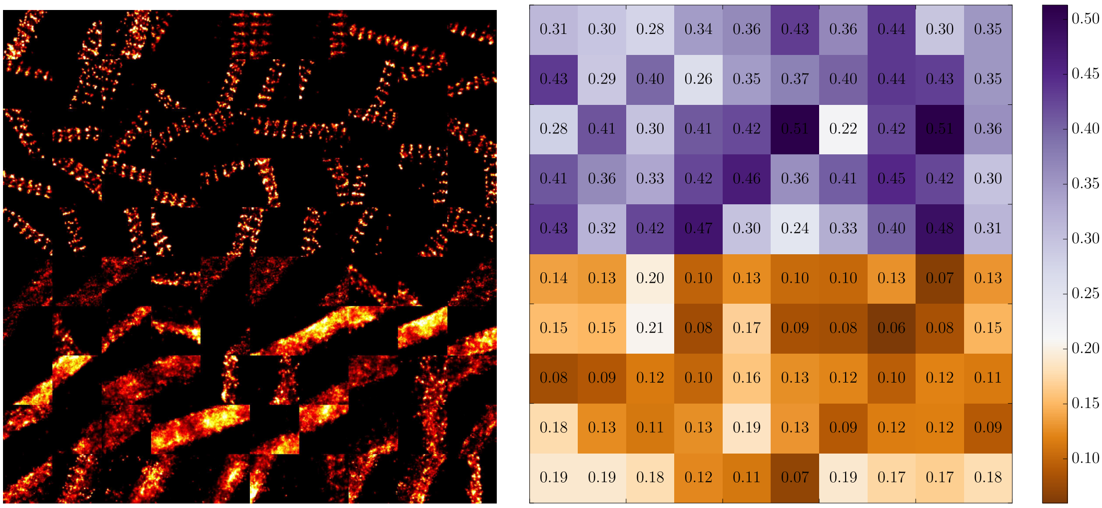

(a) (b)

Figure 4.4: (a) Image assembled from subregions of STORM images of spectrin in hippocampal neurons. (b) Results of the analysis. The white color of the colormap corresponds to the chosen threshold for discriminating subregions with and without the PSS.

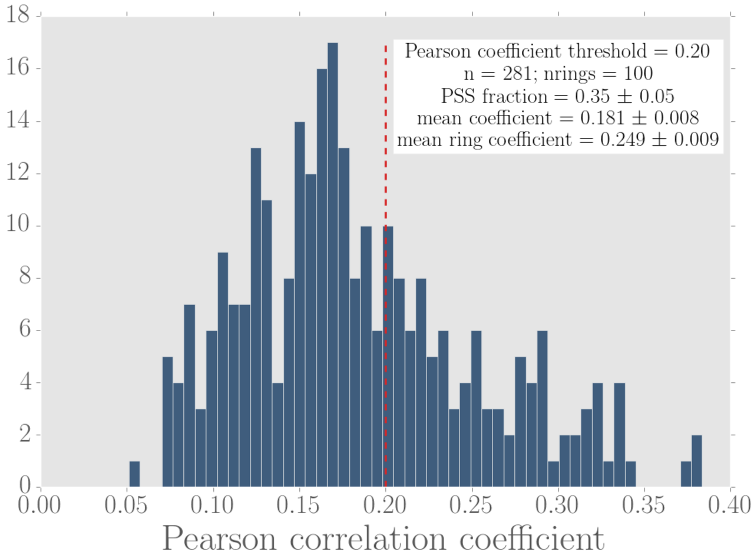

Figure 4.5: Histogram of Pearson coefficient values of a set of subregions. The red dashed line is the chosen threshold for discriminating subregions with the periodic structure.

R above the discrimination value, the mean R of all neuronal subregions and the mean R of the subregions above discrimination. This last quantity can be used for evaluating the quality of the structure, that is its sharpness and contrast. Furthermore, Gollum saves two additional segmented images for each analyzed one: the first has R as the intensity of each pixel and the second is a binary image, indicating whether the subregion has the periodic structure. These output images can be superimposed with the original images.

In order to validate the performance of the analysis, hippocampal neurons fixed at different days *in vitro* (DIV) had their spectrin stained with Alexa Fluor 647. As discussed in [159, 163], an increase in the presence of the periodic structure with the DIV was expected, reaching saturation around 7DIV. 15 STORM images of 10 μm x 10 μm size were taken from each sample, from 2DIV to 40DIV. Each STORM acquisition consisted of 25000 15 ms image frames taken with straight widefield illumination of 642 nm laser intensity of 20 kW cm^{-2}. Some of the final STORM images are shown in Figure 4.6, overlayed with the binary images that indicate the presence of the PSS. A quick inspection of the images reveals that the spectrin stain appears either roughly homogeneous or non-present in early neurons and increasingly packed in the periodic structures after 8DIV. The yellow squares indicating subregions with detected periodic structure successfully confirm the trend.

The whole set of measurements are summarized in Figure 4.7. Here it is revealed that the PSS fraction evolves from 5% at 2DIV to 60% at 14DIV and stays roughly constant at least up to 40DIV. This *plateau* is reached somewhere between 8DIV and 14DIV. This result is important for deciding the suitable age of cells in future studies. If one is interested in assessing how the formation of the periodic structure is affected with a certain stimulus, then such stimulus should be administrated before 14DIV. If, on the other hand, the interest is on how the structure is modified after its consolidation, older cells should be used.

Since picking the Pearson coefficient threshold for periodic structure detection relies on the user, different users may choose different values. Therefore, it is important to test the robustness of the analysis against different thresholds. To this end, the previous analysis was performed for several thresholds. Remarkably, choosing a different threshold value of R changes the absolute quantification of periodic structures but the trend vs DIV remains practically unaffected (see Figure 4.8). This confirms that the bulk analysis of images based on Gollum enables

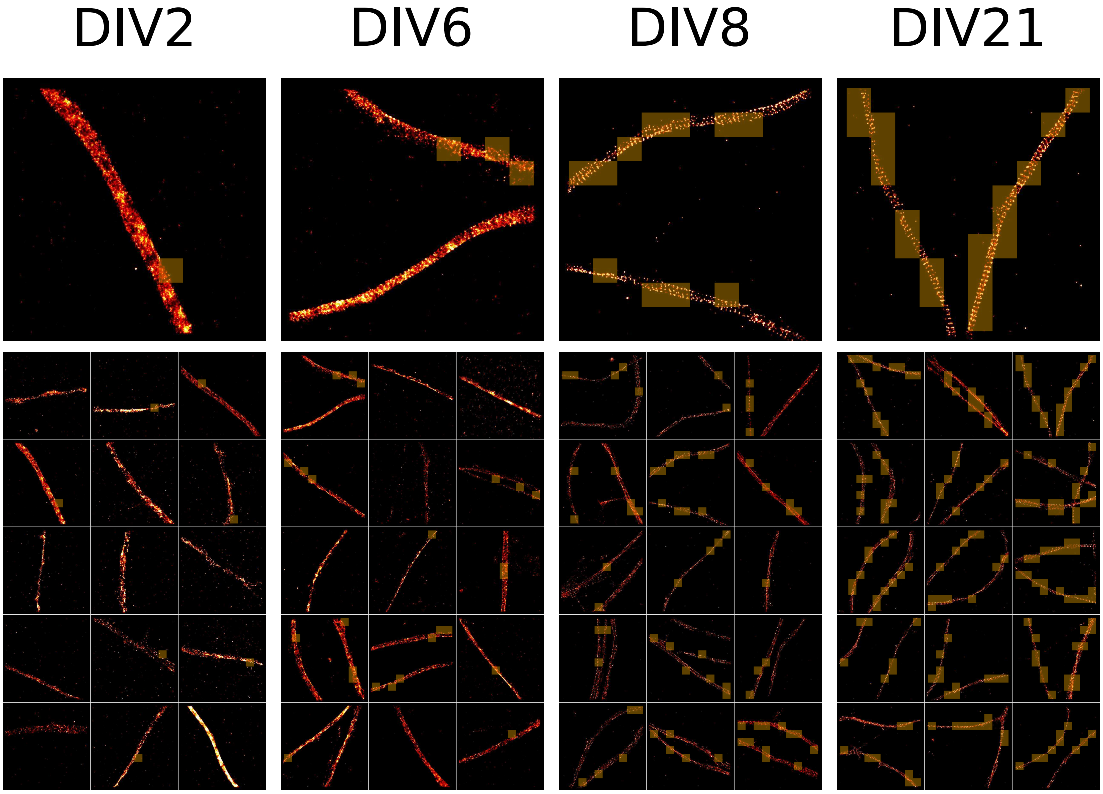

Figure 4.6: Montages of images for different DIV. The upper images are typical single STORM acquisitions. The ones on the bottom are the complete 15 images taken from each sample. The superimposed yellow squares are the subregions where the software detected the PSS.

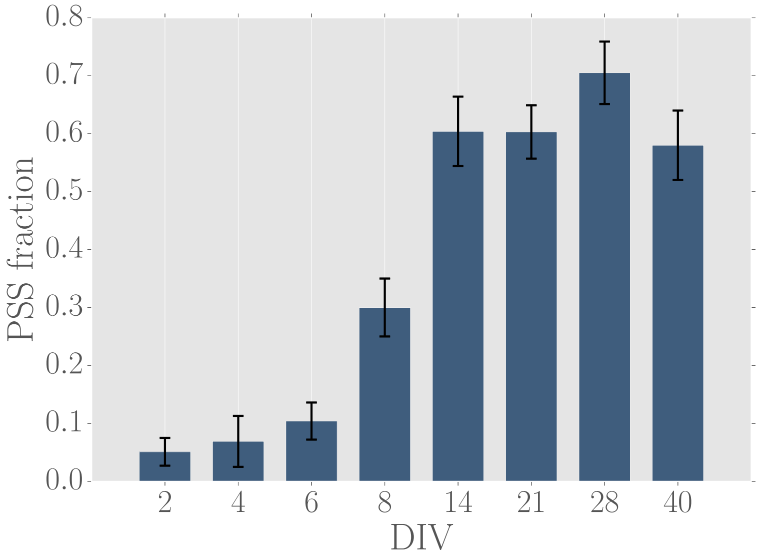

Figure 4.7: PSS fraction vs the days *in vitro* of the hippocampal neurons.

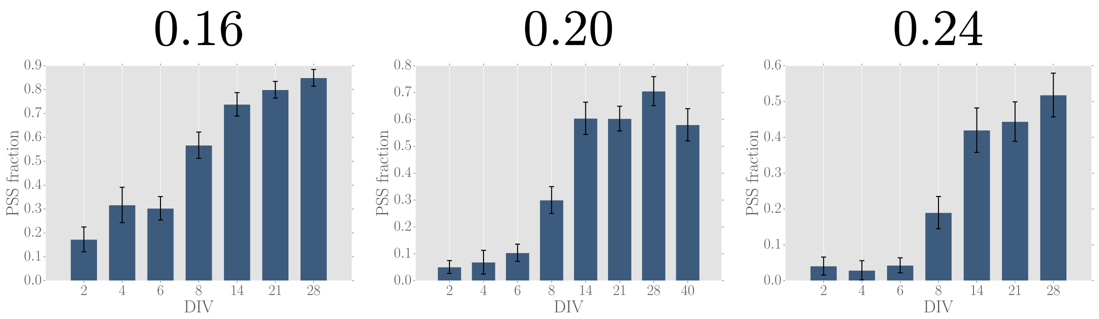

Figure 4.8: PSS fraction vs DIV for different discrimination thresholds. The threshold chosen for the rest of the data analysis was 0.20.

the extraction of solid conclusions, quite free from user influence.

4.3. Application

Gollum is a formidable tool for assessing how the protein periodic structure responds to different stimuli. As a part of an ongoing project in collaboration with the Institute of Biomedicine of Buenos Aires (IBioBA), the effect of a toxic compound on the spectrin periodic structure was analyzed.

Paraquat is a toxic salt herbicide linked to the development of the Parkinson disease[168, 169]. 14DIV cells were treated for 18 hours with concentrations of Paraquat ranging from 1 μM to 25 μM and imaged with the STORM setup at CIBION. Results, shown in Figure 4.9, indicate that the PSS is affected with the drug. A slight decrease of the PSS fraction between 1 μM and 5 μM is followed by a drastic one between 5 μM and 25 μM.

Comparison between the control measurement in Figure 4.9 and the 14DIV value of Figure 4.7 shows that the PSS fraction is not constant across different neuronal cultures. A careful analysis of this variability should be performed between any comparison of results from different cultures can be performed.

4.4. Sample preparation

Sample preparation procedures for all the data presented in this Chapter were carried out at the Institute of Biomedicine of Buenos Aires (IBioBA). When ready, they were taken to CIBION in a multi-well plate so they could be mounted onto a microscope slide with the STORM imaging buffer prepared as described

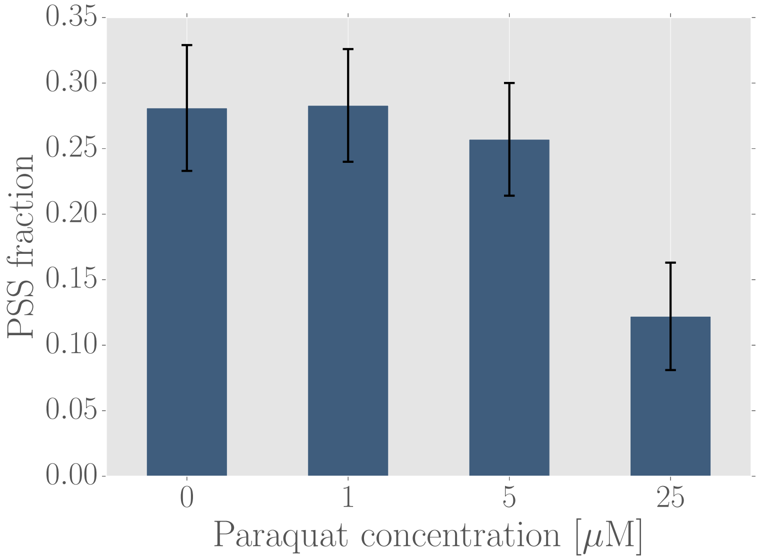

Figure 4.9: PSS fraction vs Paraquat concentration.

in Section A.2.

Primary hippocampal neuronal cultures

Primary hippocampal neurons were prepared as previously described[170, 171]. Briefly, hippocampi from CD1 mouse embryos (E16.5-17.5) were dissected and a neuronal suspension was prepared through Trypsin digestion and mechanical disruption of the tissue. Neurons were plated at a density of 125 cells/mm^2 and maintained in Neurobasal-A medium with 2% B27 and 0.5 mM GlutaMAX-I (Gibco) at 37°C and 5% CO_2.

Immunocytochemistry

Neurons were simultaneously fixed and permeabilized in PHEM buffer (60 mM PIPES, 25 mM HEPES, 5 mM EGTA, 1 mM $MgCl_2$) containing 0.25% glutaraldehyde, 3.7% paraformaldehyde, 3.7% sucrose, and 0.1% Triton X-100, for 20 min at RT. Samples were quenched with 0.1 M glycine in PBS for 15 min and blocked for 1 h in 5% BSA solution in PBS containing 0.01% Triton X-100. Purified Mouse Anti-β-Spectrin II primary antibody (Clone 42/B-Spectrin II, BD Biosciences) was diluted 1:400 in blocking solution and incubated with the samples overnight at 4°C. The secondary antibody (1:750) was conjugated to Alexa Fluor 647 (Life Technologies).

4.5. Statistical methods

4.5.1. Pearson correlation coefficient

The Pearson correlation coefficient R between two array images $a = (a_1, a_2, \dots, a_n)$ and $b = (b_1, b_2, \dots, b_n)$ is calculated as follows:

$$R = \frac{\sum_i (a_i - \bar{a})(b_i - \bar{b})}{\sqrt{\left[\sum_i (a_i - \bar{a})^2\right]\left[\sum_i (b_i - \bar{b})^2\right]}}, \tag{4.3}$$

where $\bar{a}$ and $\bar{b}$ are the mean value of arrays a and b. The Pearson coefficient is equivalent to the correlation between a and b at the origin.

4.5.2. PSS fraction uncertainty

Two sources of uncertainty were identified for the PSS fraction uncertainty σ_{fr}: the spread of values given by biological diversity and the statistical uncertainty.

For the former, σ_{bio}, the standard deviation of the mean value of PSS fraction values of the analyzed images was used. This source of uncertainty addresses the spread of values given by biological diversity.

The number n_0 of counts of a histogram with values greater than a certain threshold follows the binomial distribution $B(n, p)$, where n is the total number of trials and p is the probability of getting a value greater than the threshold. From the binomial distribution, the variance of n_0 is estimated by

$$\mathrm{Var}(n_0) = n_0 \, \frac{n - n_0}{n} \tag{4.4}$$

Therefore, the uncertainty of the PSS fraction $\mathrm{fr} = n_0/n$ is

$$\sigma_{\mathrm{stat}} = \sqrt{\frac{\mathrm{fr}\ (1 - \mathrm{fr})}{n}} \tag{4.5}$$

Finally, the total uncertainty σ_{fr} was calculated as

$$\sigma_{\mathrm{fr}} = \sqrt{\sigma_{\mathrm{bio}}^2 + \sigma_{\mathrm{stat}}^2}. \tag{4.6}$$

4.6. Conclusions

A fundamental computational tool for the future of the quantitative analysis of periodic nanometric structures in neurons was developed. It can retrieve the degree of periodic content of images with minimal user intervention. The software fills the gap needed for large-scale analysis of periodic structures in neurons. Its working principles and detection strategies were detailed. Working tests were shown, including the first systematic measurement of the maturation of the spectrin periodic structure in hippocampal neurons from 2DIV to 40DIV. Finally, the software was applied to the analysis of neuronal samples treated with the Parkinson-related herbicide Paraquat. Results showed a drastic decrease of the fraction of neurons exhibiting the periodic structure for treatments with a concentration beyond 5 μM.

Naturally, the software can be applied to studies of any other regular structure, such as βIV spectrin and ankyrinG, sodium channels and adducin. Furthermore, the exploration of biological cells with fluorescence nanoscopy has only started, providing unprecedented insight into the supramolecular organization of proteins, where more regular and periodic structures are expected.

Estructuras periódicas en el citoesqueleto de neuronas

El avance tecnológico dado por la nanoscopía de fluorescencia para las ciencias biológicas permite estudiar sistemas ya conocidos con un grado de detalle sin precedentes. Un ejemplo es el citoesqueleto de neuronas, donde imágenes con precisión nanoscópica revelaron por primera vez una estructura periódica de actina y espectrina en axones[158], esquematizada en la Figura 4.1. El período de 190 nm hacía imposible su visualización por microscopía de fluorescencia convencional. Estudios subsiguientes revelaron que esta estructura periódica se encuentra en dendritas[159, 160] y en un amplio espectro de tipos de células y distintas especies animales[161, 162]. También se demostró que la estructura se establece progresivamente durante la maduración neuronal alcanzando su forma definitiva alrededor de los 7 días in vitro[163, 159].

Su función todavía no está clara. Se desconoce, por ejemplo, cómo responde la estructura de actina y espectrina a estímulos fisiológicos o patológicos. Para llevar a cabo estudios que respondan estos interrogantes es necesario contar con un método de análisis que permita cuantificar cambios en la estructura periódica.

Aquí se presenta *Gollum*, una herramienta de análisis de imágenes para encontrar y analizar estructuras regulares y arreglos periódicos automáticamente. Para constatar su efectividad, se analizaron imágenes de espectrina en neuronas hipocampales tomadas con el nanoscopio descripto en el Capítulo 3. En primer lugar, se ensambló una imagen compuesta por porciones de imágenes donde se advierte claramente la estructura periódica y porciones de neuritas tomadas por microscopía de fluorescencia convencional. *Gollum* discrimina exitosamente ambos casos. También se compararon imágenes de neuronas fijadas entre 2DIV (2 días *in vitro*) y 40DIV. *Gollum* registra correctamente el incremento esperado en la proporción de anillos conforme a la maduración de las neuronas, llegando a saturar alrededor de los 14DIV. Finalmente, se analizó el efecto del herbicida Paraquat sobre la estructura periódica encontrándose que su proporción disminuye al aumentar la concentración de Paraquat con la que se trató a las neuronas.

Chapter 5

Visualization of protein domains on the membrane of *T. cruzi*

Trypanosoma cruzi (*T. cruzi*) is the hemoflagellate protozoan parasite that in humans causes the Chagas disease. During its life cycle, shown in Figure 5.1, it alternates between a blood-eating *Reduviidae* bug from the subfamily Triatominae commonly known as *vinchuca* and an animal host, usually a mammal. Infection with this blood parasite has been recorded in more than 150 species of 24 families of domestic and wild mammals[172].

A vector vinchuca is infected when feeding from the blood of a previously infected animal. Inside the bug, it goes to the epimastigote stage, capable of reproduction. After reproduction, the epimastigotes move onto the rectal cell wall, where they go to the infectious form, called trypomastigote. When the vinchuca subsequently takes a blood meal from an animal, it also defecates. The trypomastigotes in the feces enter the animal through the bite wound or by crossing mucous membranes. Then, they are capable of swimming into the cells of the host thanks to its flagella, or swimming tail. Other ways of infection include blood transfusions, transplacental transmission, organ transplants and consumption of parasite-infected food[172]. Once inside the host cells, trypomastigotes go to the spherical amastigote stage, from which they can reproduce through binary fission. After reproduction, it goes to the blood trypomastigote form. The accumulation of parasites within the cell eventually produce its destruction and the release of the trypomastigotes into the bloodstream, hence completing the life cycle of the parasite[174].

Chagas disease, also known as American trypanosomiasis, develops in two

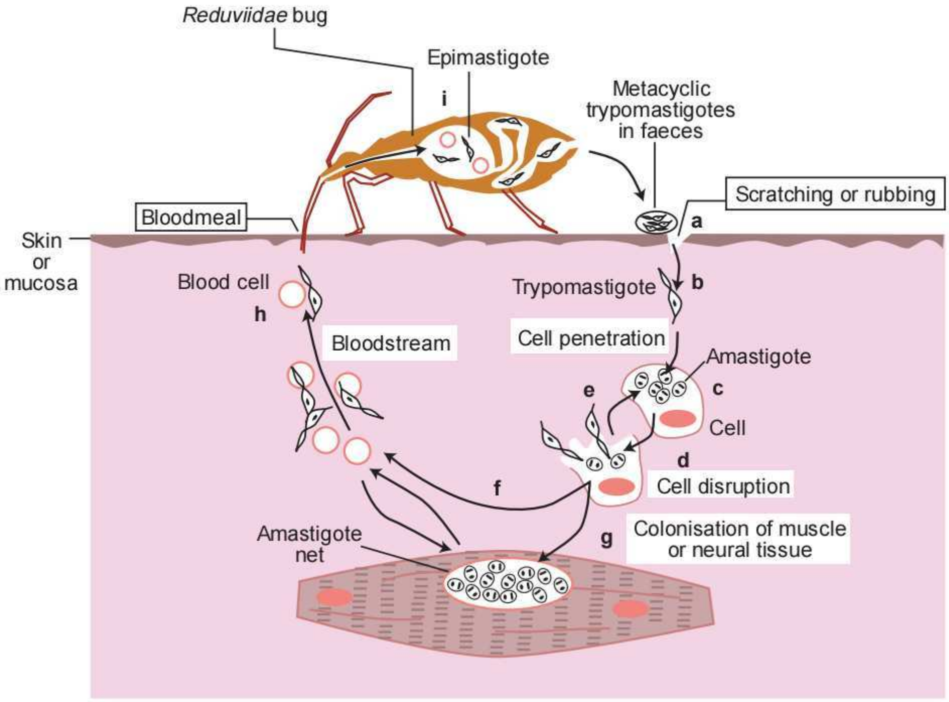

Figure 5.1: *T. cruzi* life cycle. The organism depicted in pink can be human or many other mammals. Image adapted from [173].

stages: the acute and the chronic stage, that can manifest itself decades later[175]. After the initial infection, the incubation period follows, lasting up to four weeks. The acute stage is usually unnoticed beyond some swelling around the entry zone. If untreated, the patient is infected for life. The chronic form affects organs such as the heart, esophagus, colon and the peripheral nervous system. Chagas cardiomyopathy is by far the most serious form of the disease[176]. Affected people may die from sudden death, complex arrhythmias, ventricular aneurysms, heart failure, and thromboembolism[177].

The diagnostic of Chagas is carried out by looking at blood samples through the microscope or by the detection of *T. cruzi* specific antibodies in blood. There is no effective treatment or vaccine. Prevention methods rely on the elimination of vinchucas and a careful analysis of blood transfusion. Chagas disease remains a significant public health issue and a major cause of morbidity and mortality in Latin America, with an estimate of 18 million people infected[178]. Despite nearly 1 century of research, the pathogenesis of chronic Chagas cardiomyopathy is incompletely understood, the most intriguing challenge of which is the complex host-parasite interaction[179]. Therefore, the study of the biology of *T. cruzi* is

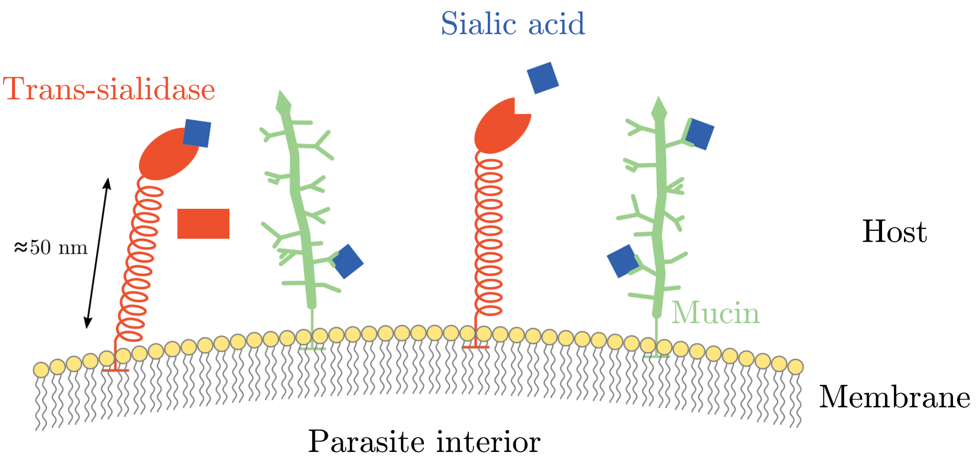

Figure 5.2: Schematic *T. cruzi* membrane components in the nanoscale. Image adapted from [164].

highly relevant to achieve a better understanding of Chagas mechanisms towards new methods of diagnostic and treatment.

5.1. Molecular survival mechanisms of *T. cruzi*

Sialic acid is a monosaccharide found on the outer surface of pathogenic bacteria like *Escherichia coli* and helps them to evade the immune system in their mammalian hosts[180]. Sialic acid compose a negatively charged coat that protects them from killing by human anti-α-galactopyranosyl antibodies[181]. Unlike *E. coli*, *T. cruzi* is unable to synthesize sialic acid so it transfers the monosaccharide from the host to acceptor molecules called mucins in a process called *sialylation*. This enzymatic activity is carried out by an unusual parasite enzyme known as *trans*-sialidase [182, 183]. Mucins are a glycoprotein that besides acting as the sialic acid reservoir, they provide protection against the vector and/or vertebrate-host-derived defense mechanisms and ensure the targeting and invasion of specific cells or tissues[184].

Both *trans*-sialidase enzymes and mucins are located on the surface of the parasite, as depicted in Figure 5.2. *Trans*-sialidases are formed by a catalytic region (responsible for the interaction with sialic acid), then a region displaying repeats of 12 amino acids in tandem, called SAPA (Shed Acute Phase Antigen)[185], and finally a terminal region that covalently binds the structure to the cellular membrane through a glycosylphosphatidylinositol (GPI) anchor[181]. The SAPA domain effectively separates the catalytic domain to about 50 nm away from the cell surface [186]. Mucins are composed of a free amine terminal, a central region with multiple acceptor sites for sialic acid and a terminal region to bind to the membrane with a GPI anchor[181].

The membrane structure and composition makes it possible for the parasite to survive within the bloodstream of the host and invade cells to proliferate. The comprehension of mechanisms involving *trans*-sialidase in the abrogation of immunity against *T. cruzi* infection is crucial for the developing and establishment of effective therapeutic approaches[187]. Due to its biologic relevance in the host/parasite interaction, it is of high interest to fully understand the sialic acid acquisition process together with the distribution of the *trans*-sialidase and acceptor molecules on the *T. cruzi* surface. Due to its size, these structures cannot be resolved with conventional optical microscopy. Here, the localization of the *trans*-sialidase enzyme and mucins are studied in collaboration with the Molecular Immunology Group at the Biotechnological Research Institute (IIB), National University of San Martín (UNSAM).

5.2. Sample preparation

Sample preparation procedures was carried out at the IIB, within secure clean rooms to prevent the proliferation of the infective bug. Fixed samples were taken to CIBION in a multi-well plate. In CIBION they were mounted onto a microscope slide with the STORM imaging buffer prepared as described in Section A.2.

Parasites

T. cruzi parasites from the CL Brener strain in the infective trypomastigote stage are used. Trypomastigotes are obtained from the supernatant of infected Vero culture cells, harvested by centrifugation at 4500 G for 10 min and washed with PBS.

Mucins staining and *in vivo* protein sialylation

Mucin staining is a two-step process. First, the parasites are sialylated and then sialylated proteins are stained through immunofluorescence. Mucins are preferentially detected because they are the main sialic acid acceptor of the *T. cruzi* membrane[188, 186].

Parasites are resuspended up to a concentration of 10^6 per μL in PBS and then incubated with 1 mM Azida sugar for 20-30 min. After washing with 1 mL of PBS, they are incubated with 0.05 nM dibenzocyclooctynes-FLAG (DBCO-FLAG) per 10^6 parasites in PBS 2% SFB for 30-40 min. Finally they are washed with PBS and fixed with 4% paraformaldehyde (PFA) in PBS for 30 min and stored at 4°C until its use.

This treatment enables the detection of sialylated proteins (sialylated with the modified saccharide) through α-Flag antibodies.

Parasites adsorption to coverslips and immunostaining

18 mm 1.5# coverslips are treated with a 1/5 poly-lysine dilution (Sigma) for 20-30 min.

Parasites are resuspended up to a concentration of $4-5\ 10^6$ per 200 μL in PBS and adsorbed through incubation of those 200 μL of suspended trypomastigotes over the previously-treated coverslips for 1 h.

Once adsorbed, they are washed with PBS once and incubated with blocking solution (2% BSA in PBS) for 1 h. Then, they are incubated for 1 h with a serum dilution α-protein-of-interest (α-Flag 1:2000 made in rat for the detection of sialylated proteins and α-SAPA 1:10000 made in rabbit). Coverslips are washed three times in PBS and incubated for 1 h with the secondary antibodies α-dye (1:2000 α-rat conjugated with Alexa Fluor 568 and 1:1000 α-rabbit conjugated with Alexa Fluor 647). Sample is washed three times with PBS and fixed with 4% PFA in PBS for 15 min. Then washed with PBS and stored in 0.1% azida in PBS at 4°C and guarded from light.

5.3. Visualizing the surface distribution of *trans*-sialidase and mucin

The SAPA region of the *trans*-sialidase was stained with Alexa Fluor 647 and mucins with Alexa Fluor 568. The nanoscope was set up in the dual-color 2D configuration. The channel overlay calibration and the acquisition were performed according to the guidelines detailed in Section 3.4.3.

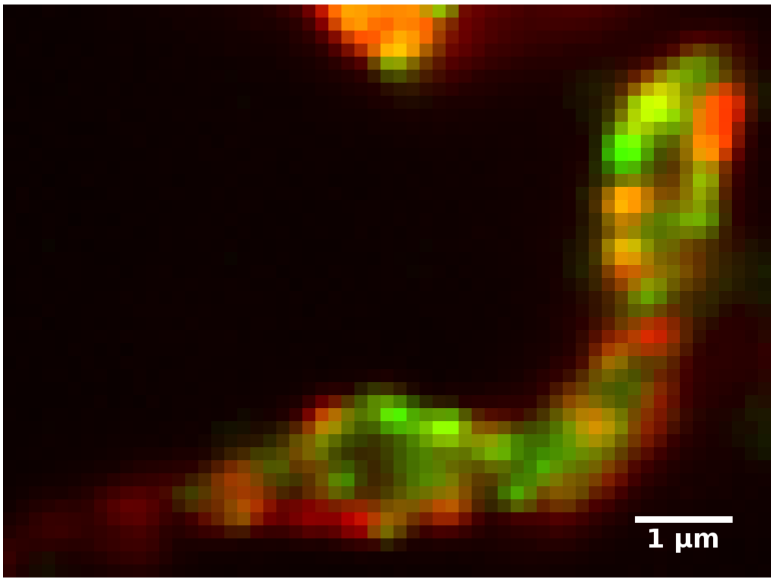

(a)

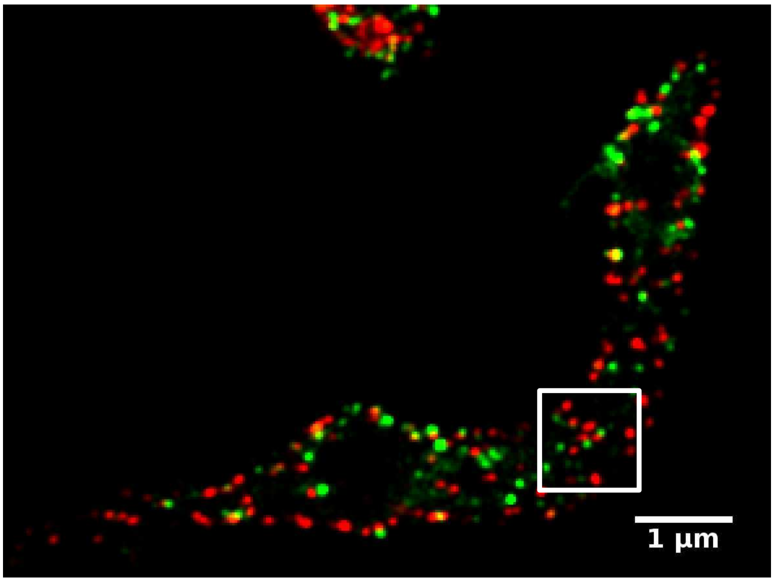

(b)

Figure 5.3: (a) Widefield and (b) STORM image of *trans*-sialidases (in red) and mucins (in green) of a *T. cruzi*.

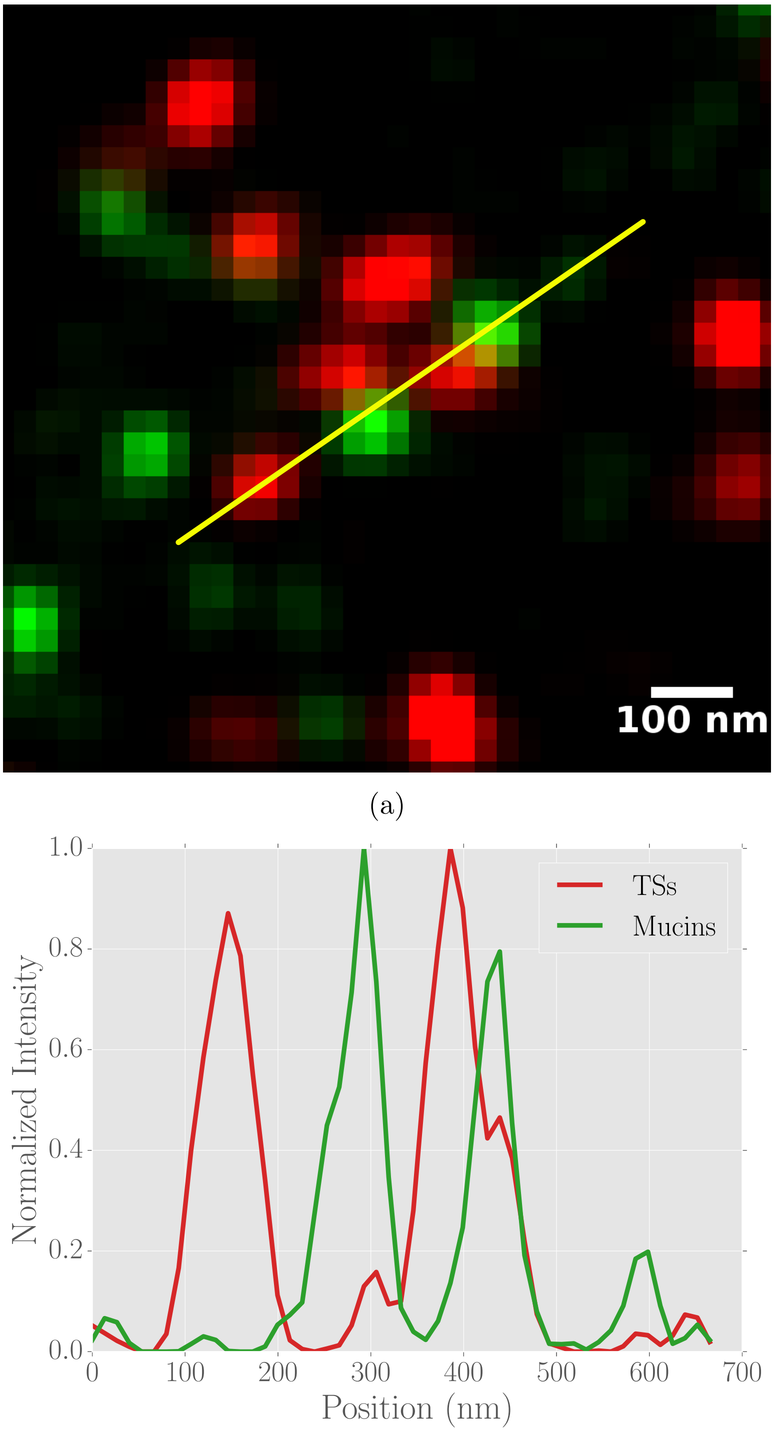

(a)

(b)

Figure 5.4: (a) Area in the white square of Figure 5.3. (b) Intensity profile along the line in (a) for both channels.

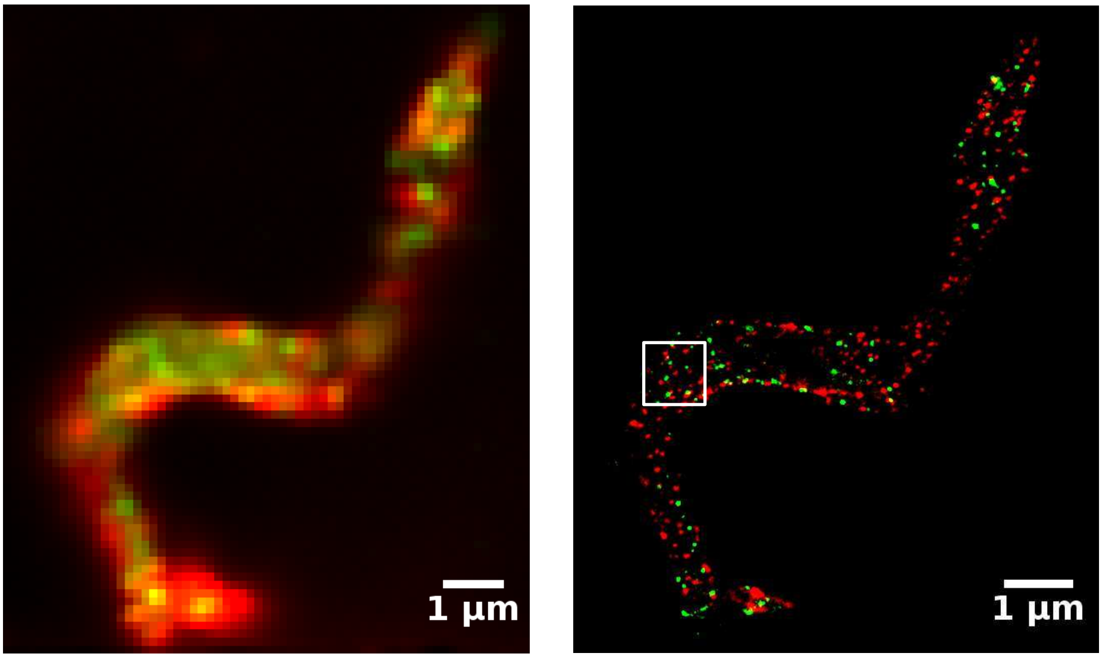

(a) (b)

Figure 5.5: (a) Widefield and (b) STORM image of *trans*-sialidases (in red) and mucins (in green) of a *T. cruzi*.

Since the parasites are roughly 1 μm thick, the illumination was configured in straight widefield mode. The 532 nm laser intensity was 12 kW cm^{-2} and the 642 nm laser was 6 kW cm^{-2}. Each acquisition took 20000 frames at 40 ms of exposure time.

The crosstalk between channels was evaluated by imaging samples stained only by one of the dyes. In both cases no crosstalk was observed.

The background fluorescence was corrected with a running median filter prior to the localization analysis, as described in [112].

Comparison between widefield and STORM typical results are shown in Figures 5.3 and 5.5. The widefield images were built by averaging the all the frames of the acquisition. From widefield images one can only assess that the distribution of the proteins under study is not homogeneous throughout the surface of the parasite. Any detail about the spatial distribution of the *trans*-sialidase and mucin is blurred by the diffraction limited resolution. STORM, on the other hand, delivers images where it is clear that mucins and *trans*-sialidases are organized in isolated domains, and it is even possible to quantify their size, separation and degree of overlap. Zoomed images from the squares of Figures 5.3 and 5.5 are shown in

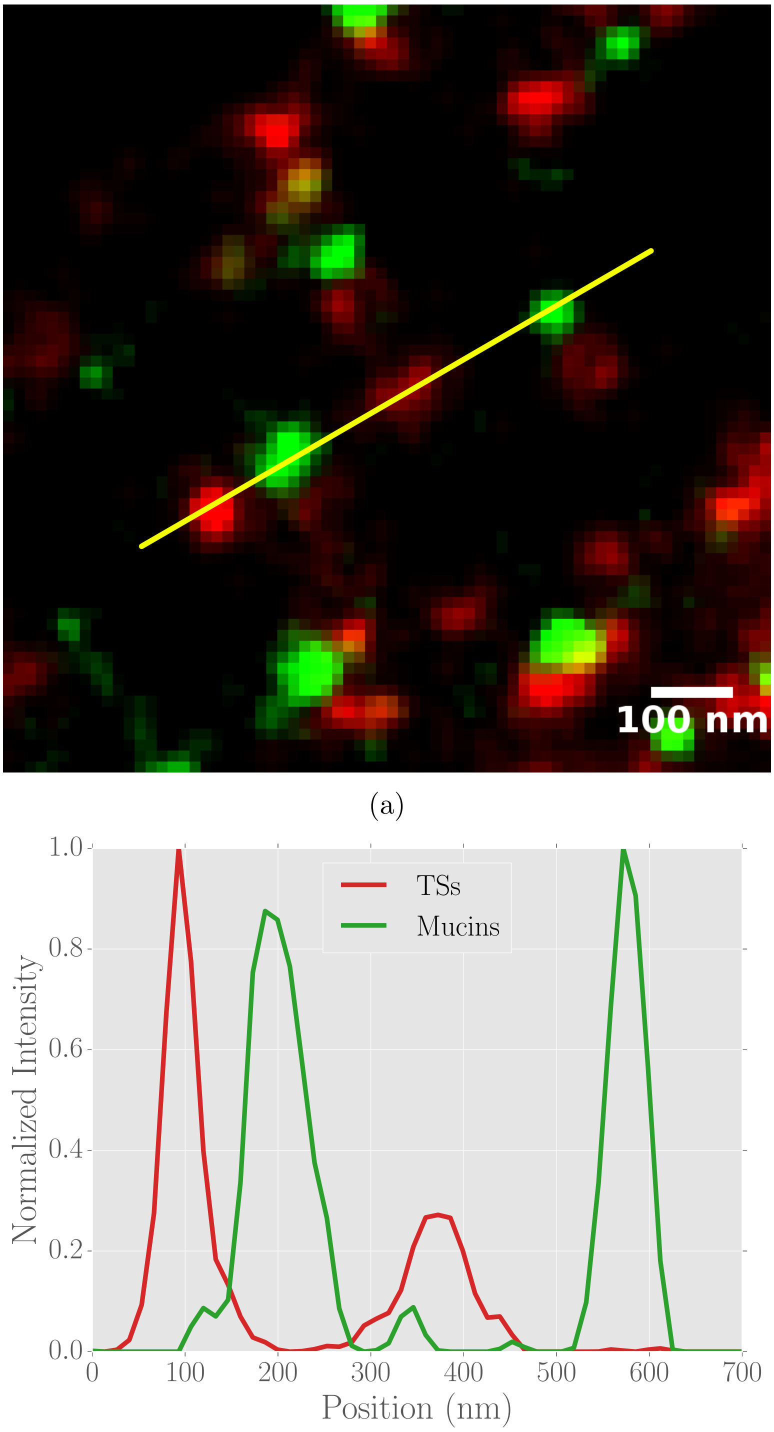

(a)

(b)

Figure 5.6: (a) Area in the white square of Figure 5.5. (b) Intensity profile along the line in (a) for both channels.

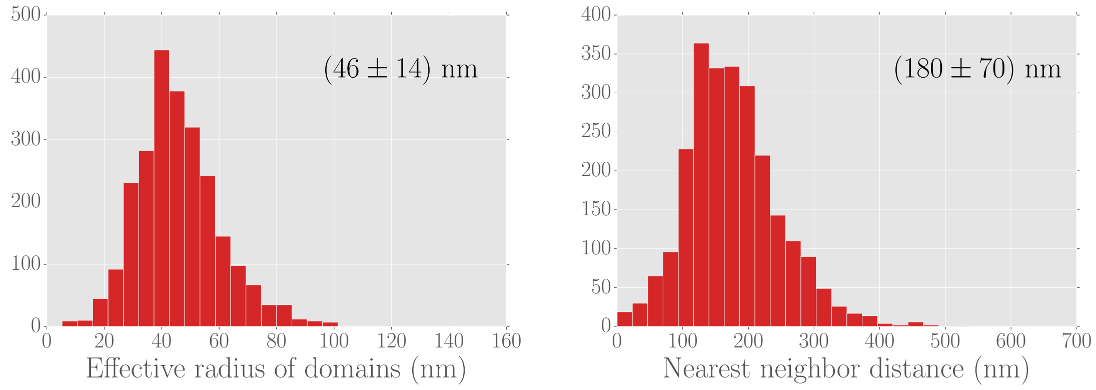

(a) (b)

Figure 5.7: Effective radius (a) and nearest neighbor distance (b) distributions for *trans*-sialidase domains. The corresponding mean value and standard deviation estimates are shown.

Figures 5.4 and 5.6, respectively. The intensity profiles show that it is possible to extract precise dual-color information from areas an order of magnitude smaller than the diffraction limited resolution.

A total of 24 whole *T. cruzi* parasites were imaged, comprising 2461 *trans*-sialidase domains and 1227 mucin domains.

A special routine was developed to automatically analyze the spatial distribution of the domains. The user manually indicates a broad region around each domain and the software automatically outlines the precise area of such domain. This is done by measuring the median of the user-enclosed region and considering as part of the domain those pixels with intensity greater than the median plus a 20% of the intensity standard deviation. This threshold value was found effective to discern the protein domains from the background of the images. This local strategy makes the determination insensitive to the naturally stochastic number of single-molecule localizations conforming each domain. Then, the software quantifies the size and nearest neighbor distance of each protein domain, along with the overlap ratio between channels. Histograms of each quantity are built once all images have been analyzed.

The effective radius, i.e. the radius of a circle with the same area, was chosen as a measure of the size of the domain. The resulting histograms for *trans*-sialidase and mucin domains are shown in Figures 5.7(a) and 5.8(a), respectively. On each histogram, its mean value and standard deviation estimates are indicated. Both radius histograms have mean values well below the diffraction-limited

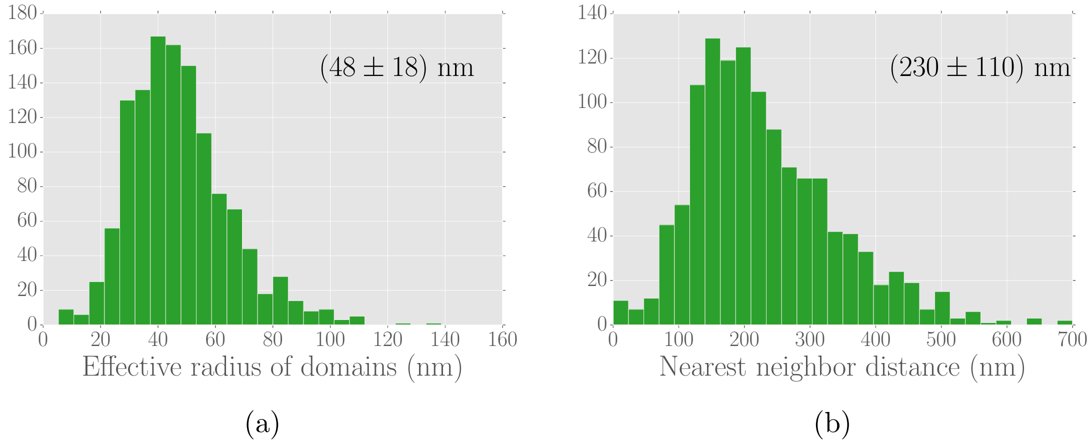

(a) (b)

Figure 5.8: Effective radius (a) and nearest neighbor distance (b) distributions for mucin domains. The corresponding mean value and standard deviation estimates are shown.

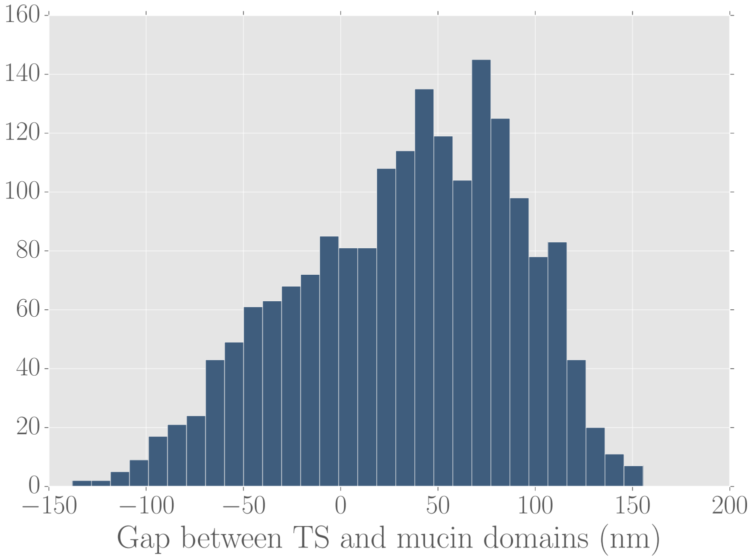

Figure 5.9: Distribution of the gap between *trans*-sialidases and mucins domains. A negative value indicates overlapping domains.

resolution. Also, since no sharp cutoff is observed at their lower end, the reported size of domains does not seem to be limited by the resolution of the nanoscopic images.

The nearest neighbor distance between the domains of each protein was measured between the centroid coordinates. This parameter is related to the coverage of the membrane and is relevant to model the survival mechanism of the parasite. The resulting histograms for *trans*-sialidase and mucin domains are shown in Figures 5.7(b) and 5.8(b), respectively. On each histogram, its mean value and standard deviation estimates are indicated. Both mean values are roughly equal to the resolution limit of conventional fluorescence microscopes, thus the apparent overlapping of domains in widefield images.

Colocalization between *trans*-sialidases and mucins was analyzed in two ways: by calculating the gap between nearby domains and the colocalization ratio. Figure 5.9 shows the distribution of the gap between the proteins, calculated as the distance between the nearest mucin to a *trans*-sialidase domain, minus the sum of their effective radii. Thus, a negative gap value corresponds to the overlap of domains. This histogram has a mean value of 30 nm. The colocalization ratio was calculated as the area (in pixels) shared by both proteins over the total area occupied by each one. The ratio gives a 7% for *trans*-sialidases and a 12% for mucins. These results are a strong indication that that *trans*-sialidases and mucins do not need to overlap in order to perform their biological function. If this were the case, the sialylation of mucins would have to follow a different mechanism than action by contact.

The results presented here should be further confirmed through a new analysis routine requiring less user intervention. Such routine would eliminate any bias that the current manual domain identification could be creating.

5.4. Conclusions

Trans-sialidase and mucin isolated domains on the *T. cruzi* membrane were observed with an unprecedented spatial resolution thanks to localization fluorescence nanoscopy. The very existence of domains is interesting: since *trans*-sialidases and mucins alike are bound to the membrane through a GPI anchor, there has to be an additional specific interaction that groups them in domains of each protein. The nearest neighbor distance between the domains of each protein was also analyzed. This parameter is related to the coverage of the membrane and is relevant to model the survival mechanism of the parasite.

The relative distance and overlap between *trans*-sialidases and mucins was quantified. It was expected that *trans*-sialidases would be located close enough to mucins so as to allow the mucin sialylation to proceed. Notably, there was no colocalization between *trans*-sialidase and mucin domains. Taking into account that *trans*-sialidase and mucins are not only enzyme and substrate but also GPI-anchored proteins, their segregated distribution at the parasite surface is certainly puzzling. This result is a clear evidence of the *T. cruzi* complex infection mechanisms.

This study challenge the classic paradigm in which membrane-anchored mucins are sialylated by a nearby *trans*-sialidase enzyme. The results could not have been produced with conventional fluorescence techniques because the dimensions of the proteins domains and their separation are smaller than the light diffraction limit of resolution.

A hypothesis consistent with our results is that mucins could be sialylated through secreted *trans*-sialidases, present in the extracelullar space. To put this idea to test, our collaborators at IIB carried out the following experiment: fixed parasites were mixed with alive ones. Since fixed *T. cruzi* are sialic acid acceptors but cannot produce *trans*-sialidases, any sialic acid they intake could only be transferred by *trans*-sialidases secreted by the alive parasites. Sialic acid was in fact observed at mucins on the fixed parasites[186], which is a strong evidence in favor of the hypothesis.

A follow-up of this study could be to answer whether the domains are randomly distributed on the membrane. This matter could be addressed by analyzing the correlation between size and position of domains and with a comparison between its experimental spatial distribution and a simulated one that takes the observed size as input.

Visualización de dominios de proteínas en la membrana del *T. cruzi*

El *Trypanosoma cruzi* (*T. cruzi*) es el parásito que en humanos causa la enfermedad de Chagas. Durante su ciclo de vida (Figura 5.1) invade el insecto conocido como vinchuca y un mamífero, que puede ser el humano. La enfermedad del Chagas se desarrolla en dos etapas: la aguda, luego de la infección original y la crónica, que puede desarrollarse décadas más tarde y generalmente conlleva cardiopatías que pueden llevar a la muerte. Chagas es un grave problema de enfermedad pública en Latinoamérica, donde hay unos 18 millones de infectados[178].

El ácido siálico es un monosacárido que algunas bacterias usan para evadir al sistema inmune del huésped[180, 181]. *T. cruzi* no produce ácido siálico, por lo que lo transfiere del huésped a moléculas aceptoras llamadas mucinas dispuestas en su membrana por medio de la enzima *trans*-sialidasa[182, 183] (ver Figura 5.2). La comprensión de los mecanismos involucrados en el reclutamiento de ácido siálico por parte de la *trans*-sialidasa es crucial para el desarrollo de nuevas estrategias terapéuticas[187]. Es de especial interés el estudio de la distribución espacial de las *trans*-sialidasas y las mucinas. Sin embargo, su tamaño no puede ser resuelto por microscopía de fluorescencia tradicional, por lo que es necesario recurrir a la nanoscopía de fluorescencia, proyecto que se llevó a cabo en colaboración con el Grupo de Inmunología Molecular del Instituto de Investigación Biotecnológico (IIB) de la Universidad Nacional de San Martín (UNSAM).

La preparación de muestras se llevó a cabo en IIB y la toma de imágenes, en CIBION. La región SAPA de la *trans*-sialidasa se marcó con Alexa Fluor 647 y las mucinas, con Alexa Fluor 568. El nanoscopio se configuró en la modalidad de dos colores y se tomaron 10 imágenes, que incluyeron a 31 parásitos en total y comprendieron 2461 de dominios de *trans*-sialidasas y 1227 de dominios de mucinas (ver resultados típicos en las Figuras 5.3 y 5.5). Las imágenes de superresolución permitieron cuantificar el tamaño, separación y grado de superposición de los dominios. A diferencia de lo esperado, se encontró que las dos proteínas no se superponen, lo que evidencia la complejidad de los mecanismos de supervivencia del *T. cruzi*. Se formula la hipótesis de que las mucinas podrían almacenar ácido siálico transferido por *trans*-sialidasas presentes en el medio extracelular.

Chapter 6

Conclusions and perspectives

Fluorescence nanoscopy is a recently emerged field that is still experimenting new groundbreaking concepts on a regular basis. In this thesis, the group of techniques known as single-molecule localization fluorescence nanoscopy was studied. Then, a multicolor fluorescence nanoscope was designed and built capable of super-resolved imaging in three dimensiones, and applied and applied to projects of biological significance in which the resolution of conventional fluorescence microscopy was not enough to resolve the structures of interest.

In Chapter 3, the features and performance of the fluorescence localization nanoscope were described. It is capable of acquiring 2D single-color, 3D single-color and dual-color images with nanometric resolution. It is equipped with a focus stabilization system that can lock the focus of the nanoscope within a 40 nm range for an unlimited amount of time. The specially developed open-source control software *Tormenta* was described in detail too. Particular operating instructions for each mode of imaging were provided and typical images were presented with a lateral resolution of 40 nm. In the future, the system could be further improved with an online analysis system in order to produce the nanoscopic images during acquisition. It could be powered by a field programmable gate array (FPGA) or a dedicated graphics processing unit (GPU).

The superior resolution provided by fluorescence nanoscopy led to discoveries in the biological sciences. One such example is the neuronal periodic cytoskeleton, first observed in 2012. In Chapter 4, the problem of automatically and quantitatively assessing changes in the presence of this structure due to different stimuli was addressed. An open-source software termed *Gollum* was developed to analyze the images and quantify the abundance of such periodic structures, with minimal user intervention. Its work principles were explained. Its effectivity was demonstrated with test images and also by the analysis of images of spectrin in hippocampal neurons from 2DIV to 40DIV. This analysis showed great agreement with the qualitative assessments found in the literature that stated that the periodic spectrin structure is progressively formed during cell maturation and are consolidated around 7DIV. Finally, as a part of an ongoing project in collaboration with the Institute of Biomedicine of Buenos Aires (IBioBA), the software was used to quantify how the herbicide Paraquat affects the periodical spectrin structure. It was shown that a concentration beyond 5 μM causes a significant decrease in the fraction of neuronal mass exhibiting the periodic spectrin structure. This software enables the quantification of regular structures of any kind. Its development is timely and its application should be wide and popular. Super-resolution microscopy provides insight into the supramolecular organization of proteins in biological cells and tissue, where regular and periodic structures of different kind are expected.

Chagas disease is a significant public health issue and a major cause of morbidity and mortality in Latin America. It is caused by a protozoan parasite called *T. cruzi*. In collaboration with the Molecular Immunology Group at the Biotechnological Research Institute (IIB), National University of San Martín (UNSAM), the spatial distribution of two proteins on the membrane of the parasite was studied in Chapter 5. These proteins are the *trans*-sialidase and mucin and together they extract and store sialic acid from the host. They are key for the parasite survival because it uses the sialic acid to escape the host immunological system. Localization fluorescence nanoscopy was used to image both proteins simultaneously. It was shown that they are distributed in nanometric domains and its size, distance and degree of overlap was quantified. It was expected that *trans*-sialidases would be located close enough to mucins so as to allow the mucin sialylation to proceed. Notably, there was very little colocalization between *trans*-sialidase and mucin domains. This result is a clear evidence of the *T. cruzi* complex infection mechanisms. A hypothesis consistent with such results is that mucins could be sialylated through secreted *trans*-sialidases, present in the extracellular space.

Fluorescence nanoscopy is the natural successor of the hugely successful fluorescence microscopy. It constitutes a key tool in the future of biological imaging for a simple reason, one can see more. This thesis is one more step towards its robust application in the life sciences, and obtaining quantitative information out of super-resolved images.

Conclusiones

La nanoscopía de fluorescencia, como todo campo de origen reciente, todavía se encuentra en un estado de constante innovación. En esta tesis, se estudió el grupo de técnicas conocidas como nanoescopía de fluorescencia por localización de moléculas individuales. Se diseñó y construyó un nanoscopio multicolor de fluorescencia capaz de obtener imágenes de superresolución en tres dimensiones, y se lo aplicó a proyectos de importancia biológica en el que la resolución de la microscopía de fluorescencia convencional no es suficiente para resolver las estructuras de interés.

En el Capítulo 3, se describieron las características y el rendimiento del nanoscopio de fluorescencia por localización. Es capaz de adquirir imágenes con resolución nanométrica 2D y 3D a un color y bicolores. Está equipado con un sistema de estabilización que puede mantener el foco del nanoscopio dentro de un rango de 40 nm por tiempo ilimitado. Se describió en detalle *Tormenta*, el software de control de código abierto especialmente desarrollado. Se proporcionaron instrucciones de funcionamiento particulares para cada modo de adquisición de imágenes y se presentaron imágenes típicas con una resolución lateral de 40 nm. En el futuro, el sistema podría mejorarse con un sistema de análisis en línea con el fin de producir las imágenes nanoscópicas durante la adquisición. Podría ser alimentado por una matriz de campo programable (FPGA) o una unidad de procesamiento gráfico dedicada (GPU).

La resolución superior proporcionada por la nanoscopía de fluorescencia condujo a descubrimientos en las ciencias biológicas. Uno de estos ejemplos es el citoesqueleto periódico neuronal, observado por primera vez en 2012. En el Capítulo 4, se abordó el problema de evaluar automáticamente y cuantitativamente los cambios en la presencia de esta estructura debido a diferentes estímulos. Se desarrolló un software de código abierto denominado *Gollum* para analizar las imágenes y cuantificar la abundancia de dichas estructuras periódicas, con una mínima intervención del usuario. Se explicaron sus principios de funcionamiento. Su efectividad se demostró con imágenes de prueba y también por el análisis de imágenes de espectrina en neuronas del hipocampo de 2DIV a 40DIV. Este análisis mostró gran concordancia con las evaluaciones cualitativas encontradas en la literatura que afirmaron que la estructura periódica de espectrina se forma progresivamente durante la maduración celular y se consolida alrededor de los 7DIV. Finalmente, como parte de un proyecto en curso en colaboración con el Instituto de Biomedicina de Buenos Aires (IBioBA), se utilizó el software para cuantificar la forma en que el herbicida Paraquat afecta a la estructura periódica de espectrina. Se demostró que una concentración mayor a 5 μM causa una disminución significativa en la fracción de masa neuronal que exhibe la estructura periódica de espectrina. Este software permite la cuantificación de estructuras regulares de cualquier tipo. Su desarrollo es oportuno y su aplicación debe ser amplia y popular. La microscopía de superresolución brinda información sobre la organización supramolecular de proteínas en células y tejidos biológicos, donde se espera encontrar estructuras regulares y periódicas de diferente tipo.

La enfermedad de Chagas es un problema importante de salud pública y una de las principales causas de mortalidad en América Latina. Es causada por un parásito protozoario llamado *T. cruzi*. En colaboración con el Grupo de Inmunología Molecular del Instituto de Investigaciones Biotecnológicas (IIB) de la Universidad Nacional de San Martín (UNSAM), se estudió la distribución espacial de dos proteínas en la membrana del parásito. Estas proteínas son la *trans*-sialidasa y la mucina y juntos extraen y almacenan el ácido siálico del huésped. Son clave para la supervivencia del parásito, ya que utiliza el ácido siálico para escapar del sistema inmunológico del huésped. Se utilizó nanoescopía de fluorescencia de localización para visualizar simultáneamente ambas proteínas. Se demostró que se distribuyen en dominios nanométricos y se cuantificó su tamaño, distancia y grado de superposición. Se esperaba que las *trans*-sialidasas estuvieran situadas suficientemente cerca de las mucinas como para permitir que la sialización de mucina se efectuara por contacto. Sin embargo, se encontró poca colocalización entre los dominios de *trans*-sialidasa y los de mucina. Este resultado es una clara evidencia de los mecanismos complejos de infección del parásito. Una hipótesis consistente con tales resultados es que las mucinas podrían ser sializadas a través de *trans*-sialidasas secretadas, presentes en el espacio extracelular.

La nanoscopía de fluorescencia es el sucesor natural de la microscopía de fluorescencia. Constituye una herramienta clave en el futuro de la toma de imágenes biológicas por una simple razón: se puede ver más. Esta tesis es un paso más hacia su aplicación en las ciencias de la vida y la obtención de información cuantitativa a partir de imágenes de superresolución.

Appendix A

Protocols

A.1. Calibration samples preparation

A.1.1. Flow chamber

Several bidimensional samples were prepared through the flow chamber technique. It is a straightforward way of easily apply and exchange solutions along a coverslip. Here we describe how to build it and two protocols for making calibration samples with it.

How to build the flow chamber

1. Sonicate a microscope slide and a 22 mm squared coverslip in mQ water three times for 10 min each, then dry with N_2.

2. Cover the long edges of the microscope slide with double-sided tape leaving an uncover corridor along the middle of the slide.

3. Stick the coverslip over the tape on the middle of the slide, as pictured in Figure A.1. Press onto the coverslip with a pipette tip so it makes full contact with the double-side tape. A chamber of 20-30 μL is thus created between the coverslip and the microscope slide.

4. Take off the excess double-sided tape.

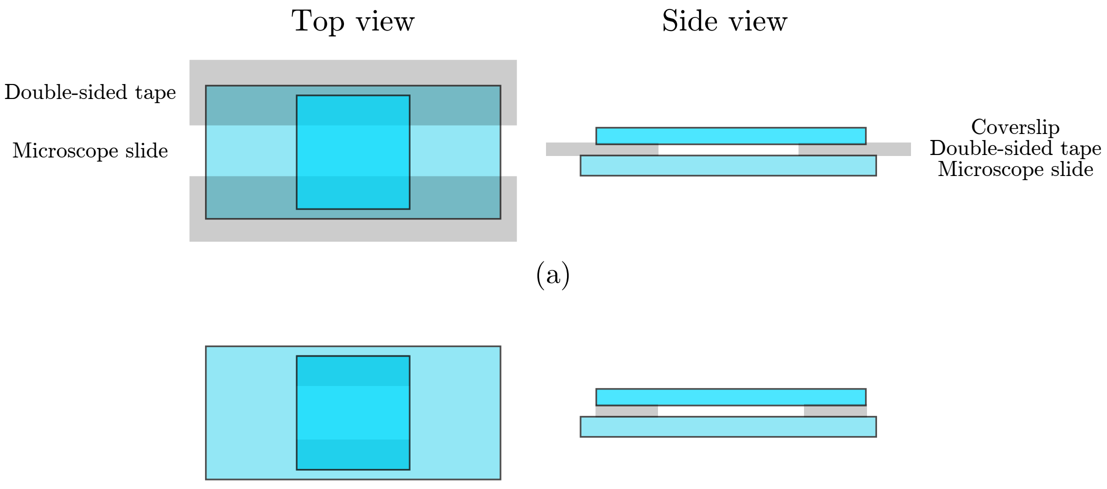

(a)

(b)

Figure A.1: Flow chamber diagram. (a) preparation, (b) done.

A.1.2. 2D Stained neutravidin sample

This protocol is designed to make bidimensional samples of neutravidin conjugated with a fluorophore. By tuning the stained neutravidin concentration, one can change the spatial final concentration from nearly-homogeneous samples to single-molecule.

Protocol

1. Make the flow chamber
2. Flow 30 μL BSA through the channel
3. Flow 100 μL TRIS through the channel
4. Dilute the stained neutravidin to the desired concentration vortexing after each dilution. 1:10000 gives single-molecule concentration.
5. Flow 100 μL of the diluted neutravidin through the channel
6. Flow 200 μL TRIS through the channel
7. Flow 200 μL IB + 2 μL GLOX (+ 2 μL MEA or βME if blinking is desired) (see Appendix A.2)
8. Seal

A.1.3. 2D bead sample

Two different protocols were used during the thesis. By tuning the bead concentration in PBS, one can change the spatial final concentration from nearly-homogeneous samples to single-molecule.

Protocol 1 (simpler)[189]

1. Sonicate bead eppendorf to break clusters
2. Dilute 1 μL of beads into 200 μL PBS and mix.
3. Make the flow chamber
4. Flow 30 μL of the diluted beads into the channel
5. Wait for 15 min*
6. Wash with 200 μL PBS.
7. Seal

Note *: the dilution and incubation time can be adjusted to obtain different densities of beads. This protocol typically results in between 3-10 beads per 20.5 μm x 20.5 μm field-of-view.

Protocol 2 (complex)

1. Sonicate bead eppendorf to break clusters
2. Dilute beads in TRIS (1:1000 for a dense sample)
3. Make the flow chamber
4. Flow 30 μL of the diluted beads into the channel
5. Make 50 μL of solution containing:
    - TRIS 10 mM o 50 mM pH 7.5
    - NaCl 10 mM o 50 mM
    - $MgCl_2$ 50 mM
6. Flow solution through the channel

7. Wash with 200 μL PBS.
8. Seal

A.2. STORM imaging buffer

The aqueous imaging buffer used as mounting media has two main components: the thiol that enables photoswitching and an oxygen scavenging system to reduce photobleaching. Along this thesis work, two thiols were used: mercaptoethylamine and β-mercaptoethanol. For the oxygen scavenging system, a solution containing glucose oxidase and catalase enzymes was used.

Here, the protocols for each solution are described. The final imaging buffer (IB) must be prepared immediately before the imaging session. IB is used directly as prepared while MEA or βME and GLOX are used 1:100. If a hollow microscope slide is used, 100 μL of buffer is enough to fill the slide.

- 98 μL IB
- 1 μL MEA or βME
- 1 μL GLOX

Vortex just before pipetting onto the microscope slide. Place the coverslip with the sample facing down, remove the excess volume (with vacuum for example) and seal.

Imaging buffer (IB)

Components

- 50 mM TRIS pH 8
- 10 mM NaCl
- 10% m/v glucose pH 8

Protocol

1. Find 50 mL falcon tube
2. Add 242 mg TRIS, 23.376 mg NaCl and 4 g glucose
3. Add ∼30 mL mQ water
4. Take to pH 8
5. Take to 40 mL with mQ water
6. Aliquot in 2.5 mL eppendorf tubes and store at -20°C

The working aliquot should be stored at 4°C. It lasts for ∼3 months.

MEA 100x stock solution

1. 77 mg mercaptoethylamine (Sigma-Aldrich 30070) in 1 mL H_20
2. Vortex
3. Take to pH 7.5-8.5 (done with 40 μL HCl 1:12 + 10 μL pure HCl)
4. Seal with parafilm

It lasts for months stored at 4°C.

βME 100x stock solution

β-mercaptoethanol (Sigma-Aldrich M6250) is already the 100x stock solution. Use a 2.5 mL eppendorf tube as a working aliquot. Seal with parafilm each time.

GLOX 100x stock solution

1. Dissolve 10-15 mg glucose oxidase (Sigma-Aldrich G2133) in 170 μL of 10 mM TRIS pH 7.5, 50 mM NaCl in a a 500 μL eppendorf
2. Add 80 μL catalase (Sigma-Aldrich C100) after vortexing
3. Centrifuge at 13g for 60 s

Use only the supernatant, leaving catalase crystals at the bottom. It lasts for months stored at 4°C.

Bibliography

[1] D. Brewster, "On an account of a rock-crystal lens and decomposed glass found in niniveh," *Die Fortschritte der Physik im Jahre*, pp. 355–356, 1852.

[2] R. Rashed, "A pioneer in anaclastics: Ibn sahl on burning mirrors and lenses," *Isis*, vol. 81, no. 3, pp. 464–491, 1990.

[3] A. Van Helden, S. Dupre, and R. Van Gent, *The Origins of the Telescope.* Amsterdam University Press - History of Science and Scholarship in the Netherlan, KNAW Press, 2010.

[4] E. Abbe, "Beitrage zur theorie des mikroskops und der mikroskopischen wahrnehmung," *Archiv fur mikroskopische Anatomie*, vol. 9, no. 1, pp. 413–418, 1873.

[5] S. R. y Cajal, *Comparative study of the sensory areas of the human cortex.* 1899.

[6] H. Siedentopf and R. Zsigmondy, "Uber sichtbarmachung und größenbestimmung ultramikoskopischer teilchen, mit besonderer anwendung auf goldrubingläser," *Annalen der Physik*, vol. 315, no. 1, pp. 1–39, 1902.

[7] F. Zernike, "Das phasenkontrastverfahren bei der mikroskopischen beobachtung," *Z. Tech. Phys*, vol. 16, pp. 454–457, 1935.

[8] W. Schmidt, "Doppelbrechung der kernspindel und zugfasertheorie der chromosomenbewegung," *Zeitschrift für Zellforschung und Mikroskopische Anatomie Abt. B Chromosoma*, vol. 1, no. 1, pp. 253–264, 1939.

[9] G. G. Stokes, "On the change of refrangibility of light," *Philosophical Transactions of the Royal Society of London*, vol. 142, pp. 463–562, 1852.

[10] M. Knoll and E. Ruska, "Das elektronenmikroskop," *Zeitschrift für Physik*, vol. 78, no. 5-6, pp. 318–339, 1932.

[11] G. Binnig, H. Rohrer, C. Gerber, and E. Weibel, "Surface studies by scanning tunneling microscopy," *Physical review letters*, vol. 49, no. 1, p. 57, 1982.

[12] D. W. Pohl, W. Denk, and M. Lanz, "Optical stethoscopy: Image recording with resolution $\lambda/20$," *Applied physics letters*, vol. 44, no. 7, pp. 651–653, 1984.

[13] G. Binnig, C. F. Quate, and C. Gerber, "Atomic force microscope," *Physical review letters*, vol. 56, no. 9, p. 930, 1986.

[14] M. Minsky, "Microscopy apparatus (US Patent)," Dec. 1961.

[15] D. Axelrod, "Cell-substrate contacts illuminated by total internal reflection fluorescence," *Journal of Cell Biology*, vol. 89, pp. 141–145, Apr. 1981.

[16] B. Valeur and M. N. Berberan-Santos, *Molecular fluorescence: principles and applications.* John Wiley & Sons, 2012.

[17] O. Dann, G. Bergen, E. Demant, and G. Volz, “Trypanocide diamidine des 2-phenylbenzofurans, 2-phenyl-indens und 2-phenyl-indols,” *Justus Liebigs Annalen der Chemie*, vol. 749, no. 1, pp. 68–89, 1971.

[18] J. A. Barden, M. Miki, B. D. Hambly, and C. G. Dos Remedios, “Localization of the phalloidin and nucleotide-binding sites on actin,” *European Journal of Biochemistry*, vol. 162, no. 3, pp. 583–588, 1987.

[19] E. Wulf, A. Deboben, F. Bautz, H. Faulstich, and T. Wieland, “Fluorescent phallotoxin, a tool for the visualization of cellular actin,” *Proceedings of the National Academy of Sciences*, vol. 76, no. 9, pp. 4498–4502, 1979.

[20] A. H. Coons, H. J. Creech, and R. N. Jones, “Immunological properties of an antibody containing a fluorescent group.,” *Experimental Biology and Medicine*, vol. 47, no. 2, pp. 200–202, 1941.

[21] M. Chalfie, Y. Tu, G. Euskirchen, W. Ward, and D. Prasher, “Green fluorescent protein as a marker for gene expression,” *Science*, vol. 263, no. 5148, pp. 802–805, 1994.

[22] R. Y. Tsien, “The green fluorescent protein,” *Annual Review of Biochemistry*, vol. 67, no. 1, pp. 509–544, 1998. PMID: 9759496.

[23] M. V. Matz, A. F. Fradkov, Y. A. Labas, A. P. Savitsky, A. G. Zaraisky, M. L. Markelov, and S. A. Lukyanov, “Fluorescent proteins from nonbioluminescent anthozoa species,” *Nature biotechnology*, vol. 17, no. 10, pp. 969–973, 1999.

[24] G. H. Patterson and J. Lippincott-Schwartz, “A photoactivatable gfp for selective photolabeling of proteins and cells,” *Science*, vol. 297, no. 5588, pp. 1873–1877, 2002.

[25] R. Ando, H. Hama, M. Yamamoto-Hino, H. Mizuno, and A. Miyawaki, “An optical marker based on the uv-induced green-to-red photoconversion of a fluorescent protein,” *Proceedings of the National Academy of Sciences*, vol. 99, no. 20, pp. 12651–12656, 2002.

[26] N. C. Shaner, R. E. Campbell, P. A. Steinbach, B. N. Giepmans, A. E. Palmer, and R. Y. Tsien, “Improved monomeric red, orange and yellow fluorescent proteins derived from discosoma sp. red fluorescent protein,” *Nature biotechnology*, vol. 22, no. 12, pp. 1567–1572, 2004.

[27] L. Novotny and B. Hecht, *Principles of Nano-optics*, ch. 4. Cambridge University Press, 2006.

[28] M. Von Ardenne and D. Beischer, “Untersuchung von Metalloxyd-Rauchen mit dem Universal-Elektronenmikroskop,” *Zeitschrift fur Elektrochemie und angewandte physikalische Chemie*, vol. 46, no. 4, pp. 270–277, 1940.

[29] G. Binnig, H. Rohrer, C. Gerber, and E. Weibel, “Surface studies by scanning tunneling microscopy,” *Phys. Rev. Lett.*, vol. 49, pp. 57–61, Jul 1982.

[30] T. Wilson and C. Sheppard, *Theory and Practice of Scanning Optical Microscopy.* Academic Press, 1984.

[31] W. Denk, J. Strickler, and W. Webb, “Two-photon laser scanning fluorescence microscopy,” *Science*, vol. 248, no. 4951, pp. 73–76, 1990.

[32] M. Bertero, P. Boccacci, G. J. Brakenhoff, F. Malfanti, and H. T. M. van der Voort, “Three-dimensional image restoration and super-resolution in fluorescence confocal microscopy,” *Journal of Microscopy*, vol. 157, no. 1, pp. 3–20, 1990.

[33] Schönle, A. and Hell, S. W., “Far-field fluorescence microscopy with repetitive excitation,” *Eur. Phys. J. D*, vol. 6, no. 3, pp. 283–290, 1999.

[34] S. W. Hell and E. H. K. Stelzer, "Properties of a 4Pi confocal fluorescence microscope," *Journal of the Optical Society of America A*, vol. 9, no. 12, pp. 2159–2166, 1992.

[35] H. Gugel, J. Bewersdorf, S. Jakobs, J. Engelhardt, R. Storz, and S. W. Hell, "Cooperative 4Pi excitation and detection yields sevenfold sharper optical sections in live-cell microscopy.," *Biophysical journal*, vol. 87, pp. 4146–52, dec 2004.

[36] J. Bewersdorf, R. Schmidt, and S. Hell, "Comparison of I^5M and 4Pi-microscopy," *Journal of microscopy*, vol. 222, no. 2, pp. 105–117, 2006.

[37] M. G. L. Gustafsson, "Surpassing the lateral resolution limit by a factor of two using structured illumination microscopy," *Journal of Microscopy*, vol. 198, no. 2, pp. 82–87, 2000.

[38] E. Betzig, R. J. Chichester, F. Lanni, and D. L. Taylor, "Near-field fluorescence imaging of cytoskeletal actin," *Bioimaging*, vol. 1, no. 3, pp. 129–135, 1993.

[39] A. Kirsch, C. Meyer, and T. M. Jovin, "Integration of optical techniques in scanning probe microscopes," vol. 286, pp. 317–323, 1996.

[40] X. Hao, C. Kuang, Z. Gu, Y. Wang, S. Li, Y. Ku, Y. Li, J. Ge, and X. Liu, "From microscopy to nanoscopy via visible light," *Light: Science & Applications*, vol. 2, no. 10, p. e108, 2013.

[41] S. W. Hell and J. Wichmann, "Breaking the diffraction resolution limit by stimulated emission: stimulated-emission-depletion fluorescence microscopy," *Opt. Lett.*, vol. 19, pp. 780–782, Jun 1994.

[42] T. A. Klar, S. Jakobs, M. Dyba, A. Egner, and S. W. Hell, "Fluorescence microscopy with diffraction resolution barrier broken by stimulated emission," *Proceedings of the National Academy of Sciences*, vol. 97, no. 15, pp. 8206–8210, 2000.

[43] S. Hell and M. Kroug, "Ground-state-depletion fluorscence microscopy: A concept for breaking the diffraction resolution limit," *Applied Physics B*, vol. 60, no. 5, pp. 495–497, 1995.

[44] R. Heintzmann, T. M. Jovin, and C. Cremer, "Saturated patterned excitation microscopy—a concept for optical resolution improvement," *JOSA A*, vol. 19, no. 8, pp. 1599–1609, 2002.

[45] M. G. Gustafsson, "Nonlinear structured-illumination microscopy: wide-field fluorescence imaging with theoretically unlimited resolution," *Proceedings of the National Academy of Sciences of the United States of America*, vol. 102, no. 37, pp. 13081–13086, 2005.

[46] T. Grotjohann, I. Testa, M. Leutenegger, H. Bock, N. T. Urban, F. Lavoie-Cardinal, K. I. Willig, C. Eggeling, S. Jakobs, and S. W. Hell, "Diffraction-unlimited all-optical imaging and writing with a photochromic GFP," *Nature*, vol. 478, pp. 204–208, Oct. 2011.

[47] R. E. Thompson, D. R. Larson, and W. W. Webb, "Precise nanometer localization analysis for individual fluorescent probes.," *Biophysical journal*, vol. 82, pp. 2775–83, may 2002.

[48] E. Betzig, G. H. Patterson, R. Sougrat, O. W. Lindwasser, S. Olenych, J. S. Bonifacino, M. W. Davidson, J. Lippincott-Schwartz, and H. F. Hess, "Imaging intracellular fluorescent proteins at nanometer resolution," *Science*, vol. 313, no. 5793, pp. 1642–1645, 2006.

[49] S. T. Hess, T. P. K. Girirajan, and M. D. Mason, "Ultra-High Resolution Imaging by Fluorescence Photoactivation Localization Microscopy," *Biophysical Journal*, vol. 91, pp. 4258–4272, Dec. 2006.

[50] J. Fölling, M. Bossi, H. Bock, R. Medda, C. A. Wurm, B. Hein, S. Jakobs, C. Eggeling, and S. W. Hell, "Fluorescence nanoscopy by ground-state depletion and single-molecule return," *Nature Methods*, vol. 5, no. 11, pp. 1–3, 2008.

[51] M. J. Rust, M. Bates, and X. Zhuang, "Sub-diffraction-limit imaging by stochastic optical reconstruction microscopy (STORM).," *Nature methods*, vol. 3, no. 10, pp. 793–795, 2006.

[52] A. Sharonov and R. M. Hochstrasser, "Wide-field subdiffraction imaging by accumulated binding of diffusing probes.," *Proceedings of the National Academy of Sciences of the United States of America*, vol. 103, pp. 18911–6, dec 2006.

[53] R. Jungmann, C. Steinhauer, M. Scheible, A. Kuzyk, P. Tinnefeld, and F. C. Simmel, "Single-molecule kinetics and super-resolution microscopy by fluorescence imaging of transient binding on DNA origami," *Nano Letters*, vol. 10, no. 11, pp. 4756–4761, 2010.

[54] N. Bobroff, "Position measurement with a resolution and noise-limited instrument," *Review of Scientific Instruments*, vol. 57, no. 6, p. 1152, 1986.

[55] R. J. Ober, S. Ram, and E. S. Ward, "Localization accuracy in single-molecule microscopy.," *Biophysical journal*, vol. 86, pp. 1185–200, feb 2004.

[56] C. S. Smith, N. Joseph, B. Rieger, and K. a. Lidke, "Fast, single-molecule localization that achieves theoretically minimum uncertainty.," *Nature methods*, vol. 7, pp. 373–5, may 2010.

[57] B. Rieger and S. Stallinga, "The Lateral and Axial Localization Uncertainty in Super-Resolution Light Microscopy," *ChemPhysChem*, pp. n/a–n/a, dec 2013.

[58] A. Yildiz, J. N. Forkey, S. a. McKinney, T. Ha, Y. E. Goldman, and P. R. Selvin, "Myosin V walks hand-over-hand: single fluorophore imaging with 1.5-nm localization.," *Science (New York, N.Y.)*, vol. 300, pp. 2061–5, jun 2003.

[59] B. Huang, W. Wang, M. Bates, and X. Zhuang, "Three-dimensional super-resolution imaging by stochastic optical reconstruction microscopy.," *Science (New York, N.Y.)*, vol. 319, pp. 810–3, feb 2008.

[60] M. P. Backlund, M. D. Lew, A. S. Backer, S. J. Sahl, G. Grover, A. Agrawal, R. Piestun, and W. E. Moerner, "The double-helix point spread function enables precise and accurate measurement of 3D single-molecule localization and orientation," *Proceedings of SPIE*, vol. 8590, pp. 85900L–85900L–11, feb 2013.

[61] M. Bates, B. Huang, G. T. Dempsey, and X. Zhuang, "Multicolor super-resolution imaging with photo-switchable fluorescent probes.," *Science (New York, N.Y.)*, vol. 317, pp. 1749–53, sep 2007.

[62] I. Testa, C. a. Wurm, R. Medda, E. Rothermel, C. von Middendorf, J. Fölling, S. Jakobs, A. Schönle, S. W. Hell, and C. Eggeling, "Multicolor fluorescence nanoscopy in fixed and living cells by exciting conventional fluorophores with a single wavelength.," *Biophysical journal*, vol. 99, pp. 2686–94, oct 2010.

[63] M. Bates, G. T. Dempsey, K. H. Chen, and X. Zhuang, "Multicolor super-resolution fluorescence imaging via multi-parameter fluorophore detection.," *Chemphyschem : a European journal of chemical physics and physical chemistry*, vol. 13, pp. 99–107, jan 2012.

[64] A. Lampe, V. Haucke, S. J. Sigrist, M. Heilemann, and J. Schmoranzer, "Multi-colour direct STORM with red emitting carbocyanines," *Biology of the Cell*, vol. 104, no. 4, pp. 229–237, 2012.

[65] R. Jungmann, M. S. Avendaño, J. B. Woehrstein, M. Dai, W. M. Shih, and P. Yin, "Multiplexed 3D cellular super-resolution imaging with DNA-PAINT and Exchange-PAINT.," *Nature methods*, vol. 11, no. 3, pp. 313–8, 2014.

[66] J. Tam, G. A. Cordier, J. S. Borbely, A. Sandoval Álvarez, and M. Lakadamyali, "Cross-Talk-Free Multi-Color STORM Imaging Using a Single Fluorophore.," *PLOS ONE*, vol. 9, p. e101772, jan 2014.

[67] Z. Zhang, S. J. Kenny, M. Hauser, W. Li, and K. Xu, "Ultrahigh-throughput resolved super-resolution microscopy," *Nature Methods*, vol. 12, no. 10, 2015.

[68] M. J. Mlodzianoski, N. M. Curthoys, M. S. Gunewardene, S. Carter, and S. T. Hess, "Super-resolution imaging of molecular emission spectra and single molecule spectral fluctuations," *PLOS ONE*, vol. 11, no. 3, p. e0147506, 2016.

[69] C. v. Middendorff, A. Egner, C. Geisler, S. W. Hell, and A. Schönle, "Isotropic 3D nanoscopy based on single emitter switching," *Optics express*, vol. 16, no. 25, pp. 20774–20788, 2008.

[70] G. Shtengel, J. A. Galbraith, C. G. Galbraith, J. Lippincott-Schwartz, J. M. Gillette, S. Manley, R. Sougrat, C. M. Waterman, P. Kanchanawong, M. W. Davidson, *et al.*, "Interferometric fluorescent super-resolution microscopy resolves 3D cellular ultrastructure," *Proceedings of the National Academy of Sciences*, vol. 106, no. 9, pp. 3125–3130, 2009.

[71] D. Aquino, A. Schönle, C. Geisler, C. V. Middendorff, C. A. Wurm, Y. Okamura, T. Lang, S. W. Hell, and A. Egner, "Two-color nanoscopy of three-dimensional volumes by 4Pi detection of stochastically switched fluorophores.," *Nature methods*, vol. 8, pp. 353–9, apr 2011.

[72] S. T. Hess, T. J. Gould, M. V. Gudheti, S. A. Maas, K. D. Mills, and J. Zimmerberg, "Dynamic clustered distribution of hemagglutinin resolved at 40 nm in living cell membranes discriminates between raft theories," *Proceedings of the National Academy of Sciences*, vol. 104, no. 44, pp. 17370–17375, 2007.

[73] H. Shroff, C. G. Galbraith, J. A. Galbraith, and E. Betzig, "Live-cell photoactivated localization microscopy of nanoscale adhesion dynamics," *Nature methods*, vol. 5, no. 5, pp. 417–423, 2008.

[74] H.-l. D. Lee, S. J. Lord, S. Iwanaga, K. Zhan, H. Xie, J. C. Williams, H. Wang, G. R. Bowman, E. D. Goley, L. Shapiro, *et al.*, "Superresolution imaging of targeted proteins in fixed and living cells using photoactivatable organic fluorophores," *Journal of the American Chemical Society*, vol. 132, no. 43, pp. 15099–15101, 2010.

[75] R. Wombacher, M. Heidbreder, S. van de Linde, M. P. Sheetz, M. Heilemann, V. W. Cornish, and M. Sauer, "Live-cell super-resolution imaging with trimethoprim conjugates," *Nature methods*, vol. 7, no. 9, pp. 717–719, 2010.

[76] S. a. Jones, S.-H. Shim, J. He, and X. Zhuang, "Fast, three-dimensional super-resolution imaging of live cells.," *Nature methods*, vol. 8, pp. 499–508, jun 2011.

[77] F. Huang, S. L. Schwartz, J. M. Byars, and K. A. Lidke, "Simultaneous multiple-emitter fitting for single molecule super-resolution imaging," *Biomedical optics express*, vol. 2, no. 5, pp. 1377–1393, 2011.

[78] L. Zhu, W. Zhang, D. Elnatan, and B. Huang, "Faster STORM using compressed sensing.," *Nature methods*, vol. 9, pp. 721–3, jul 2012.

[79] J. Min, C. Vonesch, H. Kirshner, L. Carlini, N. Olivier, S. Holden, S. Manley, J. C. Ye, and M. Unser, "FALCON: fast and unbiased reconstruction of high-density super-resolution microscopy data," *Scientific reports*, vol. 4, p. 4577, 2014.

[80] H. Babcock, Y. M. Sigal, and X. Zhuang, "A high-density 3D localization algorithm for stochastic optical reconstruction microscopy," *Optical Nanoscopy*, vol. 1, no. 1, p. 6, 2012.

[81] A. Barsic, G. Grover, and R. Piestun, "Three-dimensional super-resolution and localization of dense clusters of single molecules.," *Scientific reports*, vol. 4, p. 5388, 2014.

[82] S. Cox, E. Rosten, J. Monypenny, T. Jovanovic-Talisman, D. T. Burnette, J. Lippincott-Schwartz, G. E. Jones, and R. Heintzmann, "Bayesian localization microscopy reveals nanoscale podosome dynamics," *Nature methods*, vol. 9, no. 2, pp. 195–200, 2012.

[83] Š. Bálint, I. V. Vilanova, Á. S. Álvarez, and M. Lakadamyali, "Correlative live-cell and superresolution microscopy reveals cargo transport dynamics at microtubule intersections," *Proceedings of the National Academy of Sciences*, vol. 110, no. 9, pp. 3375–3380, 2013.

[84] F. Huang, T. M. P. Hartwich, F. E. Rivera-molina, Y. Lin, W. C. Duim, J. J. Long, P. D. Uchil, J. R. Myers, M. A. Baird, W. Mothes, M. W. Davidson, D. Toomre, and J. J. Bewersdorf, "Video-rate nanoscopy using sCMOS camera – specific single-molecule localization algorithms," *Nature Methods*, vol. 10, no. 7, 2013.

[85] A. Small and S. Stahlheber, "Fluorophore localization algorithms for super-resolution microscopy," *Nature Methods*, vol. 11, pp. 267–279, feb 2014.

[86] J. Engelhardt, J. Keller, P. Hoyer, M. Reuss, T. Staudt, and S. W. Hell, "Molecular orientation affects localization accuracy in superresolution far-field fluorescence microscopy," *Nano letters*, vol. 11, no. 1, pp. 209–213, 2010.

[87] S. Stallinga and B. Rieger, "Accuracy of the gaussian point spread function model in 2D localization microscopy.," *Optics express*, vol. 18, pp. 24461–76, nov 2010.

[88] M. D. Lew, M. P. Backlund, and W. E. Moerner, "Rotational Mobility of Single Molecules Affects Localization Accuracy in Super-Resolution Fluorescence Microscopy," *Nano letters*, vol. 13, no. 9, pp. 3967–3972, 2013.

[89] T. Quan, S. Zeng, and Z.-L. Huang, "Localization capability and limitation of electron-multiplying charge-coupled, scientific complementary metal-oxide semiconductor, and charge-coupled devices for superresolution imaging.," *Journal of biomedical optics*, vol. 15, no. 6, p. 066005, 2010.

[90] P. Prabhat, S. Ram, E. S. Ward, and R. J. Ober, "Simultaneous imaging of different focal planes in fluorescence microscopy for the study of cellular dynamics in three dimensions," *IEEE transactions on nanobioscience*, vol. 3, no. 4, pp. 237–242, 2004.

[91] E. Toprak, H. Balci, B. H. Blehm, and P. R. Selvin, "Three-dimensional particle tracking via bifocal imaging," *Nano letters*, vol. 7, no. 7, pp. 2043–2045, 2007.

[92] M. F. Juette, T. J. Gould, M. D. Lessard, M. J. Mlodzianoski, B. S. Nagpure, B. T. Bennett, S. T. Hess, and J. Bewersdorf, "Three-dimensional sub–100 nm resolution fluorescence microscopy of thick samples," *Nature methods*, vol. 5, no. 6, pp. 527–529, 2008.

[93] M. D. McMahon, A. J. Berglund, P. Carmichael, J. J. McClelland, and J. A. Liddle, "3D particle trajectories observed by orthogonal tracking microscopy," *ACS nano*, vol. 3, no. 3, pp. 609–614, 2009.

[94] J. Tang, J. Akerboom, A. Vaziri, L. L. Looger, and C. V. Shank, "Near-isotropic 3D optical nanoscopy with photon-limited chromophores," *Proceedings of the National Academy of Sciences*, vol. 107, no. 22, pp. 10068–10073, 2010.

[95] B. Bailey, D. L. Farkas, D. L. Taylor, and F. Lanni, "Enhancement of axial resolution in fluorescence microscopy by standing-wave excitation.," *Nature*, vol. 365, no. 6450, p. 44, 1993.

[96] J. Deschamps, M. Mund, and J. Ries, "3D superresolution microscopy by supercritical angle detection," *Optics Express*, vol. 22, no. 23, p. 29081, 2014.

[97] N. Bourg, C. Mayet, G. Dupuis, T. Barroca, P. Bon, S. Lécart, E. Fort, and S. Lévêque-Fort, "Direct optical nanoscopy with axially localized detection," *Nature Photonics*, vol. 9, no. 9, pp. 587–593, 2015.

[98] H. P. Kao and a. S. Verkman, "Tracking of single fluorescent particles in three dimensions: use of cylindrical optics to encode particle position.," *Biophysical journal*, vol. 67, pp. 1291–300, sep 1994.

[99] J. Yajima, K. Mizutani, and T. Nishizaka, "A torque component present in mitotic kinesin Eg5 revealed by three-dimensional tracking," *Nature structural & molecular biology*, vol. 15, no. 10, pp. 1119–1121, 2008.

[100] Y. Sun, J. D. McKenna, J. M. Murray, E. M. Ostap, and Y. E. Goldman, "Parallax: high accuracy three-dimensional single molecule tracking using split images," *Nano letters*, vol. 9, no. 7, pp. 2676–2682, 2009.

[101] D. Baddeley, M. B. Cannell, and C. Soeller, "Three-dimensional sub-100 nm super-resolution imaging of biological samples using a phase ramp in the objective pupil," *Nano Research*, vol. 4, no. 6, pp. 589–598, 2011.

[102] M. D. Lew, S. F. Lee, M. Badieirostami, and W. Moerner, "Corkscrew point spread function for far-field three-dimensional nanoscale localization of pointlike objects," *Optics letters*, vol. 36, no. 2, pp. 202–204, 2011.

[103] S. R. P. Pavani and R. Piestun, "Three dimensional tracking of fluorescent microparticles using a photon-limited double-helix response system," *Optics express*, vol. 16, no. 26, pp. 22048–22057, 2008.

[104] S. R. P. Pavani, M. A. Thompson, J. S. Biteen, S. J. Lord, N. Liu, R. J. Twieg, R. Piestun, and W. Moerner, "Three-dimensional, single-molecule fluorescence imaging beyond the diffraction limit by using a double-helix point spread function," *Proceedings of the National Academy of Sciences*, vol. 106, no. 9, pp. 2995–2999, 2009.

[105] M. A. Thompson, M. D. Lew, M. Badieirostami, and W. Moerner, "Localizing and tracking single nanoscale emitters in three dimensions with high spatiotemporal resolution using a double-helix point spread function," *Nano letters*, vol. 10, no. 1, pp. 211–218, 2009.

[106] I. Izeddin, M. El Beheiry, J. Andilla, D. Ciepielewski, X. Darzacq, and M. Dahan, "PSF shaping using adaptive optics for three-dimensional single-molecule super-resolution imaging and tracking," *Optics Express*, vol. 20, no. 5, p. 4957, 2012.

[107] S. Jia, J. C. Vaughan, and X. Zhuang, "Isotropic three-dimensional super-resolution imaging with a self-bending point spread function," *Nature Photonics*, pp. 1–5, mar 2014.

[108] L. Oudjedi, J.-B. Fiche, S. Abrahamsson, L. Mazenq, A. Lecestre, P.-F. Calmon, A. Cerf, and M. Nöllmann, "Astigmatic multifocus microscopy enables deep 3d super-resolved imaging," *Biomed. Opt. Express*, vol. 7, pp. 2163–2173, Jun 2016.

[109] A. Frodesen, O. Skjeggestad, and H. Tøfte, *Probability and statistics in particle physics*. No. v. 2 in Probability and Statistics in Particle Physics, Universitetsforl., 1979.

[110] S. M. Kay, *Fundamentals of Statistical Signal Processing: Practical Algorithm Development*, vol. 3. Pearson Education, 2013.

[111] A. V. Abraham, S. Ram, J. Chao, E. Ward, and R. J. Ober, "Quantitative study of single molecule location estimation techniques," *Optics express*, vol. 17, no. 26, pp. 23352–23373, 2009.

[112] E. Hoogendoorn, K. C. Crosby, D. Leyton-Puig, R. M. P. Breedijk, K. Jalink, T. W. J. Gadella, and M. Postma, "The fidelity of stochastic single-molecule super-resolution reconstructions critically depends upon robust background estimation.," *Scientific reports*, vol. 4, p. 3854, jan 2014.

[113] D. Sage, H. Kirshner, T. Pengo, N. Stuurman, J. Min, S. Manley, and M. Unser, "Quantitative evaluation of software packages for single-molecule localization microscopy.," *Nature Methods*, vol. 12, no. August 2014, pp. 1–12, 2015.

[114] M. J. Rust, M. Bates, and X. Zhuang, "Sub-diffraction-limit imaging by stochastic optical reconstruction microscopy (STORM)," *Nature Methods*, vol. 3, no. 10, 2006.

[115] G. T. Dempsey, M. Bates, W. E. Kowtoniuk, D. R. Liu, R. Y. Tsien, and X. Zhuang, "Photoswitching mechanism of cyanine dyes," *Journal of the American Chemical Society*, vol. 131, no. 51, pp. 18192–18193, 2009.

[116] J. Vogelsang, T. Cordes, C. Forthmann, C. Steinhauer, and P. Tinnefeld, "Controlling the fluorescence of ordinary oxazine dyes for single-molecule switching and superresolution microscopy," *Proceedings of the National Academy of Sciences*, vol. 106, no. 20, pp. 8107–8112, 2009.

[117] G. T. Dempsey, J. C. Vaughan, K. H. Chen, M. Bates, and X. Zhuang, "Evaluation of fluorophores for optimal performance in localization-based super-resolution imaging," *Nature Methods*, vol. 8, no. 12, pp. 793–795, 2011.

[118] S. van de Linde, A. Löschberger, T. Klein, M. Heidbreder, S. Wolter, M. Heilemann, and M. Sauer, "Direct stochastic optical reconstruction microscopy with standard fluorescent probes.," *Nature protocols*, vol. 6, no. 7, pp. 991–1009, 2011.

[119] J. E. Berlier, A. Rothe, G. Buller, J. Bradford, D. R. Gray, B. J. Filanoski, W. G. Telford, S. Yue, J. Liu, C.-Y. Cheung, *et al.*, "Quantitative comparison of long-wavelength alexa fluor dyes to cy dyes: fluorescence of the dyes and their bioconjugates," *Journal of Histochemistry & Cytochemistry*, vol. 51, no. 12, pp. 1699–1712, 2003.

[120] X. Shi, J. Lim, and T. Ha, "Acidification of the oxygen scavenging system in single-molecule fluorescence studies: in situ sensing with a ratiometric dual-emission probe," *Analytical chemistry*, vol. 82, no. 14, pp. 6132–6138, 2010.

[121] M. Swoboda, H.-m. Cheng, D. Brugger, D. Haltrich, N. Plumere, and M. Schlierf, "Enzymatic Oxygen Scavenging for Photostability without pH Drop in Single-Molecule Experiments," *ACS Nano*, vol. 6, no. 7, pp. 6364–6369, 2012.

[122] S. V. D. Linde, J. Lehmann, M. Sauer, and S. Doose, "Methylene Blue- and Thiol-Based Oxygen Depletion for Super- Resolution Imaging," *Analytical chemistry*, vol. 85, pp. 3393–3400, 2013.

[123] N. Olivier, D. Keller, V. S. Rajan, G. Pierre, S. Manley, P. Gönczy, and S. Manley, "Simple buffers for 3D STORM microscopy," *Biomedical Optics Express*, vol. 4, pp. 16840–16841, may 2013.

[124] N. Olivier, D. Keller, P. Gönczy, and S. Manley, "Resolution Doubling in 3D-STORM Imaging through Improved Buffers.," *PLOS ONE*, vol. 8, p. e69004, jan 2013.

[125] L. Nahidiazar, A. V. Agronskaia, J. Broertjes, B. van den Broek, and K. Jalink, "Optimizing imaging conditions for demanding multi-color super resolution localization microscopy," *PLOS ONE*, vol. 11, no. 7, p. e0158884, 2016.

[126] I. Testa, A. Schönle, C. v. Middendorff, C. Geisler, R. Medda, C. A. Wurm, A. C. Stiel, S. Jakobs, M. Bossi, C. Eggeling, S. W. Hell, and A. Egner, "Nanoscale separation of molecular species based on their rotational mobility," *Opt. Express*, vol. 16, pp. 21093–21104, Dec 2008.

[127] A. Egner, C. Geisler, C. von Middendorff, H. Bock, D. Wenzel, R. Medda, M. Andresen, A. C. Stiel, S. Jakobs, C. Eggeling, A. Schönle, and S. W. Hell, "Fluorescence Nanoscopy in Whole Cells by Asynchronous Localization of Photoswitching Emitters," *Biophysical Journal*, vol. 93, pp. 3285–3290, Nov. 2007.

[128] M. Bates, B. Huang, and X. Zhuang, "Super-resolution microscopy by nanoscale localization of photo-switchable fluorescent probes," *Current opinion in chemical biology*, vol. 12, no. 5, pp. 505–514, 2008.

[129] A. R. Carter, G. M. King, T. A. Ulrich, W. Halsey, D. Alchenberger, and T. T. Perkins, "Stabilization of an optical microscope to 0.1 nm in three dimensions," *Applied optics*, vol. 46, no. 3, pp. 421–427, 2007.

[130] C. Geisler, T. Hotz, A. Schönle, S. W. Hell, A. Munk, and A. Egner, "Drift estimation for single marker switching based imaging schemes," *Optics Express*, vol. 20, no. 7, pp. 223–226, 2012.

[131] R. McGorty, D. Kamiyama, and B. Huang, "Active microscope stabilization in three dimensions using image correlation," *Optical Nanoscopy*, vol. 2, no. 1, p. 3, 2013.

[132] B. Huang, S. A. Jones, B. Brandenburg, and X. Zhuang, "Whole-cell 3D STORM reveals interactions between cellular structures with nanometer-scale resolution," *Nature Methods*, vol. 5, no. 12, pp. 1047–1052, 2008.

[133] M. Ovesnỳ, P. Křížek, J. Borkovec, Z. Švindrych, and G. M. Hagen, "ThunderSTORM: a comprehensive ImageJ plug-in for PALM and STORM data analysis and super-resolution imaging," *Bioinformatics*, vol. 30, no. 16, pp. 2389–2390, 2014.

[134] J. Schindelin, C. T. Rueden, M. C. Hiner, and K. W. Eliceiri, "The imagej ecosystem: An open platform for biomedical image analysis," *Molecular reproduction and development*, vol. 82, no. 7-8, pp. 518–529, 2015.

[135] S. Wolter, A. Löschberger, T. Holm, S. Aufmkolk, M.-C. Dabauvalle, S. van de Linde, M. Sauer, and S. van de Linde, "rapidSTORM : accurate , fast open-source software for localization microscopy orcae : online resource for community annotation of eukaryotes," *Nature methods*, vol. 9, pp. 1040–1, nov 2012.

[136] D. Baddeley, M. B. Cannell, and C. Soeller, "Visualization of localization microscopy data," *Microscopy and Microanalysis*, vol. 16, no. 01, pp. 64–72, 2010.

[137] H. Deschout, F. C. Zanacchi, M. Mlodzianoski, A. Diaspro, J. Bewersdorf, S. T. Hess, and K. Braeckmans, "Precisely and accurately localizing single emitters in fluorescence microscopy," *Nature Methods*, vol. 11, pp. 253–266, feb 2014.

[138] N. Banterle, K. H. Bui, E. A. Lemke, and M. Beck, "Fourier ring correlation as a resolution criterion for super-resolution microscopy," *Journal of Structural Biology*, vol. 183, no. 3, pp. 363–367, 2013.

[139] R. P. J. Nieuwenhuizen, K. a. Lidke, M. Bates, D. L. Puig, D. Grünwald, S. Stallinga, and B. Rieger, "Measuring image resolution in optical nanoscopy.," *Nature methods*, apr 2013.

[140] Y. Lin, J. J. Long, F. Huang, W. C. Duim, S. Kirschbaum, Y. Zhang, L. K. Schroeder, A. a. Rebane, M. G. M. Velasco, A. Virrueta, D. W. Moonan, J. Jiao, S. Y. Hernandez, Y. Zhang, and J. Bewersdorf, "Quantifying and Optimizing Single-Molecule Switching Nanoscopy at High Speeds," *PLOS ONE*, vol. 10, no. 5, p. e0128135, 2015.

[141] L. Novotny and B. Hecht, *Principles of Nano-optics*, ch. 2.11. Cambridge University Press.

[142] F. M. Barabas, L. A. Masullo, and F. D. Stefani, "Note: Tormenta: An open source python-powered control software for camera based optical microscopy," *Review of Scientific Instruments*, vol. 87, no. 12, p. 126103, 2016.

[143] R. Computing, "PyQT." `https://riverbankcomputing.com/software/pyqt/intro`, 2017. [Online; accessed 17-January-2017].

[144] L. Campagnola, "PyQtGraph: Scientific Graphics and GUI Library for Python." `http://www.pyqtgraph.org/`, 2017. [Online; accessed 17-January-2017].

[145] F. Barabas and L. Masullo, "Tormenta: Measurement control and analysis for super-resolution localization fluorescence microscopy." `https://github.com/fedebarabas/tormenta`, 2017. [Online; accessed 17-January-2017].

[146] M. Leung, "PyAPT: Controlling Thorlabs APT Using Python Code Using APT.dll and APT.lib, Bypassing the Activex Controls." `https://github.com/mcleung/PyAPT`, 2017. [Online; accessed 17-January-2017].

[147] L. Corporation, "Python and LJM (Windows, Mac, Linux)." `https://labjack.com/support/software/examples/ljm/python`, 2017. [Online; accessed 17-January-2017].

[148] H. Grecco, "Lantz: Simple yet powerful instrumentation in Python." `https://lantz.readthedocs.io/en/0.3/`, 2017. [Online; accessed 17-January-2017].

[149] D. Green, "A colour scheme for the display of astronomical intensity images," *arXiv preprint arXiv:1108.5083*, 2011.

[150] Andor Technology Ltd, *Andor iXon User Manual*.

[151] A. Desai and T. J. Mitchison, "Microtubule polymerization dynamics," *Annual review of cell and developmental biology*, vol. 13, no. 1, pp. 83–117, 1997.

[152] J. F. Lee, G. M. Stovall, and A. D. Ellington, "Aptamer therapeutics advance," *Current opinion in chemical biology*, vol. 10, no. 3, pp. 282–289, 2006.

[153] J. J. Schmied, A. Gietl, P. Holzmeister, C. Forthmann, C. Steinhauer, T. Dammeyer, and P. Tinnefeld, "Fluorescence and super-resolution standards based on DNA origami.," *Nature methods*, vol. 9, pp. 1133–4, dec 2012.

[154] G. GMBH, "Gatta-Paint Nanoruler." `http://www.gattaquant.com/products/localization-based/gatta-paint-nanoruler.html`, 2017. [Online; accessed 147-February-2017].

[155] P. W. Rothemund, "Folding DNA to create nanoscale shapes and patterns," *Nature*, vol. 440, no. 7082, pp. 297–302, 2006.

[156] S. Quirin, S. R. P. Pavani, and R. Piestun, "Optimal 3d single-molecule localization for superresolution microscopy with aberrations and engineered point spread functions," *Proceedings of the National Academy of Sciences*, vol. 109, no. 3, pp. 675–679, 2012.

[157] R. I. Hartley and A. Zisserman, *Multiple View Geometry in Computer Vision*, ch. 4. Cambridge University Press, ISBN: 0521540518, second ed., 2004.

[158] K. Xu, G. Zhong, and X. Zhuang, "Actin , Spectrin , and Associated Proteins Form a Periodic Cytoskeletal Structure in Axons," *Sciencexpress*, vol. 10.1126, no. December, 2012.

[159] G. Zhong, J. He, R. Zhou, D. Lorenzo, H. P. Babcock, V. Bennett, and X. Zhuang, "Developmental mechanism of the periodic membrane skeleton in axons," *Elife*, vol. 3, p. e04581, 2014.

[160] E. D'Este, D. Kamin, F. Göttfert, A. El-Hady, and S. W. Hell, "Sted nanoscopy reveals the ubiquity of subcortical cytoskeleton periodicity in living neurons," *Cell reports*, vol. 10, no. 8, pp. 1246–1251, 2015.

[161] E. D'Este, D. Kamin, C. Velte, F. Göttfert, M. Simons, and S. W. Hell, "Subcortical cytoskeleton periodicity throughout the nervous system," *Scientific reports*, vol. 6, 2016.

[162] J. He, R. Zhou, Z. Wu, M. A. Carrasco, P. T. Kurshan, J. E. Farley, D. J. Simon, G. Wang, B. Han, J. Hao, *et al.*, "Prevalent presence of periodic actin–spectrin-based membrane skeleton in a broad range of neuronal cell types and animal species," *Proceedings of the National Academy of Sciences*, p. 201605707, 2016.

[163] K. Xu, G. Zhong, and X. Zhuang, "Actin, spectrin, and associated proteins form a periodic cytoskeletal structure in axons," *Science*, vol. 339, no. 6118, pp. 452–456, 2013.

[164] M. D. Bordenave, *Mediciones con resolución nanométrica mediante depleción por emisión estimulada*. PhD thesis, Buenos Aires University, 2016.

[165] S. C. Sidenstein, E. D'Este, M. J. Böhm, J. G. Danzl, V. N. Belov, and S. W. Hell, "Multicolour multilevel sted nanoscopy of actin/spectrin organization at synapses," *Scientific reports*, vol. 6, 2016.

[166] D. Albrecht, C. M. Winterflood, M. Sadeghi, T. Tschager, F. Noé, and H. Ewers, "Nanoscopic compartmentalization of membrane protein motion at the axon initial segment," *J Cell Biol*, pp. jcb–201603108, 2016.

[167] F. Barabas and L. Masullo, "RingFinder." `https://github.com/fedebarabas/ringfinder`, 2017. [Online; accessed 7-February-2017].

[168] C. M. Tanner, F. Kamel, G. W. Ross, J. A. Hoppin, S. M. Goldman, M. Korell, C. Marras, G. S. Bhudhikanok, M. Kasten, A. R. Chade, *et al.*, "Rotenone, paraquat, and parkinson's disease," *Environmental health perspectives*, vol. 119, no. 6, p. 866, 2011.

[169] F. Kamel, "Paths from pesticides to parkinson's," *Science*, vol. 341, no. 6147, pp. 722–723, 2013.

[170] S. A. Giusti, A. M. Vogl, M. M. Brockmann, C. A. Vercelli, M. L. Rein, D. Trümbach, W. Wurst, D. Cazalla, V. Stein, J. M. Deussing, *et al.*, "Microrna-9 controls dendritic development by targeting rest," *Elife*, vol. 3, p. e02755, 2014.

[171] A. M. Vogl, M. M. Brockmann, S. A. Giusti, G. Maccarrone, C. A. Vercelli, C. A. Bauder, J. S. Richter, F. Roselli, A.-S. Hafner, N. Dedic, *et al.*, "Neddylation inhibition impairs spine development, destabilizes synapses and deteriorates cognition," *Nature neuroscience*, vol. 18, no. 2, pp. 239–251, 2015.

[172] J. H. Remme, P. Feenstra, P. Lever, A. C. Medici, C. M. Morel, M. Noma, K. Ramaiah, F. Richards, A. Seketeli, G. Schmunis, *et al.*, "Tropical diseases targeted for elimination: Chagas disease, lymphatic filariasis, onchocerciasis, and leprosy," *Disease control priorities in developing countries*, vol. 22, pp. 433–447, 2006.

[173] A. M. Macedo, R. P. Oliveira, and S. D. Pena, "Chagas disease: role of parasite genetic variation in pathogenesis," *Expert reviews in molecular medicine*, vol. 4, no. 05, pp. 1–16, 2002.

[174] A. V. Martins, A. P. Gomes, E. G. de Mendonça, J. L. R. Fietto, L. A. Santana, M. G. de Almeida Oliveira, M. Geller, R. de Freitas Santos, R. R. Vitorino, and R. Siqueira-Batista, "Biology of *Trypanosoma cruzi*: An update," *Infectio*, vol. 16, no. 1, pp. 45–58, 2012.

[175] J. C. P. Dias, "Acute chagas' disease," *Memórias do Instituto Oswaldo Cruz*, vol. 79, pp. 85–91, 1984.

[176] A. Prata, “Clinical and epidemiological aspects of chagas disease,” *The Lancet infectious diseases*, vol. 1, no. 2, pp. 92–100, 2001.

[177] F. S. Laranja, E. Dias, G. Nobrega, and A. Miranda, “Chagas' disease,” *Circulation*, vol. 14, no. 6, pp. 1035–1060, 1956.

[178] M. P. Barrett, R. J. Burchmore, A. Stich, J. O. Lazzari, A. C. Frasch, J. J. Cazzulo, and S. Krishna, “The trypanosomiases,” *The Lancet*, vol. 362, no. 9394, pp. 1469–1480, 2003.

[179] J. A. Marin-Neto, E. Cunha-Neto, B. C. Maciel, and M. V. Simões, “Pathogenesis of chronic chagas heart disease,” *Circulation*, vol. 115, no. 9, pp. 1109–1123, 2007.

[180] E. Vimr and C. Lichtensteiger, “To sialylate, or not to sialylate: that is the question,” *Trends in microbiology*, vol. 10, no. 6, pp. 254–257, 2002.

[181] M. E. Giorgi and R. M. de Lederkremer, “*Trans*-sialidase and mucins of *Trypanosoma cruzi*: an important interplay for the parasite,” *Carbohydrate research*, vol. 346, no. 12, pp. 1389–1393, 2011.

[182] J. Previato, A. F. Andrade, M. C. V. Pessolani, and L. Mendonça-Previato, “Incorporation of sialic acid into *Trypanosoma cruzi* macromolecules. a proposal for a new metabolic route,” *Molecular and biochemical parasitology*, vol. 16, no. 1, pp. 85–96, 1985.

[183] L. Freire-de Lima, L. Fonseca, T. Oeltmann, L. Mendonça-Previato, and J. Previato, “The *trans*-sialidase, the major *Trypanosoma cruzi* virulence factor: three decades of studies,” *Glycobiology*, p. cwv057, 2015.

[184] C. A. Buscaglia, V. A. Campo, A. C. Frasch, and J. M. Di Noia, “*Trypanosoma cruzi* surface mucins: host-dependent coat diversity,” *Nature Reviews Microbiology*, vol. 4, no. 3, pp. 229–236, 2006.

[185] G. D. Pollevick, J. Affranchino, A. C. Frasch, and D. O. Sánchez, “The complete sequence of a shed acute-phase antigen of *Trypanosoma cruzi*,” *Molecular and biochemical parasitology*, vol. 47, no. 2, pp. 247–250, 1991.

[186] A. B. Lantos, G. Carlevaro, B. Araoz, P. R. Diaz, M. de los Milagros Camara, C. A. Buscaglia, M. Bossi, H. Yu, X. Chen, C. R. Bertozzi, *et al.*, “Sialic acid glycobiology unveils *Trypanosoma cruzi* trypomastigote membrane physiology,” *PLOS Pathog*, vol. 12, no. 4, p. e1005559, 2016.

[187] A. F. F. R. Nardy, C. G. Freire-de Lima, A. R. Pérez, and A. Morrot, “Role of *Trypanosoma cruzi Trans*-sialidase on the escape from host immune surveillance,” *Frontiers in Microbiology*, vol. 7, p. 348, 2016.

[188] R. P. Muiá, H. Yu, J. A. Prescher, U. Hellman, X. Chen, C. R. Bertozzi, and O. Campetella, “Identification of glycoproteins targeted by *Trypanosoma cruzi trans*-sialidase, a virulence factor that disturbs lymphocyte glycosylation,” *Glycobiology*, vol. 20, no. 7, pp. 833–842, 2010.

[189] D. J. Metcalf, R. Edwards, N. Kumarswami, and A. E. Knight, “Test samples for optimizing storm super-resolution microscopy,” *JoVE (Journal of Visualized Experiments)*, no. 79, pp. e50579–e50579, 2013.